Study of Very High Energy Gamma-ray Emission from the Unidentified Source HESS J1614−518 with CANGAROO−III

Taku Mizukami

Very high energy gamma-ray observations using an Imaging Air Cherenkov Technique (IACT) have discovered more than 100 sources since the first detection of TeV gamma-rays from Crab nebula in 1989. The development of the IACT enables us to explore the site of the cosmic-ray acceleration, since very high energy gamma-rays are expected to be generated in the proximity of the acceleration site. Among those galactic TeV sources, one third of the gamma-ray sources are still unidentified gamma-ray sources. This large population indicates that they might play important role in the cosmic-ray acceleration. Thus, detailed discussion on the radiation mechanism for each source is necessary to estimate their contributions on the cosmic-ray acceleration quantitatively.

We observed one of the unidentified source, HESS J1614-518, using the CANGAROO-III imaging atmospheric Cherenkov telescope array, for 53.6 hr in 2008 May to August. Diffuse gamma-ray emission above 760 GeV with the 8.9σ level were detected. The spectrum was represented by a power-law:
$(8.2 \pm 2.2_{stat} \pm 2.5_{sys}) \times 10^{-12} \times (E/1\ \mathrm{TeV})^{-\gamma} \mathrm{cm}^{-2}\ \mathrm{s}^{-1}\ \mathrm{TeV}^{-1}$ with a photon index γ of $2.4 \pm 0.3_{stat} \pm 0.2_{sys}$, which was compatible with that of the previous H.E.S.S. observation.

By combining our result with multi wavelength data from radio to VHE gamma-ray band, I discuss the possible counterparts for HESS J1614-518 and consider radiation mechanisms based on hadronic and leptonic processes for a supernova remnant, stellar winds from massive stars, and a pulsar wind nebula, respectively.

For a supernova remnant scenario, the leptonic model gives a good reproduction of the observed spectrum with an ambient matter density n_p of 600 $p\ \mathrm{cm}^{-3}$, while there is no obvious overlapping molecular clouds. The hadronic model also shows a good reproduction of the spectrum. By assuming $n_p = 100p\ \mathrm{cm}^{-3}$, the efficiency of energy conversion to accelerate protons needed to explain observed TeV luminosity is 10% of a typical kinetic energy of the supernova explosion. In addition, I calculated the contribution of emissions from secondary electrons from $p - p$ interactions which has not been detected yet. The detection of this radiation will be a strong evidence for the hadronic model.

For the PWN scenario, the nearby known pulsars are not responsible since the spin-down powers are insufficient to produce the observed TeV gamma-ray luminosity.

For the stellar wind scenario, Pismis 22 was required to contain two O-type stars through its entire age from energetics considerations with $n_p = 100p\ \mathrm{cm}^{-3}$, which, however, seems controversial to the NANTEN observations.

The detection of the synchrotron emission in radio to optical band from the secondary electron will be a great evidence for SNR scenario with the hadronic model.

Contents

1 Introduction **9**

1.1 Development of gamma-ray astronomy 9

1.2 Cosmic-ray 10

2 Very high energy gamma-ray emission in the galaxy **13**

2.1 Mechanism of cosmic-ray acceleration 13

2.2 Mechanism of gamma-ray emission 16

2.2.1 π^0 decay 16

2.2.2 Synchrotron emission 18

2.2.3 Inverse Compton scattering 19

2.2.4 Bremsstrahlung 21

2.3 The galactic VHE gamma-ray sources 21

2.4 Supernova Remnant 21

2.5 Pulsar Wind Nebula 22

2.6 Massive Star Cluster 25

2.7 Binary systems 25

2.8 Unidentified VHE Gamma-ray source;
HESS J1614−518 25

3 Imaging Air Cherenkov Technique **35**

3.1 Extensive Air Shower 35

3.2 Cherenkov Radiation 38

3.2.1 Cherenkov Light Observation 40

4 CANGAROO-III telescope and Observation **48**

4.1 CANGAROO experiment 48

4.1.1 Reflector 49

4.1.2 Imaging Camera . . . 52
4.1.3 Electronics and Data Acquisition System . . . 52
4.2 Telescope performance . . . 59
4.2.1 Muon analysis . . . 59
4.3 Observation of HESS J1614-518 . . . 59
4.3.1 Observation Mode . . . 59
4.3.2 Observation of HESS J1614-518 . . . 60
4.4 Monte-Carlo Simulation . . . 61

5 Analysis **66**
5.1 Calibration for Cameras and ADCs . . . 66
5.2 Timewalk corrections . . . 67
5.3 Image Cleaning . . . 67
5.3.1 Cloud cut . . . 71
5.3.2 Edge cut . . . 71
5.4 Arrival direction determination . . . 73
5.4.1 An determination method for large zenith angle . . . 75
5.5 Gamma/Proton separation −Fisher Discriminant Method− . . . 78
5.5.1 Fisher fit . . . 83
5.6 Differential Flux . . . 87
5.7 Morphology . . . 88

6 Discussion **91**
6.1 SNR Scenario . . . 92
6.1.1 Leptonic Model . . . 94
6.1.2 Hadronic Model . . . 98
6.2 Stellar wind from massive stars scenario . . . 102
6.3 PWN Scenario . . . 102

7 Conclusion **106**

A Hillas parameters **108**

B statistical significance **110**

C Spindown luminosity and magnetic field of pulsar **113**

D Braking index and characteristic age of pulsar **114**

List of Figures

1.1 Number of detected high energy sources. 10
1.2 Energy spectrum of cosmic-ray. 12

2.1 Schematic view of the acceleration at the shock front. 14
2.2 Classification of the galactic sources. 21
2.3 Gamma-ray excess map of SN 1006 23
2.4 SED predicted for SN 1006. 24
2.5 Schematic view of a pulsar system 24
2.6 Schematic views of the binary systems detected by VHE gamma-rays . . . 26
2.7 Periodogram of binary system, LS 5039 27
2.8 SED of LS 5039 28
2.9 The gamma-ray population in the galactic plane. 29
2.10 H.E.S.S. observation results of HESS J1614−518. 30
2.11 *Suzaku* observation region for HESS J1614−518. 30
2.12 *Suzaku* image for HESS J1614−518 observation. 31
2.13 *Suzaku* spectrum for HESS J1614−518 observation. 31
2.14 Swift source map. 33
2.15 The spectrum given by Lande et al. (2012) for HESS J1614−518 (right top). 34

3.1 Schematic diagram of EAS. 37
3.2 The number of particles in an EAS by gamma rays. 37
3.3 Schematic diagram of the development of a nucleonic cascade in the atmosphere. 38
3.4 Polarization set up in a dielectric when a charged particle passes through. . 39
3.5 Different property of the Cherenkov radiation related to electrons 40
3.6 A sketch of Cherenkov light on the ground 41

3.7 Distribution of the Cherenkov light on the ground 42
3.8 Energy dependence of the Cherenkov light density on the ground 44
3.9 A Schematic of geometry of a shower and a Cherenkov telescope 44
3.10 EAS images on imaging camera 45
3.11 Definition of the image parameters 45
3.12 Shower reconstruction 46
3.13 Shower reconstruction 46
3.14 Angular resolution and the pitch of telescopes 47
3.15 Angular resolution and the number of telescopes 47
3.16 Muon event 47

4.1 Position of the observation site of the CANGAROO-III, Woomera. 48
4.2 Geometrical distribution of CANGAROO-III telescope array. 49
4.3 Facets alignment system 50
4.4 FRP cross section drawing. 50
4.5 A GFRP facet 50
4.6 Reflectivity of FRP mirrors. 51
4.7 Optical spot size of CANGAROO-III telescope 51
4.8 Imaging camera of CANGAROO-III 53
4.9 Photomultiplier tube of CANGAROO-III 53
4.10 Reflectance of the light guide 54
4.11 Block diagram of the DSM 55
4.12 PMT grouping 55
4.13 Logic of local trigger 57
4.14 Global Trigger System 57
4.15 Timing chart of the trigger system 58
4.16 Time variation of the light collecting efficiency. 60
4.17 Wobble position 61
4.18 Zenith angle distributions of ON run. 62
4.19 Mean value of $WIDTH$ distribution by changing the number of the atmosphere layers in Monte-Carlo code. 63
4.20 Waveform of PMT signal 64
4.21 NSB measurement 64

5.1 The schematic of timewalk. 68

5.2 An example of the correlation between ADC channels and TDC channels (Nakamori, 2008). 68
5.3 Distributions of arrival time of whole PMTs in the camera. 69
5.4 An example of the cluster cut 70
5.5 ADC distribution of T4 before (solid) and after (dashed) the adc cut (Nakamori, 2008). 71
5.6 TDC distributions of T4 before (black-dotted) and after (red-solid) the image cleaning (Nakamori, 2008). 72
5.7 Event rates in cloudy (top) and clear (bottom) nights. 72
5.8 Schematic of the edge treatment. 73
5.9 Energy resolution for each edge treatment (Mizukami, 2007). 74
5.10 Angular resolution for each edge treatment (Mizukami, 2007). 74
5.11 Differential flux of RX J0852.0−4622 with the different edge treatment . . 75
5.12 Schematics of sine-weighted intersection point determination. 76
5.13 Dip and DISTANCE correlation for small and large zenith angle. 77
5.14 Parameters used in IP-fit. 78
5.15 Correlation between LENGTH/WIDTH and DISTANCE. 79
5.16 n value dependence against PSF (Nakamori, 2008). 79
5.17 Dip and DISTANCE correlation obtained by IP fit 80
5.18 θ^2 distributions with/without IP-fit 81
5.19 The WIDTH and LENGTH distributions of T4 for both background observation for Crab nebula and the gamma-ray simulation (Nakamori, 2008). 83
5.20 Correlation between LENGTH, WIDTH and ln(SIZE). 84
5.21 Fisher discriminant F distributions obtained by the HESS J1614−518 analysis. 85
5.22 The θ^2 plot obtained by HESS J1614−518 analysis. 86
5.23 The excess event number variation against different excess region taking . . 87
5.24 The obtained differential flux of HESS J1614−518. 89
5.25 Morphology of gamma-ray–like events. 90

6.1 Morphological relationship between the X-ray and gamma-ray observations for HESS J1614−518. 93
6.2 The IC emission curves for HESS J1614−518. 95
6.3 Interstellar radiation field from the GALPROP. 96

6.4 SED with synchrotron and IC emission curves for HESS J1614−518. 97
6.5 SED with Bremsstrahlung curves for HESS J1614−518. 98
6.6 SED and the model curve for neutral pion decay. 101
6.7 SED with synchrotron and IC emission curves with the PWN model for HESS J1614−518. 105

B.1 Integral frequency distributions 112

Chapter 1

Introduction

A final goal of my research is to clarify the origin of the galactic cosmic-ray. To explore the site of cosmic-ray acceleration, a TeV gamma-ray observation is a powerful tool since TeV gamma-rays are generated from the proximity of the particle acceleration site. While the cosmic-ray itself was bended by the interstellar magnetic field and has less information about their production site, the generated gamma-ray travels straight in the interstellar space and has more direct information about the production site.

1.1 Development of gamma-ray astronomy

Two strategies have been developed for the gamma-ray observation. One is satellite-based experiment, which detects low energy gamma-rays below $\sim$10 GeV directly out of the atmosphere. The other is ground-based experiment, which detects secondary productions from the interaction between high-energy gamma-rays above $\sim$10 GeV and atmospheric nuclei. The ground-based experiment indirectly detects the gamma-rays.

In 1970s and 1980s, the satellite-based experiments played an improtant role ahead of the ground-based experiment. By satellites like *SAS-II*, *COS-B*, and *CGRO*, the number of detected gamma-ray sources rapidly increases as shown in Fig.1.1. *Fermi* satellite launched in 2008 has been detecting more than a thousand sources, which is still increasing by further observations.

The very high energy (VHE) gamma-ray observation was introduced in 1970s by using atmospheric Cherenkov technique, which detects Cherenkov photons emitted by the high-energy gamma-ray at high altitude at the ground. Difficulty in this detection had been the identification of a primary particle. In 1980s, the introduction of imaging atmospheric Cherenkov technique (IACT) by Hillas (1985) opened a door to the next stage. In this

method, the Cherenkov photons were collected with a reflector and a shower image on the camera was parameterized to identify the primary particle. The detail of this method is summarized in Chapter 3.

Since the first detection of the VHE gamma-ray from Crab nebula by Whipple group (Weekes et al., 1989), the number of detected sources has been increasing as shown in Fig.1.1.

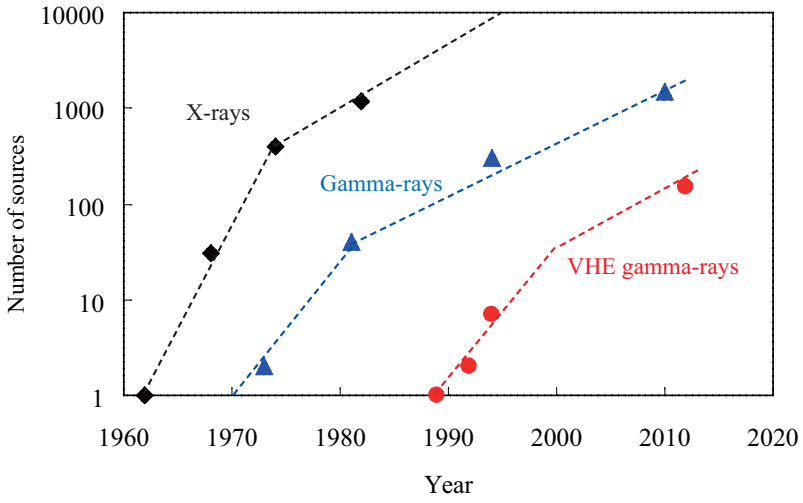

Figure 1.1 Number of detected high energy sources against years, which is called "Kifune plot".

1.2 Cosmic-ray

Since the discovery of cosmic-ray by Victor Hess in 1912, the origin of cosmic-ray has remained a mystery for a hundred years. Cosmic-rays consist mainly of primary protons, nuclei and electrons, which are accelerated to relativistic energies by powerful objects. The compositions of cosmic-ray around the earth are 90% the protons, 9% He, and 1% of heavy ions and electrons. Figure 1.2 shows the energy spectrum of cosmic-ray observed by satellites, balloon, and ground based detectors. The spectrum shows the non-thermal spectrum with the power law index of -2.7 below $\sim$1 PeV and -3.0 above $\sim$1 PeV, and extends up to 10^{20}eV. This broken energy is considered as the difference of its origin. Since most particles of cosmic-ray are charged particles, they were bended by the Lorentz

force by the interstellar magnetic field. The Larmor radius r of the particle is given as,

$$r = \frac{E}{ZeB} \sim Z^{-1} \left(\frac{E}{10^{15}\mathrm{eV}} \right) \left(\frac{B}{3\mu\mathrm{G}} \right)^{-1} \mathrm{pc}, \tag{1.1}$$

where Ze is the charge of the particle, B is the interstellar magnetic field, and E is the kinetic energy of the particle. Therefore, the particle of which energy is above ∼PeV run off from the galaxy, since their Lamor radius is larger than the thickness of the galactic disk (~ 300 pc). Here the origin of the galactic is cosmic-ray energetically estimated. A lifetime of the galactic cosmic-ray t_{CR} is obtained to be $\sim 2 \times 10^7$ years by a measurement of the existence ratio of ^{10}Be in the cosmic-ray (Garcia Munoz et al., 1977). The lifetime is determined by the escape of the cosmic-ray from the galaxy. Since the energy density of the cosmic-ray ρ_{CR} in the galaxy is estimated as ~ 1 eV cm^{-3}, the energy dissipation rate of the cosmic-ray L_{CR} is obtained as,

$$L_{\mathrm{CR}} = \frac{V_{\mathrm{G}} \rho_{\mathrm{CR}}}{t_{\mathrm{CR}}} \sim 3 \times 10^{40} \mathrm{erg\ sec}^{-1}, \tag{1.2}$$

where V_{G} is the volume of the galactic disk $V_{\mathrm{G}} \sim \pi(15\mathrm{kpc})^2(200\mathrm{pc}) \sim 4 \times 10^{66}$ cm^3 (Gaisser et al. , 1990). Supernova remnants (SNRs) are the candidate of this energy production. The rate of supernova explosion is estimated to be $\sim 1/30\mathrm{yr} \sim 10^{-9}$ sec^{-1}. Since a kinetic energy released by a typical supernova explosion is known to be $\sim 10^{51}$ erg, the supernova remnants has a possibility of producing the galactic cosmic-ray from the view of the energetic aspect when the conversion rate of kinetic energy to the cosmic-ray acceleration is $1 \sim 10$ %. Therefore, the detection of gamma-ray from SNRs and the discussion on its radiation mechanism are very important to discover the acceleration site of the galactic cosmic-rays.

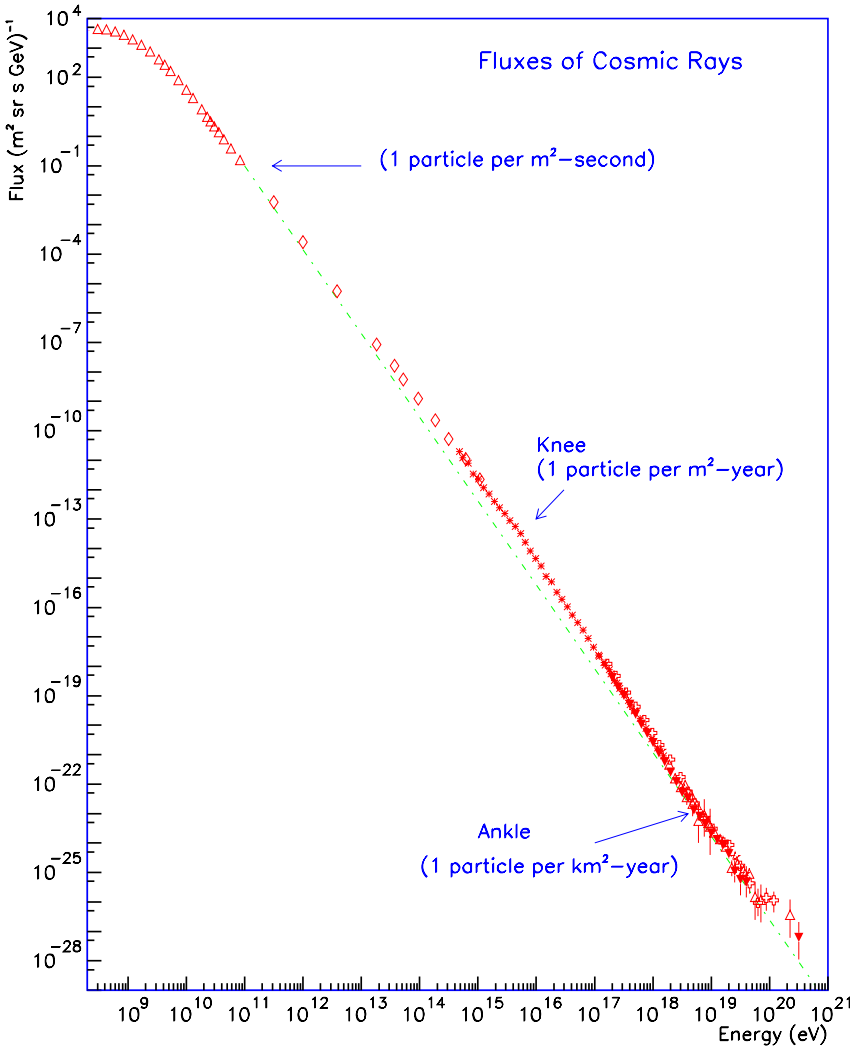

Figure 1.2 Energy spectrum of cosmic-ray.

Chapter 2

Very high energy gamma-ray emission in the galaxy

2.1 Mechanism of cosmic-ray acceleration

The mechanism of particle acceleration was originally introduced by Fermi (1949), which is known as "Second-order Fermi acceleration". However, in this original idea, the efficiency of acceleration was quite low, which led softer accelerated particle spectrum than that of cosmic-rays.

Instead of Fermi's original idea, more efficient acceleration mechanism in the shock fronts of the SNRs was introduced by Bell (1978) and Blandford & Ostriker (1978), which is known as "First-order Fermi acceleration".

Consider a process in which a charged particle increases its energy with each collision. A mechanism of such collision is described later. The energy of the particle after n collisions is given as,

$$E_n = E_0(1+\xi)^n \cong E_0 \exp(\xi n), \tag{2.1}$$

where E_0 is the initial energy of the particle, and ξ is the average energy gain per one collision. Considering a probability of escape of the particle from the acceleration region $P_{\rm esc}$ per one collision, a probability of remaining in the region after n collisions is obtained as $(1-P_{\rm esc})^n$. The number n which is necessary for the particle to reach energy E is obtained as,

$$n = \ln\left(\frac{E}{E_0}\right) / \ln(1+\xi). \tag{2.2}$$

Thus, the numbers of the particles accelerated to energies greater than E is calculated as,

$$N(\geq E) \propto \sum_{m=n}^{\infty} (1-P_{\rm esc})^m = \frac{(1-P_{\rm esc})^n}{P_{\rm esc}}, \tag{2.3}$$

$$= \frac{1}{P_{\rm esc}} \left(\frac{E}{E_0} \right)^{-\Gamma}, \tag{2.4}$$

$$\text{where} \Gamma = \ln \left(\frac{1}{1 - \mathrm{P_{esc}}} \right) / \ln(1 + \xi) \sim \frac{\mathrm{P_{esc}}}{\xi}. \tag{2.5}$$

Thus, a power law energy spectrum of the accelerated particles was obtained.

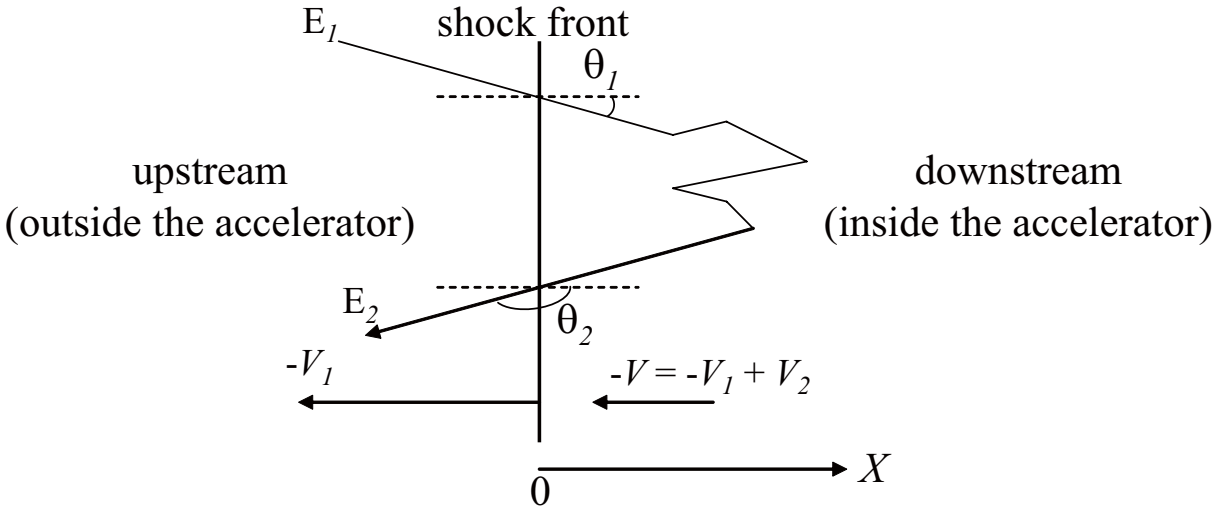

Figure 2.1 Schematic view of the acceleration at the shock front in the laboratory frame.

Fig.2.1 shows a schematic view of particle acceleration around a shock front in the laboratory frame. Suppose that the charged particles with an initial kinetic energy of E_1 come across the shock front with a velocity of $V = \beta c$. In the rest frame of the shock front, the energy of the accelerated particles is expressed as,

$$E_1' = \gamma E_1 (1 + \beta \theta_1), \tag{2.6}$$

where the prime denotes the quantity in the rest frame of the shock front, γ is the Lorentz factor, and $theta_1$ is the incident angle of the particle. By the multiple scattering with magnetic field in the downstream region, the fraction of particles crosses the shock front and goes into the upstream region again. The energy of the particle is expressed as,

$$E_2' = \gamma E_2 (1 + \beta \theta_2'). \tag{2.7}$$

Thus the energy gain with shock front is expressed as,

$$\frac{\Delta E}{E_1} = \gamma^2 (1 + \beta \cos\theta_1 \beta \cos\theta_2' - \beta^2 \cos\theta_1 \cos\theta_2') - 1, \tag{2.8}$$

where ΔE is $E_2 - E_1$. Assuming the isotropic intensity of the number of particles over the incident angles is given by I, the average of $\cos\theta_1$ is obtained as,

$$< \cos\theta_1 >= \frac{2\pi \int_0^1 \cos\theta \cdot I \cos\theta d(\cos\theta)}{2\pi \int_0^1 I \cos\theta d(\cos\theta)} = \frac{2}{3}. \tag{2.9}$$

$< \cos\theta_2'$ is obtained to be $-2/3$ similarly. Assuming the typical velocity of the shock front is $\sim$1000 km/s and thus $\beta \ll 1$, the averaged energy gain is approximated as,

$$\frac{\Delta E}{E_1} = \frac{4}{3}\frac{V_1 - V_2}{c}, \tag{2.10}$$

where V_1 and V_2 are the velocities of the upstream and the downstream region ($V = V_1 - V_2$). In the rest frame of the shock front, the flux of non-thermal particles penetrating into the shock front is given as,

$$\int_0^1 d\cos\theta \int_0^{2\pi} d\phi \frac{c\rho_{\rm part}}{4\pi}\cos\theta = \frac{c\rho_{\rm part}}{4}, \tag{2.11}$$

where $\rho_{\rm part}$ is the number density of particles undergoing acceleration. The flux of non-thermal particles which escape from the downstream region is $\rho_{\rm part} v_2$. Thus, the probability of escape $P_{\rm esc}$ is obtained as,

$$P_{\rm esc} = \frac{\rho_{\rm part} v_2}{c\rho_{\rm part}/4} = 4\frac{v_2}{c}. \tag{2.12}$$

Therefore, the power law index Γ of accelerated particle is calculated as,

$$\Gamma = \frac{P_{\rm part}}{\xi} = \frac{3}{v_1/v_2 - 1}. \tag{2.13}$$

The ratio v_1/v_2 can be estimated by the thermo-dynamics of thermal particles. In the rest frame of the shock front, conservation of mass, momentum, and energy are described as following expression,

$$\frac{\partial \rho}{\partial t} + \frac{\partial(\rho v)}{\partial x} = 0, \tag{2.14}$$

$$\frac{\partial \rho v}{\partial t} + \frac{\partial}{\partial x}(\rho v^2 + P) = 0, \tag{2.15}$$

$$\frac{\partial}{\partial t}\left(\frac{1}{2}v^2 + E\right) + \frac{\partial}{\partial x}\rho\left(\frac{1}{2}v^2 + E\right) + Pv = 0, \tag{2.16}$$

where ρ, v, P, and E are the density, velocity, pressure, and internal energy density which is the sum of the kinetic energies of thermal particles, respectively. Assuming a steady

state ($\partial/\partial t = 0$), the relations between the physical parameters in the upstream and in the downstream are given as,

$$\rho_1 v_1 = \rho_2 v_2, \tag{2.17}$$

$$\rho_1 v_1^2 + P_1 = \rho_2 v_2^2 + P_2, \tag{2.18}$$

$$v_1 \left(\rho_1 \left(\frac{1}{2}v_1^2 + E_1\right) + P_1\right) = v_2 \left(\rho_2 \left(\frac{1}{2}v_2^2 + E_2\right) + P_2\right). \tag{2.19}$$

Assuming the plasma behaves as an ideal gas, and using Mayer's relation, the energy E can be described as,

$$E = C_V T = \frac{C_V P}{nR\rho} = \frac{C_V}{C_P - C_V}\frac{P}{\rho} = \frac{1}{\gamma - 1}\frac{P}{\rho}, \tag{2.20}$$

where C_V, C_P, and γ are the molar heat at constant heat at constant volume and pressure, and the specific heat, respectively. Using the Mach number $M = v/\sqrt{\gamma P/\rho}$ in the adiabatic gas,

$$\left(1 - \frac{1}{r}\right)\gamma M_1^2 = s - 1, \tag{2.21}$$

$$\left(1 - \frac{1}{r^2}\right) M_1^2 = \frac{2}{\gamma - 1}\left(\frac{s}{r} - 1\right), \tag{2.22}$$

where $r = \rho_2/\rho_1 = v_1/v_2$ and $s = P_2/P_1$. Then r and s is obtained as,

$$r = \frac{(\gamma + 1)M_1^2}{(\gamma - 1)M_1^2 + 2}, \tag{2.23}$$

$$s = \frac{2\gamma M_1^2 - (\gamma - 1)}{\gamma + 1}. \tag{2.24}$$

For the case of strong shock approximation, $1 \ll M_1$, r is calculated as,

$$r = \frac{\gamma + 1}{\gamma - 1}. \tag{2.25}$$

By adopting γ of 5/3 for a mono atomic gas, the ratio is obtained to be 4 and corresponding index of the spectrum Γ is obtained to be 2, which is harder enough than the power-law index of the cosmic-ray.

2.2 Mechanism of gamma-ray emission

2.2.1 π^0 decay

When an accelerated nucleus comes to the bulk of matter like a molecular cloud, following nuclear reaction occurs,

$$p + p \rightarrow \pi^{\pm} + \text{anything},$$
$$\text{or}$$
$$p + p \rightarrow \pi^{0} + \text{anything}.$$

Then, the generated π^0 decays as,

$$\pi^0 \rightarrow 2\gamma,$$

and gamma-rays are generated. Detection of these gamma-rays could be a direct evidence of the cosmic-ray acceleration, since it originated from the high energy proton. $\pi^{\pm}$ are alos decay as,

$$\pi^{\pm} \rightarrow \mu^{\pm} + \nu_{\mu}/\bar{\nu_{\mu}} \rightarrow \mathrm{e}^{\pm} + \nu_{\mu}/\bar{\nu_{\mu}} + \nu_{\mu} + \bar{\nu_{\mu}}.$$

The generated $\mathrm{e}^{\pm}$ called secondary electron also contributes to gamma-ray emission through synchrotron, inverse Compton (IC), or Bremsstrahlung emission, which described in the following section. Since the rest mass of π^0 is $\sim$134 MeV, the generated gamma-rays have energies more than $\sim$70 MeV, which indicates that the gamma-ray observation is suitable for detecting this emission. Following Naito et al. (1994) calculation, the gamma-ray spectrum $F_{\gamma}(E_{\gamma})$ is given as,

$$F_{\gamma}(E_{\gamma}) = 2\int_{E_{\pi}^{\min}(E_{\gamma})}^{\infty} dE_{\pi} \frac{F_{\pi}(E_{\pi})}{\sqrt{E_{\pi}^2 - m_{\pi}^2)}}, \tag{2.26}$$

where E_{π} and m_{π} are the energy and mass of π_0, respectively, $F_{\pi}(E_{\pi})$ represents the spectrum of π_0, and $E_{\pi}^{\min}$ is the minimum energy of π_0. Then, $F_{\pi}(E_{\pi})$ can be calculated by kinematics of a collision of accelerated proton and target protons,

$$F_{\pi}(E_{\pi}) = 4\pi n_0 \int_{E_p^{\min}}^{E_p^{\max}} dE_p j_p(E_p) \frac{d\sigma_{\pi}(E_{pi}, E_p)}{dE_{\pi}} \tag{2.27}$$

where 4π comes from the assumption of the isotropic distribution of the protons, n_0 is the density of the target protons, $j_p(E_p)$ is the proton spectrum, $E_p^{\min}$, $E_p^{\max}$ are the minimum and maximum energy of the proton, and $d\sigma_{\pi}(E_{\pi}, E_p)/dE_{\pi}$ is the differential cross section of the proton against the pion.

Generally, the local cosmic-ray spectrum around the production site is described as a power-law spectrum with an exponential cut off as,

$$j_p(E_p) = \frac{dN_p}{dE_p} = K_p E_p^{-\Gamma_p} \exp(-E_p/E_p^{\max}), \tag{2.28}$$

where N_p is the number of the protons, K_p is the normalization factor, and Γ_p is the power law index of the proton spectrum. From the observed energy-dependence of the secondary to primary ratio of the cosmic-rays, Γ_p near the acceleration site is expected to be harder than 2.7 which is the power law index of cosmic-rays around the earth. Γ_p near the acceleration site is believed to have a value around 2.0 (e.g. Swordy (2001), which is also predicted by the first-order Fermi's acceleration, while the re-acceleration model of cosmic-rays in the interstellar medium predicts a value of 2.4 (Seo & Ptuskin, 1994).

2.2.2 Synchrotron emission

When the charged particles come to the magnetic field, they are bended by the Lorentz force and the photons are generated. When the charged particles are extremely relativistic, the frequency of the emitted photon spectrum extends to many times higher than the gyration frequency. This radiation is called the synchrotron emission.

I describe a simple estimation of the total emission power of the electron here, following (Rybicki, 1979). The motion of the particle of mass m and charge e in a magnetic field $\vec{B}$ is described as,

$$\frac{d}{dt}(\gamma m\vec{v}) = \frac{e}{c}\vec{v}\times\vec{B}, \tag{2.29}$$

$$\frac{d}{dt}(\gamma mc^2) = e\vec{v}\cdot\vec{B} = 0. \tag{2.30}$$

The second equation indicates that γ or $\vec{v}$ is the constant. Then, it follows,

$$m\gamma\frac{d\vec{v}}{dt} = \frac{e}{c}\vec{v}\times\vec{B}. \tag{2.31}$$

Separaing the velocity components to the component along the magnetic field $v_{\parallel}$ and normal to the field $v_{\perp}$, it follows,

$$\frac{dv_{\parallel}}{dt} = 0, \tag{2.32}$$

$$\frac{dv_{\perp}}{dt} = \frac{e}{\gamma mc}v_{\perp}B. \tag{2.33}$$

Thus, $v_{\parallel}$ =constant. Since the total velocity v is constant, $v_{\perp}$ is also constant. The projection of the motion of electron to the plane normal to the magnetic field is uniform circular motion. The frequency of this rotation is described as,

$$\omega_B = \frac{qB}{\gamma mc}. \tag{2.34}$$

Since the magnitude of the acceleration is

$$a = \omega_B v_\perp, \tag{2.35}$$

the total emitted radiation in the laboratory frame is obtained as,

$$P_{\rm synch} = \frac{2e^2}{3c^3}(\gamma^2 a)^2 \tag{2.36}$$

$$= \frac{2e^2}{3c^3}\gamma^4 \left(\frac{eB}{\gamma mc} v_\perp\right)^2 \tag{2.37}$$

$$= \frac{2}{3}\left(\frac{e}{mc^2}\right)^2 c\gamma^2 \beta_\perp^2 B^2, \tag{2.38}$$

where $\beta_\perp = v_\perp c$. For isotropic velocity distributions of electrons, the average $\beta_\perp$ is calculated as,

$$< \beta_\perp >= \frac{\beta^2}{4\pi}\int \sin^2\alpha d\Omega = \frac{2\beta^2}{3}, \tag{2.39}$$

where α is the angle between the magnetic field and the velocity, which is called the pitch angle. Thus, result is obtained as,

$$P_{\rm synch} = \left(\frac{2}{3}\right)^2 \left(\frac{e}{mc^2}\right)^2 c\gamma^2\beta^2 B^2 \tag{2.40}$$

$$= \frac{4}{3}\sigma_{\rm T} c\gamma^2\beta^2 U_B, \tag{2.41}$$

where $\sigma_{\rm T} = (8\pi/3)(e^2/mc^2)^2$ is the Thomson cross section, and $U_B = B^2/8\pi$ is the energy density of magnetic field.

2.2.3 Inverse Compton scattering

When relativistic electrons collide with low energy photons, the photons are scattered by Inverse Compton (IC) scattering.

In the electron-rest frame, the photon space distribution $n(p)$ and the energy of the photons v are related as,

$$v d\epsilon = n d^3 p, \tag{2.42}$$

where p is the momentum of the photons. Transformation to the laboratory frame are described as,

$$\epsilon = \gamma\epsilon', \tag{2.43}$$

$$d^3 p = \gamma d^3 p', \tag{2.44}$$

where ϵ' and p' are the energy and momentum of the photons in the laboratory frame, respectively, and γ is the Lorentz factor. Then, considering the term $vd\epsilon/\epsilon$ is a Lorentz invariant,

$$\frac{vd\epsilon}{\epsilon} = \frac{nd^3p}{\epsilon} = \frac{\gamma nd^3p'}{\gamma\epsilon'} = \frac{v'd\epsilon'}{\epsilon'}. \tag{2.45}$$

The total power emitted in the electron-rest frame is calculated from,

$$\frac{dE'_{\rm scat}}{dt'} = c\sigma_{\rm T}\int \epsilon'_{\rm scat}v'd\epsilon', \tag{2.46}$$

where $\sigma_{\rm T}$ is the Thomson cross section. From the Doppler shift formula, $\epsilon = \epsilon\gamma(1-\beta\cos\theta)$, following equation is obtained,

$$\frac{dE_{\rm scat}}{dt} = c\sigma_{\rm T}\gamma^2\int(1-\beta\cos\theta)^2\epsilon vd\epsilon. \tag{2.47}$$

For an isotropic distribution of the photons,

$$< (1-\beta\cos\theta)^2 >= 1+\frac{1}{3}\beta^2, \tag{2.48}$$

since $<\cos\theta>=0$ and $<\cos^2\theta>=1/3$. Thus,

$$\frac{dE_\prime}{dt} = c\sigma_{\rm T}\gamma^2\left(1+\frac{1}{3}\beta^2\right)U_{\rm ph}, \tag{2.49}$$

where $U_{\rm ph}$ is the initial photon energy density,

$$U_{\rm ph} = \int \epsilon vd\epsilon. \tag{2.50}$$

The total energy loss of the initial photon field is

$$\frac{dE{\rm init}}{dt} = -c\sigma_{\rm T}\int\epsilon vd\epsilon = -\sigma_{\rm T}cU_{\rm ph}. \tag{2.51}$$

Thus, the net energy loss of the electron or radiation by the IC scattering is

$$< P_{\rm IC} >= \frac{dE_{\rm scat}}{dt} - \frac{dE_{\rm init}}{dt} = \frac{4}{3}\sigma_{\rm T}c\gamma^2\beta^2U_{\rm ph}. \tag{2.52}$$

A ratio between synchrotron emission and IC scattering is now obtained as,

$$\frac{P_{\rm sync}}{P_{\rm IC}} = \frac{U_{\rm B}}{U_{\rm ph}}. \tag{2.53}$$

Thus, once the electron distribution and the photon field is fixed, the flux ratio of the synchrotron to IC emissions are depends only on a magnetic field.

2.2.4 Bremsstrahlung

When charged particles come to the bulk of matter, photons are emitted by an deceleration of the charged particles by the Coulomb field of the nucleus. This is called Bremsstrahlung. The cross section and the emitted power of Bremsstrahlung are same as those of synchrotron radiation. The emitted power is proportional to $1/m^2$, where m is the rest mass of the charged particle. Therefore, Bremsstrahlung is more important in the accelerated electrons than the hadrons.

2.3 The galactic VHE gamma-ray sources

Continuous efforts and steady improvements on IACTs have increased the number of detected sources up to 142 (TeVCAT ver.3.100, 2012). 86 of 142 sources are regarded as galactic. Figure 2.2 shows a classification of the galactic sources. The major part of the galactic sources was a pulsar wind nebula (PWN), the second was an unidentified source, and the third was a supernova remnant (SNR). These three objects dominates 92% of the galactic sources. In this section, I review those galactic sources.

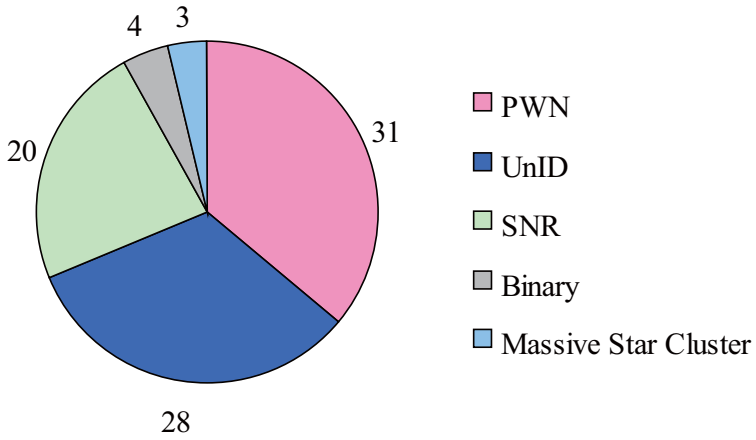

Figure 2.2 Classification of the galactic sources.

2.4 Supernova Remnant

As described in Chapter 1, the SNRs have been considered to be a unique candidate of the accelerator of the galactic CRs up to 100 TeV. VHE gamma-rays have been detected

from young SNRs such as RX J1713.7−3946 (Muraishi et al., 2000; Enomoto et al., 2002a; Aharonian et al., 2006c), RX J0852.0−4622 (Katagiri et al., 2005; Aharonian et al., 2005c; Enomoto et al., 2006b), RCW86 (Watanabe et al., 2003; Aharonian et al., 2009), and SN 1006 (Acero et al., 2010) which show possible evidences of the cosmic-ray acceleration site (e.g., Enomoto et al., 2002a; Malkov et al., 2005; Uchiyama et al., 2007; Tanaka et al., 2008; Yamazaki et al., 2009). Figure 2.3 shows the gamma-ray excess map for SN 1006 obtained by H.E.S.S. group (Acero et al., 2010), for example. The VHE gamma-ray map shows very close correlation with the X-ray map. The bipolar morphology of the emission region supports a diffusive shock acceleration theory. According to the theory, efficient downstream injection of charged ions is only possible for small angles between the magnetic field and shock normal. Assuming a uniform magnetic field, a higher density of accelerated nuclei at the both poles is predicted (Ellison et al., 1995). Three different models were investigated to account for the spectral energy distribution (SED) which were shown in Fig.2.4. In a leptonic model, the TeV emission results from IC scattering. In a hadronic model, TeV emission results from π_0 decay. The magnetic field is required to be higher than 120 μG, which is consistent with magnetic field amplification at the shock, indicated by X-ray thin filament structure. However, this model requires a very high energy conversion efficiency of 20% from a typical supernova kinetic energy of 10^{51} erg. In a mixed model for leptonic and hadronic, this problem on energy conversion efficiency was sufficiently reduced to 12%.

2.5 Pulsar Wind Nebula

Detections of VHE gamma-rays from PWNe such as the Crab nebula (Weekes et al., 1989) and Vela X nebula (Aharonian et al., 2006b; Enomoto et al., 2006a) have shown that PWNe also play an important role in particle acceleration in the Galaxy.

A pulsar is a fast rotating neutron star. Neutron stars are formed in a gravitational collapse type of the supernova explosion of a massive star ($M > 10M_{\odot}$). The typical mass and radius is $\sim 1.4M_{\odot}$ and $\sim$ 10 km, respectively, and it supports itself against the gravitational force by a degenerate pressure of neutron. The relativistic plasma is accelerated and flows out from its magnetosphere, which is called "Pulsar wind". The pulsar wind collides with the interstellar matter (ISM) and forms shock wave. The charged particles are expected to be accelerated in the shock. The schematic structure of the pulsar wind nebula is shown in Fig.2.5.

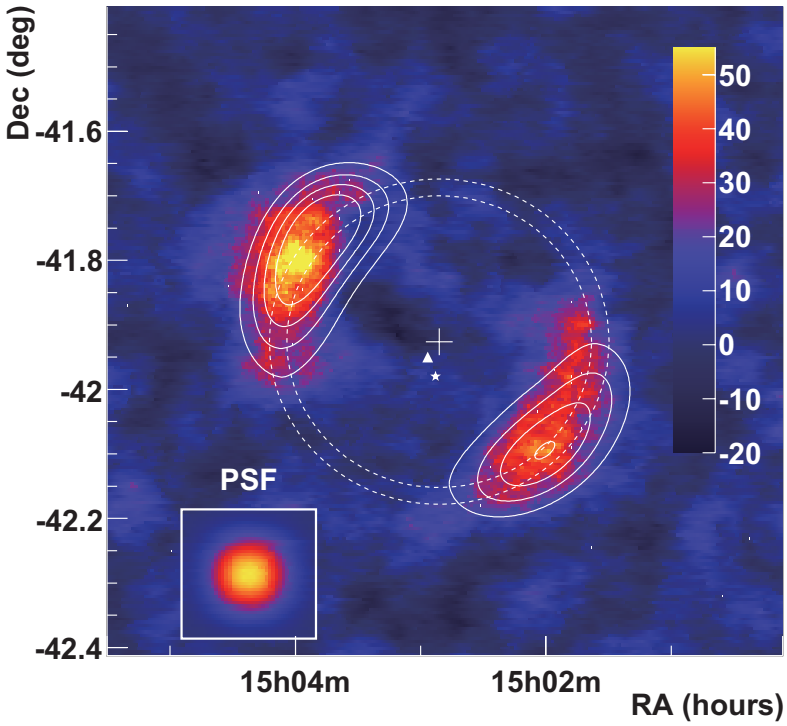

Figure 2.3 Gamma-ray excess map of SN 1006 obtained by H.E.S.S. (Acero et al., 2010). The white contours correspond to a X-ray intensity as derived from the XMM-Newton flux map.

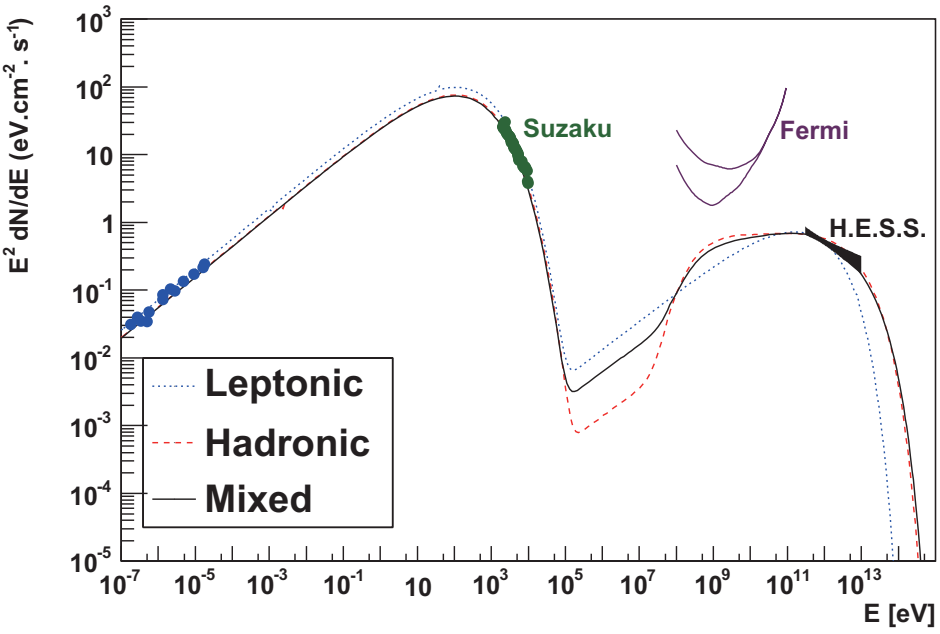

Figure 2.4 SED predicted for SN 1006.

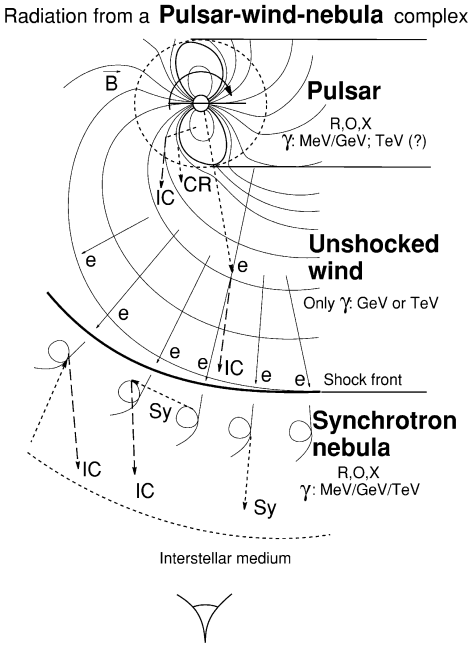

Figure 2.5 Schematic view of a pulsar system (Aharonian & Bogovalov, 2003).

2.6 Massive Star Cluster

VHE gamma-ray emission related to the stellar clusters Cyg OB2 (Aharonian et al., 2002), Westerlund 2 (Aharonian et al., 2007), and Westerlund 1 (Ohm et al., 2010) have also been reported.

The VHE gamma-ray emission origin of the stellar cluster is rather complicated. While supernova remnants or pulsar wind nebulae of the cluster has possibility origin of the emission, it is possible for the strong and fast stellar wind from the massive stars to accelerate particles up to the VHE gamma-ray energies. In the later scenario, The stellar winds of massive stars interact with each other and lead to the formation of wind-blown bubbles, filled with a low-density hot plasma (Voelk & Forman, 1982) in which diffusive shock acceleration can occur (Klepach et al., 2000).

2.7 Binary systems

VHE gamma-rays were detected from 4 binary systems: PSR 1259−63/SS 2883, LS 5039, LS I+61 303, and Cyg X-1. The binaries consist of a compact object such as a neutron star or black hole and a companion star orbiting around the compact object. The schematic view of the binary system is shown in Fig.2.6. Modulation of the radiation is linked to the orbital motion of the binary system. Figure 2.7 shows a VHE gamma-ray periodogram of LS 5039 obtained by H.E.S.S. (Aharonian et al., 2006a). The period was consistent with the orbital period reported by Casares et al. (2005). Orbital modulation of the VHE spectrum are shown in Fig.2.8. This modulation was interpreted as the result of phase-dependent pair creation on the stellar photon field when the compact object is behind the companion star, leading to a significant absorption of the VHE flux at the superior conjunction.

2.8 Unidentified VHE Gamma-ray source; HESS J1614−518

The Galactic plane survey performed by the H.E.S.S. observatory (Aharonian et al., 2005b, 2006a) discovered seventeen unidentified VHE gamma-ray sources, including HESS J1614−518. Figure 2.9 shows the galactic objects revealed by the first galactic plane survey by H.E.S.S.. Today, unidentified sources are one of the largest class of the 142 discovered

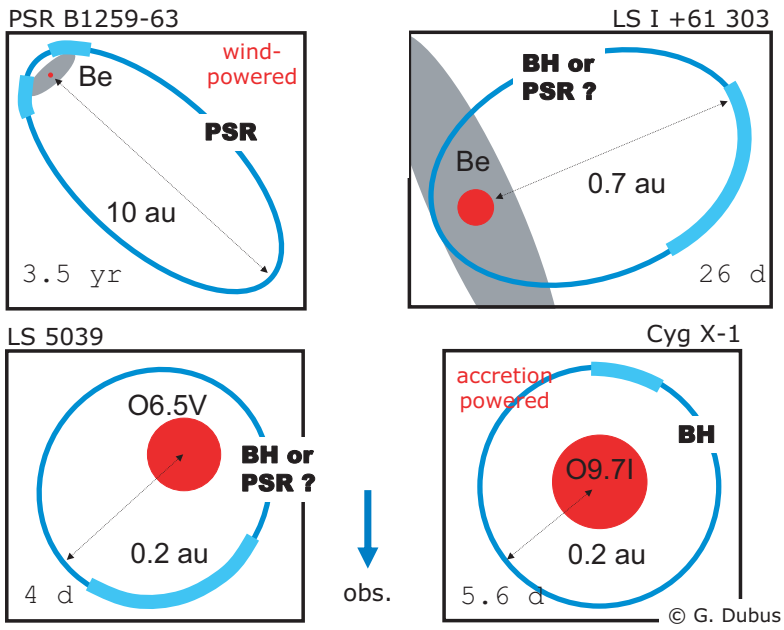

Figure 2.6 Schematic views of the binary systems detected by VHE gamma-rays (Hinton, 2007).

VHE gamma-ray sources, most of which are located in the Galactic plane (e.g., Aharonian et al. (2005d); Abdo et al. (2007); Aharonian et al. (2008); the TeVCAT catalog, TeVCAT ver.3.100 (2012), is a useful up-to-date, on-line resource). In general, the lack of non-thermal electromagnetic radiation from the radio to the X-ray bands may be an evidence of hadron acceleration because the IC scenario requires a lower magnetic field than the typical interstellar magnetic field intensity of a few μG. Revealing the possible radiation mechanism(s) of each unidentified source is therefore important for identifying the origin(s) of cosmic rays.

H.E.S.S. reported that HESS J1614−518 had a high flux level, 25% of the Crab nebula, above 200 GeV with a photon index of 2.4 and an elliptical morphology with a semi-major axis of 14 ± 1 arcmin and a semi-minor axis of 9 ± 1 arcmin (Aharonian et al., 2006a). The peak position has an offset of 8.7 arcmin to the north-east from the central position. Figure 2.10 shows the morphology of HESS J1614−518 obtained by H.E.S.S.. Landi et al. (2007) and Rowell et al. (2008) pointed out that HESS J1614−518 may be associated with the 40 Myr-old young open star cluster Pismis 22 (Piatti et al., 2000) which is located within the VHE gamma-ray emission region at a distance of 1.0 ± 0.4 kpc and has

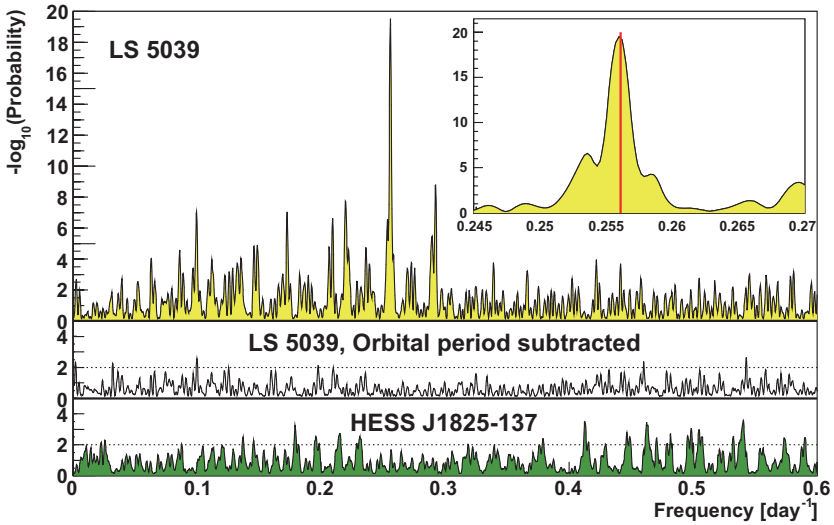

Figure 2.7 **Top:** Lomb-Scargle (LS) periodogram of the VHE runwise flux for LS=5039. Inset: zoom around the highest peak. **Middle:** LS periodogram of the same data after subtraction of a pure sinusoidal component at the orbital period. **Bottom:** LS periodogram of the HESS J1825−137. (Taken from Aharonian et al. (2006a).)

sufficient luminosity to produce the observed gamma-ray luminosity, assuming 20% energy conversion from the stellar winds of ten B-type stars. However, there are several issues in identifying HESS J1614−518 with Pismis 22 since the size of Pismis 22, 2.0 arcmin in diameter, is one order of magnitude smaller than the VHE gamma-ray emission size and the location has a 12 arcmin offset from the VHE gamma-ray emission peak. In addition, there has been no detailed discussion of the radiation mechanism.

The X-ray satellite *Suzaku* observed this region with the X-ray imaging spectrometer (XIS) and found three X-ray sources in their follow-up observation in 2006 (Matsumoto et al., 2008). The region of *Suzaku* observation and the obtained X-ray map are shown in Fig.2.11 and Fig.2.12, respectively. One of these, called Suzaku source A, is located very close to the VHE gamma-ray peak position with an offset of 0.8 arcmin. The spectrum is well fitted by a single power-law model with a photon index of $1.73^{+0.33}_{-0.30}$ and a hydrogen equivalent column density of $1.21^{+0.50}_{-0.41} \times 10^{22}$ cm^{-2} as shown in Fig.2.13. The distance to Suzaku source A is approximately 10 kpc, which was derived from the hydrogen equivalent column density using the total Galactic H I column density toward HESS J1614−518 of $\sim 2.2 \times 10^{22}$ cm^{-2} (Dickey & Lockman, 1990). The size of the X-ray emission region is slightly larger than the *Suzaku* Point Spread Function (PSF) of 1.8 arcmin and smaller

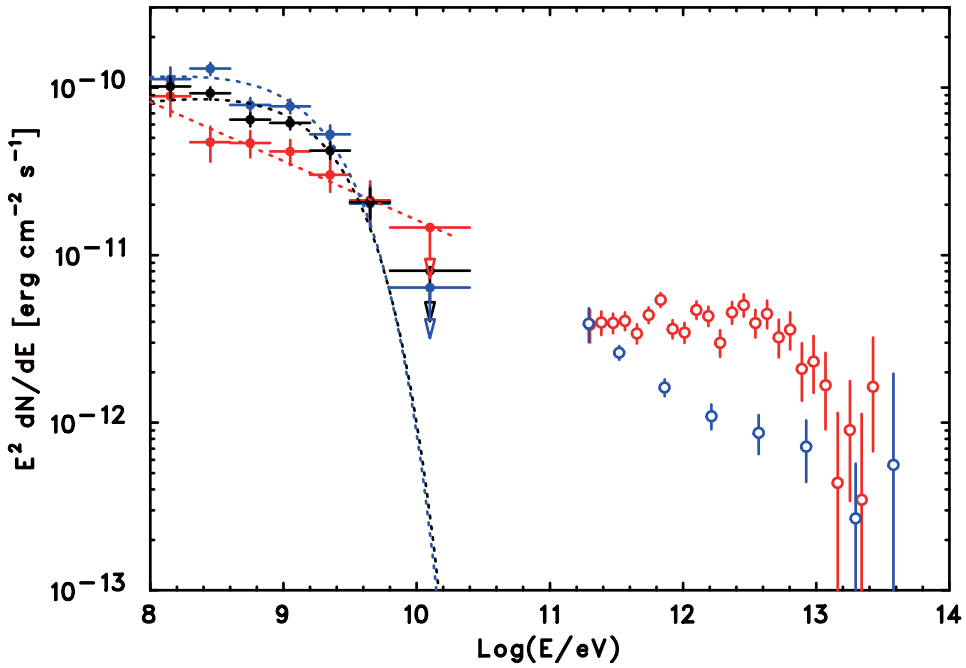

Figure 2.8 Phase resolved SED of LS 5039 with *Fermi* and H.E.S.S. data. The black points and dotted line represent the phase-averaged spectrum. The red points and dotted line represent the spectrum at inferior conjunction. The blue points and dotted line represent the spectrum at superior conjunction.(Taken from Aharonian et al. (2006a).)

than the size of the VHE gamma-ray region. Such a difference is also seen in PWNe such as HESS J1825−137 (Aharonian et al., 2006d; Uchiyama et al., 2009) and Vela X (Markwardt & Ogelman, 1995; Aharonian et al., 2006b) and could be explained by the difference between the synchrotron cooling time of the electrons that radiate X-rays and those that produce TeV gamma rays.

Electrons with an energy of 100 TeV radiate X-rays and immediately lose their energy by synchrotron cooling (e.g., the energy-loss timescale is $\sim 10^2$ yr assuming a magnetic field of 20 μG (Sturner et al., 1997)), while electrons with an energy of 1 TeV, which are responsible for the VHE gamma ray emission through IC scattering, are more slowly cooled by synchrotron radiation (e.g., the energy-loss timescale is $\sim 10^4$ yr assuming the same parameters as above) and can travel further from their source. However, the ratio between the observed VHE gamma-ray and X-ray fluxes, F(1–10 TeV) / F(2–10 keV) of ∼34, is much larger than those of known PWNe — 2.6×10^{-3}, 0.7, and 1.5 for the Crab, MSH 15-52, and Vela X, respectively (Gaensler et al., 1999; Willingale et al., 2001;

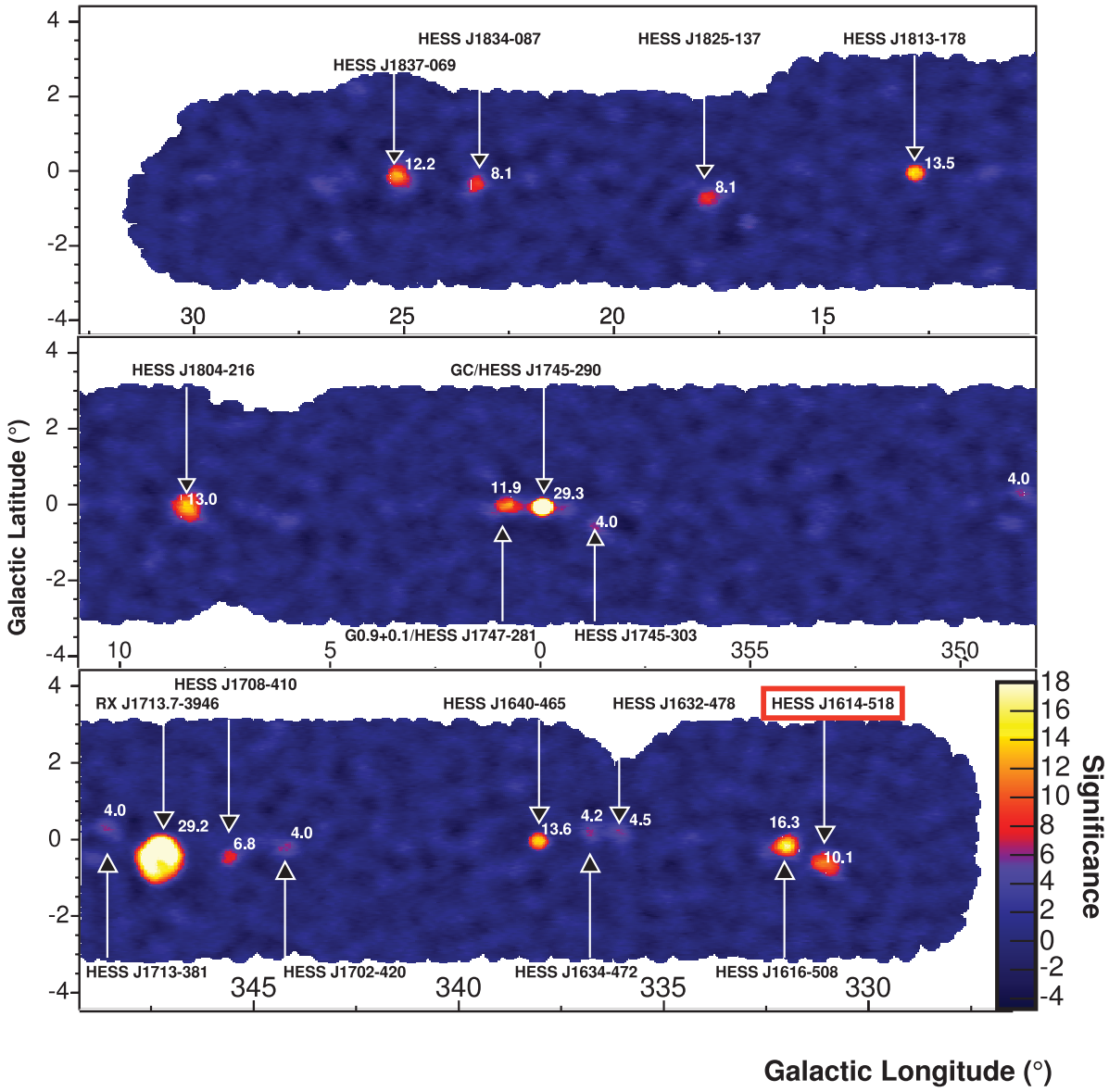

Figure 2.9 The gamma-ray population in the galactic plane observed by H.E.S.S. (Aharonian et al., 2006a).

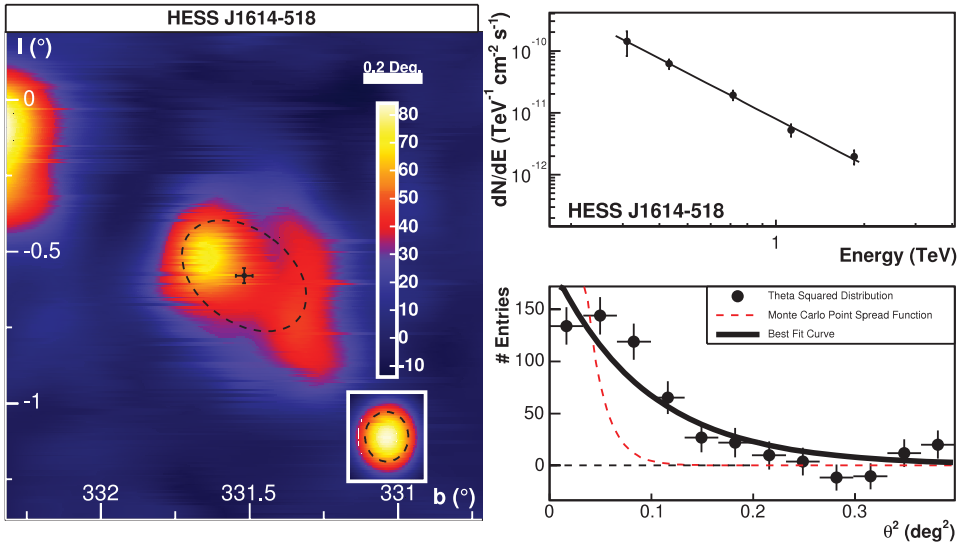

Figure 2.10 Left: Smoothed excess map (smoothing radius 0°.09) of the region of HESS J1614−518. Right: Energy spectrum (top) and θ^2 plot (bottom). Description of the θ^2 plot is mentioned in analysis chapter.

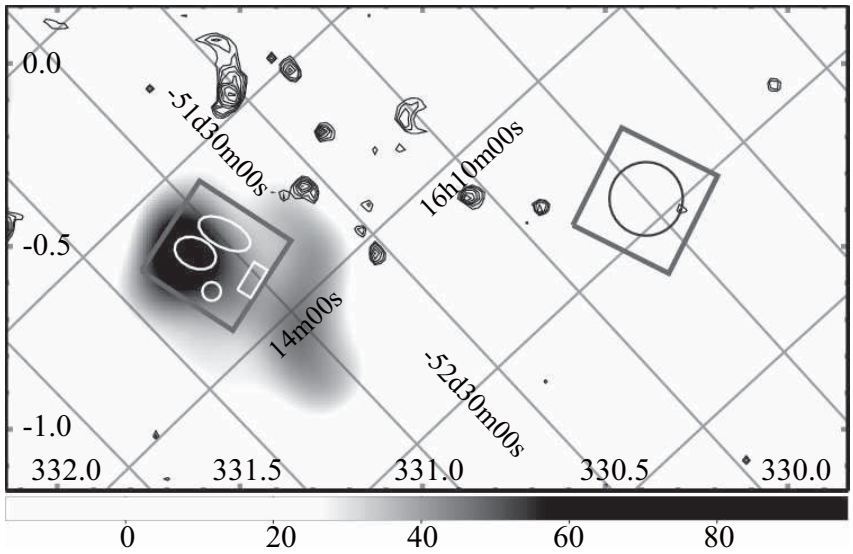

Figure 2.11 Suzaku fields of view (thick boxes) overlaid on the H.E.S.S. smoothed excess map. The scale baar below the figure represents the excess. The coordinates on the exterior frame are Galactic, while the grid shows the equatorial coordinates (J2000.0).

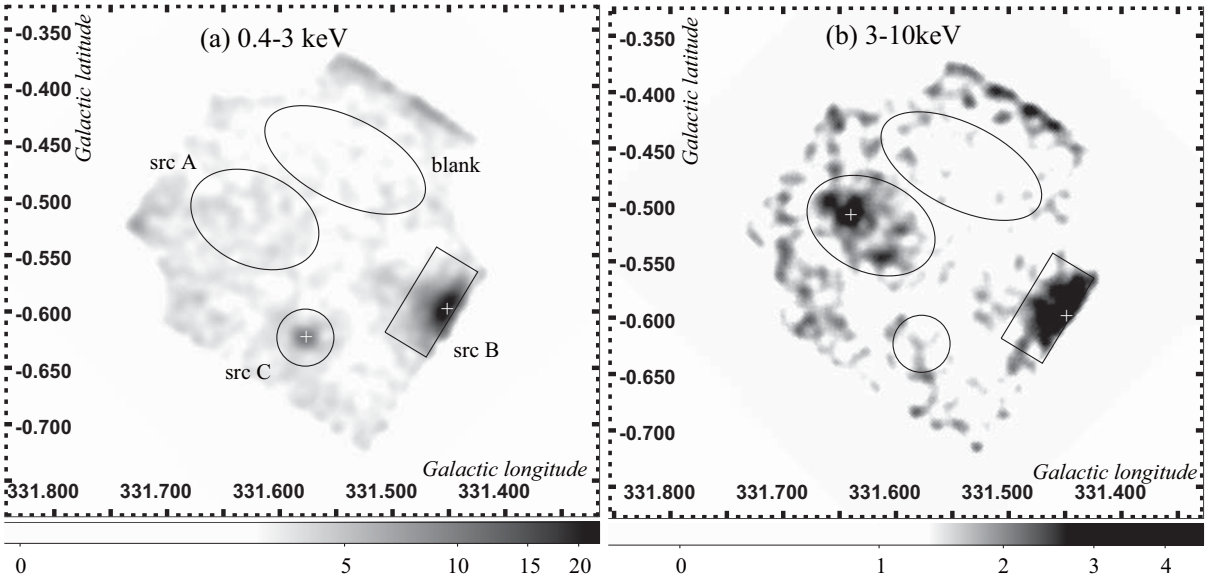

Figure 2.12 Suzaku XIS images of the HESS J1614−518 region: (a) 0.4−3 keV and (b) 3−10 keV band.

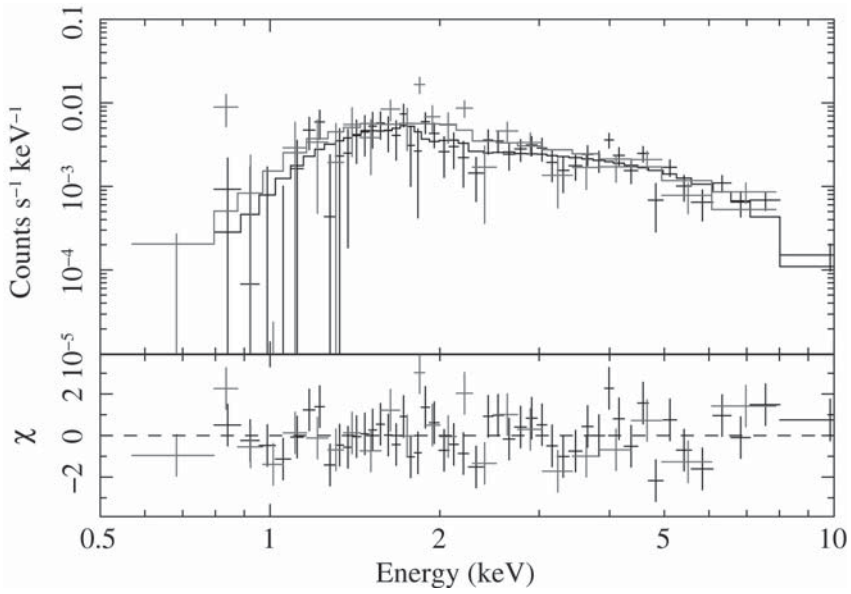

Figure 2.13 XIS spectra of source A and the best-fit power-law model.

Gaensler et al., 2002; Dodson et al., 2003; Aharonian et al., 2004, 2005a, 2006b; Manzali et al., 2007; Nakamori et al., 2008). Nevertheless, recent studies of HESS J1640−465 (Funk et al., 2007) and HESS J1804−216 (Higashi et al., 2008) claim that this large ratio can be explained by a time-evolving electron injection model, in which the number of electrons injected into space by the pulsar decreases proportionally to the spin-down of the pulsar. On the other hand, this large ratio is also expected in an old SNR with an age of $\sim 10^5$ yr, because of the difference between the cooling times of electrons and protons (Yamazaki et al., 2006). I therefore discuss both a PWN scenario and an SNR scenario in Chapter 6.

Suzaku source B is positioned towards the center of HESS J1614−518 and is coincident with the position of Pismis 22. Since the hydrogen equivalent column density derived from the Suzaku spectrum is $(1.1 \pm 0.21) \times 10^{22}$ cm^{-2}, which is comparable with that of Suzaku source A, Suzaku source B may lie at a similar distance as for Suzaku source A. This source has a non-thermal X-ray emission with a photon index of 3.19 ± 0.32. This soft index and X-ray luminosities of 7.7×10^{34} ergs s^{-1} and 4.5×10^{35} ergs s^{-1} in the 2−10 keV and 0.5−10 keV ranges, respectively, assuming a distance of 10 kpc, are typical values for an anomalous X-ray pulsar (AXP) (Fahlman & Gregory, 1981; Kuiper et al., 2006). The possible existence of the AXP also suggests this source as an SNR, since AXPs are usually associated with SNRs, e.g., 1E 2259+586 with CTB 109 (Fahlman & Gregory, 1981) and 1E 1841−045 with Kes 73 (Vasisht & Gotthelf, 1997). Since the position of this source is coincident with Pismis 22, there is a possibility that this emission originates from the stellar winds from the stellar cluster. Non-thermal X-ray emission from a stellar cluster was reported from Westerlund 1 (Muno et al., 2006), and TeV gamma rays were recently detected from this object (Ohm et al., 2009). However, this positional correlation may be only a chance coincidence since the estimated distances to Suzaku source B and Pismis 22 are different by an order of magnitude. Although Suzaku source B might be marginally extended, it is difficult to quantitatively estimate the spatial extension with the Suzaku PSF of 1.8 arcmin. If Suzaku source B is actually extended, additional scenarios besides an SNR could be considered, e.g., a PWN from a pulsar/AXP as discussed in Matsumoto et al. (2008), or emission from the unresolved hot stars in Pismis 22.

The other source, Suzaku source C, is a late B-type star as described in Matsumoto et al. (2008), and thus is not a possible counterpart of HESS J1614−518.

Swift observed this region with the X-ray telescope (XRT) and found six X-ray sources (hereafter Swift sources 1 to 6) (Landi et al., 2006, 2007) with a larger FoV than that of *Suzaku*. Figure 2.14 shows the swift source map. All these sources were point-like and no

diffuse emission was found. Two sources, Swift sources 1 and 4, are located within the field of view (FOV) of the *Suzaku* observation. Swift source 1 is located close to Pismis 22 with an offset of 42 arcsec. This source is also coincident with Suzaku source B. Swift source 4 is coincident with Suzaku source C. Swift sources 1, 2, 3, 5 are probably stars, while the nature of Swift sources 4 and 6 were not identified, probably due to the poor statistics. Although Suzaku source A was located in the FOV of the *Swift* XRT, it was not detected with *Swift* probably due to the limited exposure time (∼1700 s) and/or the small effective area.

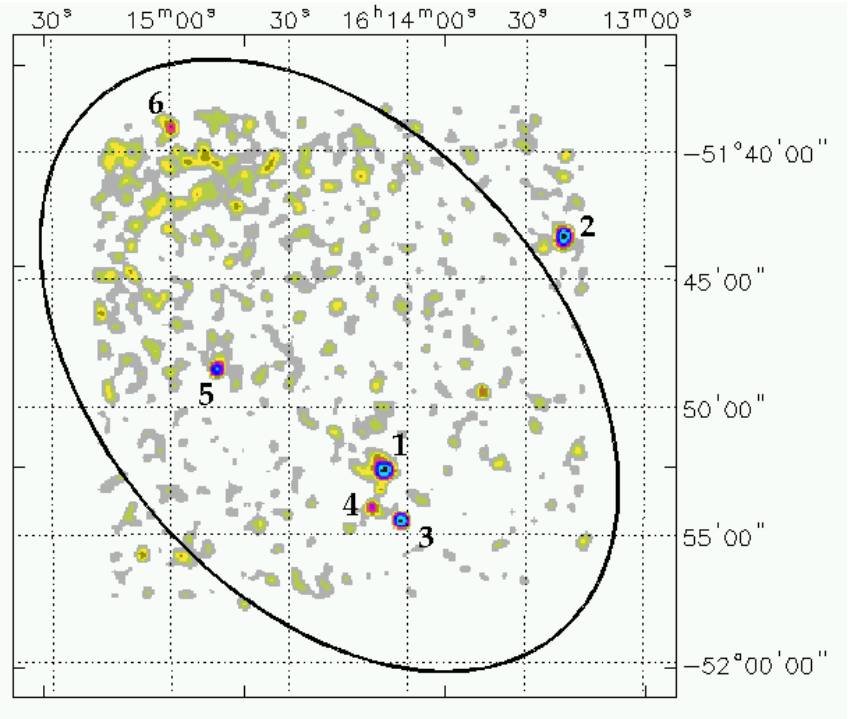

Figure 2.14 Swift source map for HESS J1614−514 region. The extent of HESS J1614−514 obtained by H.E.S.S. is shown by ellipse line.

The Fermi-LAT collaboration (Abdo et al., 2010a) reported the detection of gamma rays in the 100 MeV to 100 GeV band from 1FGL J1614.7-5138c positioned 2.7 arcmin away from the peak position of the VHE gamma-ray emission. Furthermore, the recent analysis for a diffuse emission applied to the *Fermi* data by Lande et al. (2012). They report a harder and stronger emission than the previous result as shown in Fig.2.15, although which will not change our discussion significantly.

In the radio band, no counterpart has been found in the HESS J1614−518 region; there

is no enhancement in the 843 MHz band, where the rms noise level is $\sim$2 mJy arcmin^{-2} (Bock et al., 1999; Murphy et al., 2007). In this paper, we present TeV gamma-ray observations of HESS J1614−518 with the CANGAROO-III telescopes and discuss the possible counterpart and the radiation mechanism by considering multi-wavelength observations.

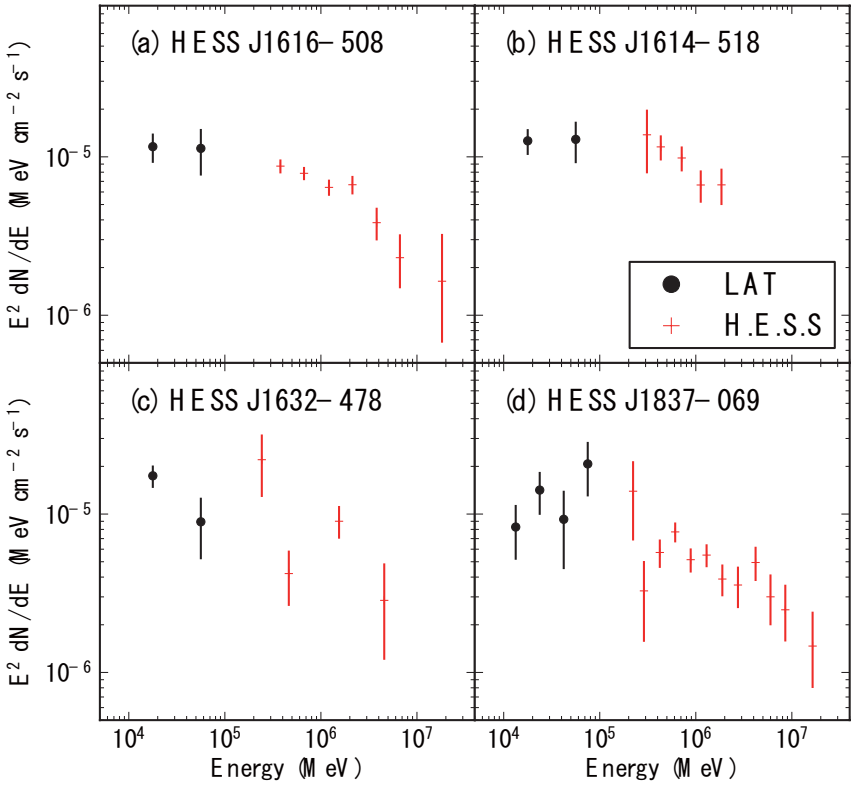

Figure 2.15 The spectrum given by Lande et al. (2012) for HESS J1614−518 (right top).

Chapter 3

Imaging Air Cherenkov Technique

High energy photons such as X-rays or gamma-rays from the space cannot reach the ground since they are absorbed by the atmosphere. Furthermore, VHE gamma-rays are hardly detected by balloon-borne or satellites instrument due to its low flux. For example, the integral flux of Crab nebula above 1 TeV is $\sim 10^{-11}$ photons cm^{-2} s^{-1}, which means that 10^7 s exposure time is required for detecting a VHE photon with an effective area of 1 m^2. Therefore, a technique called an Imaging Air Cherenkov Technique (IACT) has been developed to detect Cherenkov photons from an Extensive Air Shower (EAS) generated by an interaction between the VHE gamma-ray and the atmosphere. In this technique, the atmosphere works as a detector. Emitted Cherenkov photons spread over $\sim 100^2$ m^2 radial area, and then we detect them using a reflector in this area, which gives us a typical effective area of IACT reaches an order of 10^5 m^2.

3.1 Extensive Air Shower

When a high energy particle comes to the atmosphere, the particle interacts with a nucleus of the atmosphere and generates secondary particles. These secondary particles also interact with the atmosphere and generate more particles. These particles forms "shower" which is called an EAS. An EAS generated by a primary gamma-ray grows only by electromagnetic cascade. First, a primary gamma-ray photon produces a electron-positron pair. These electrons/positrons emit secondary gamma-rays by Bremsstrahlung, and then these gamma-rays produce furthermore electrons/positrons successively. By repeating these processes, the EAS is generated. Figures 3.1 and 3.2 show schematic diagrams of the EAS and a number of particles included in the EAS, respectively. Electrons/positrons lose their energy as the EAS develops. When each energy of an electron or positron is

decreased below 84 MeV the development of the EAS stops its development since the energy-loss process becomes dominated by ionization loss rather than Bremsstrahlung below this energy. This energy is called a critical energy. The number of the particle in the EAS reaches the maximum at this energy. Cosmic-ray hadrons also generate EAS. In this case, an EAS is developed through a nuclear cascade. When a high energy hadron comes to the atmosphere, the hadron interacts with a nucleus of the atmosphere and produces high energy nucleons. These nucleons make collisions with the atmospheric nucleus and produce many species of secondary particles such as nucleons, neutral pions, charged pions and kaons. The neutral pions have a shorter decay time of 0.83×10^{-16} sec and immediately decay to two gamma rays,

$$\pi^0 \rightarrow 2\gamma,$$

and these gamma rays generate electromagnetic cascade. On the other hand, a high energy ($\gg$ 10 GeV) charged pion does not decay since their decay time is expanded by a relativistic effect and produces further particles through collision with an atmospheric nucleus. A lower energy charged pion decay into a muon,

$$\pi^+ \rightarrow \mu^+ + \nu_\mu,$$
$$\pi^- \rightarrow \mu^- + \bar{\nu_\mu},$$

with the mean lifetime of 2.6×10^{-8} sec. Muons decay into electron/positrons,

$$\mu^+ \rightarrow e^+ + \nu_e + \bar{\nu_\mu},$$
$$\mu^- \rightarrow e^- + \bar{\nu_e} + \nu_\mu,$$

with the mean lifetime of 2.2×10^{-6} sec. Since this lifetime is long, these muons rarely decay and reach to the ground. Interactions involved in a nucleonic cascade are illustrated in Fig.3.3. There are several differences in the development of the EAS between the gamma-ray shower and nucleonic showers. First, the nucleonic shower initiates in the deeper atmosphere because of the longer interaction length than that in the radiation length. Second, nuclear cascades have larger transverse momenta than these of electromagnetic cascades. Thus, the nucleonic shower is extended more transversely than that of the gamma-ray shower. We can distinguish the gamma-rays from the background hadrons by these features.

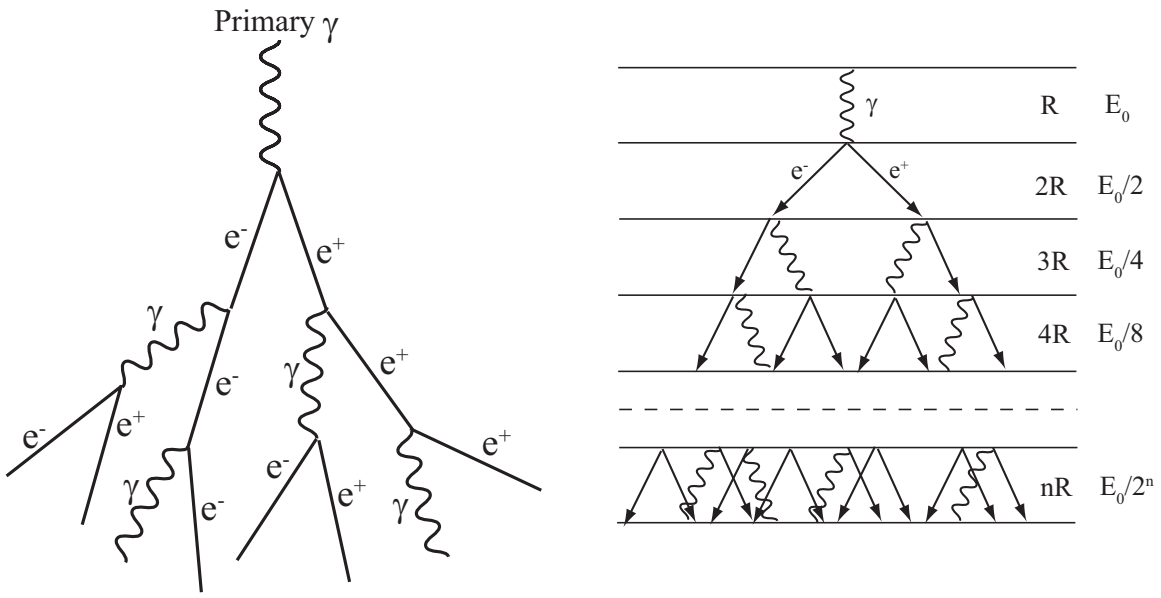

Figure 3.1 **Left**: Schematic diagram of an electromagnetic cascade shower. **Right**: Simple model of an electromagnetic shower. $R = \xi/\rho$ is a radiation length of electrons/positrons or a mean free path of a gamma ray, with a dimension of the length.

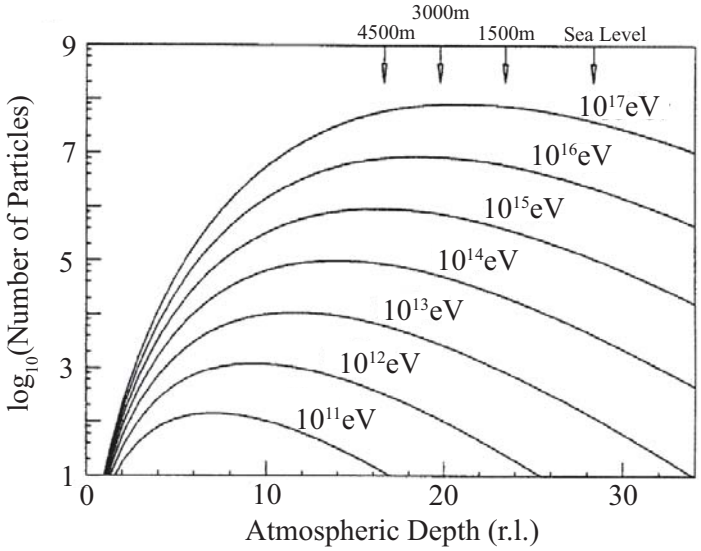

Figure 3.2 The number of particles in an EAS by gamma rays.

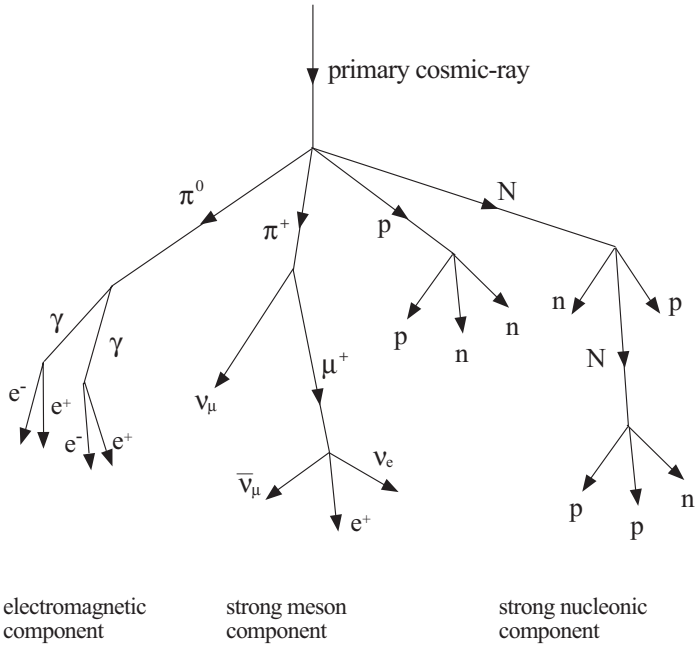

Figure 3.3 Schematic diagram of the development of a nucleonic cascade in the atmosphere.

3.2 Cherenkov Radiation

When a charged particle has a larger velocity than that of light in a medium with a reflective index of n, it radiate photons. This radiation is called Cherenkov radiation. The radiation is explained by a polarization of molecules of the medium.

When a charged particle runs across a medium, the temporal electric dipoles in the medium are induced. When the velocity of the charged particle is less than light velocity in the medium c/n, the arrangement of these dipoles are symmetrically around the position of the charged particle as shown in Fig.3.4. This is because the electric field around the charge particle propagates in the medium faster than the particle motion. Because of the symmetric arrangement, there is no net polarization of the medium in larger scale and no radiation is emitted. On the other hand, when the particle has a velocity larger than the speed of light in the medium, no temporal dipoles arises in the region ahead of the particle motion as shown in Fig.3.4. Since the electric field cannot propagate faster than the particle motion, the net polarization is produced along the path of the particle and consequently emits photons when temporal dipoles recover. These radiations are coherent and form a shock-like wave front as shown in Fig.3.4. From this geometry of this emission,

the Cherenkov radiation is only observed in a particular angle,

$$\cos\theta = \frac{1}{n\beta}, \tag{3.1}$$

where $\beta = vc$. This angle is called Cherenkov angle.

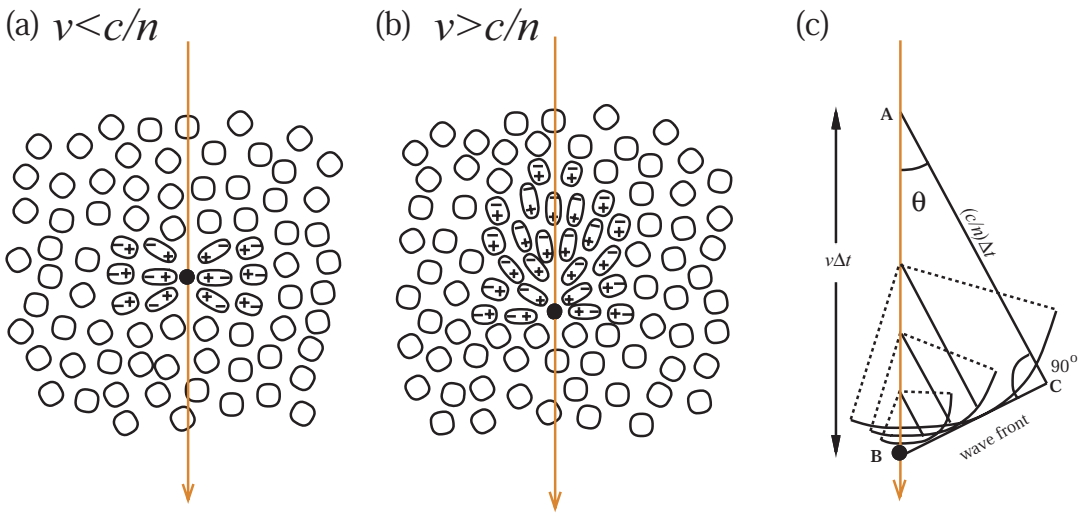

Figure 3.4 Polarization set up in a dielectric when a charged particle passes through. **a:** Low velocity. **b:** High velocity. **c:** Huygens construction to illustrate coherence and to obtain the Cherenkov angle θ.

The threshold of the emission of Cherenkov light depends on the refractive index of the atmosphere. At the wavelength of 400 nm for example, the refractive index of the atmosphere at the temperature of T [K] is given by

$$n = 1.0 + 0.000296 \left(\frac{x}{1030\mathrm{gcm}^{-2}}\right)\left(\frac{T}{273.2\ \mathrm{K}}\right)^{-1}. \tag{3.2}$$

where x is the atmospheric depth in g cm^{-2}, and T is the atmospheric temperature expressed as $T = 204 + 0.091x$ [K] (Hillas, 1985). The atmospheric refraction index at the sea level is $n \sim 1.000283$, and the corresponding Cherenkov angle (θ) is obtained to be 1°.36 for the relativistic ($\beta = v/c \sim 1$, v is the velocity) particle. From the condition of $\cos\theta \leq 1$, the minimum energy of the particle emitting the Cherenkov radiation in the medium E_{min} is written as,

$$E_{min} = \frac{mc^2}{\sqrt{1-\beta_{min}^2}} = \frac{mc^2}{\sqrt{1-n^{-2}}}, \tag{3.3}$$

For the refractive index of $n = 1.000283$, the minimum energy is obtained to be 21.5 MeV and 39.4 GeV for an electron and a proton, respectively. This energy depends on the altitude, because of the dependency of n which is shown in Fig.3.5.

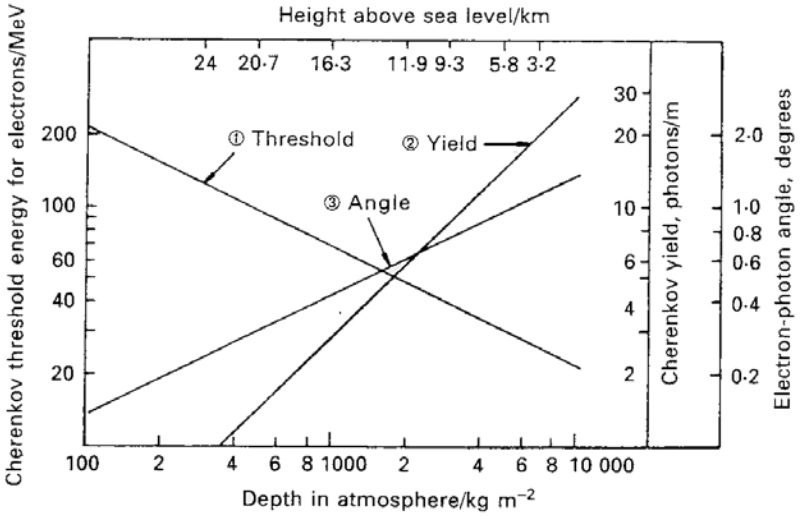

Figure 3.5 The variation with the depth in the atmosphere of different property of the Cherenkov radiation related to electrons (Logair, 1992).

The energy loss by the Cherenkov radiation per unit path length is expressed as

$$\frac{dE}{dl} = \frac{z^2e^2}{c^2}\int_{\beta n>1}\left(1-\frac{1}{\beta^2n^2}\right)\nu d\nu, \tag{3.4}$$

where ze is the particle charge and ν is the frequency of Cherenkov radiation (Jelly, 1958). Thus, the number of the Cherenkov photons emitted while the particle moving a unit length dl in the medium is given as

$$\frac{dN}{dld\lambda} = 2\pi\alpha z^2\frac{1}{\lambda^2}\left(1-\frac{1}{\beta^2n^2}\right), \tag{3.5}$$

where λ is the wavelength of Cherenkov radiation $\lambda = 1/c\nu$.

3.2.1 Cherenkov Light Observation

I describe the observation of the Cherenkov light from an EAS on the ground here. As calculated in the previous section, with refraction index at high altitude $n(10\text{ km}) \sim 1.0001$, Cherenkov photons are emitted within the Cherenkov angle of $\theta_c \sim 0.014$ rad.

Then, at the sea level, Cherenkov photons spread over ∼140 m radial pool. At the lower altitude, n gets larger and it makes θ_c larger. A radial profile of the Cherenkov photons are shown in Fig.3.6. A result of a Monte-Carlo simulation of an electromagnetic shower triggered by a 1 TeV gamma-ray is shown in Fig.3.7 (top). The radial profile has a flat photon density within 150 m radius and extends over 250 m. A result from an EAS triggered by 3 TeV proton is shown in Fig.3.7 (bottom) for a comparison. The distribution of the Cherenkov photons is not symmetric and varies event by event in the proton triggered EAS. Figure 3.8 shows the energy dependence of the Cherenkov photon density from gamma-rays of different energies. While the size of the light pool is independent of the initial energy, the photon density depends on the initial energy. Thus, we can estimate the initial energy from an only fraction of Cherenkov photons. By defining the effective area of the VHE gamma-ray detection as a circle of a 150 m radius, it is obtained to be $\sim 10^5$ m^2 which is much larger than that of satellites or balloons.

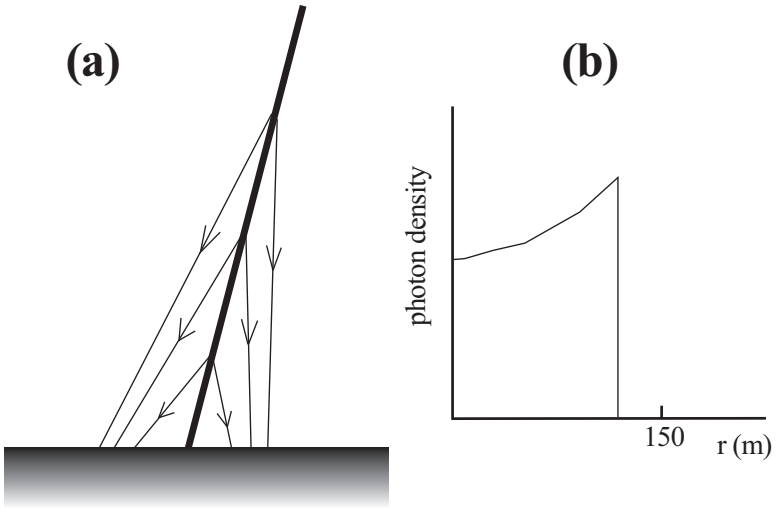

Figure 3.6 A sketch of Cherenkov light on the ground. (a) Cherenkov light emission at different atmospheric heights, changing θ_c due to the variation of the refraction index of atmosphere. (b) The photon density distribution at the ground level ignoring multiple Coulomb scattering of electrons.

The major backgrounds in the ground-based gamma-ray observation are the cosmic-ray protons. For example, the Crab nebula, which is known as a brightest steady TeV gamma-ray source, emits TeV gamma-rays with the integral flux of $\sim 10^{-11}$ cm^{-11} s^{-1} above 1 TeV. At the same time, the background cosmic-ray proton flux is known as $\sim 10^{-5}$ cm^{-2} s^{-1} str^{-1}. Assuming the field of view (FoV) of a Cherenkov telescope with a

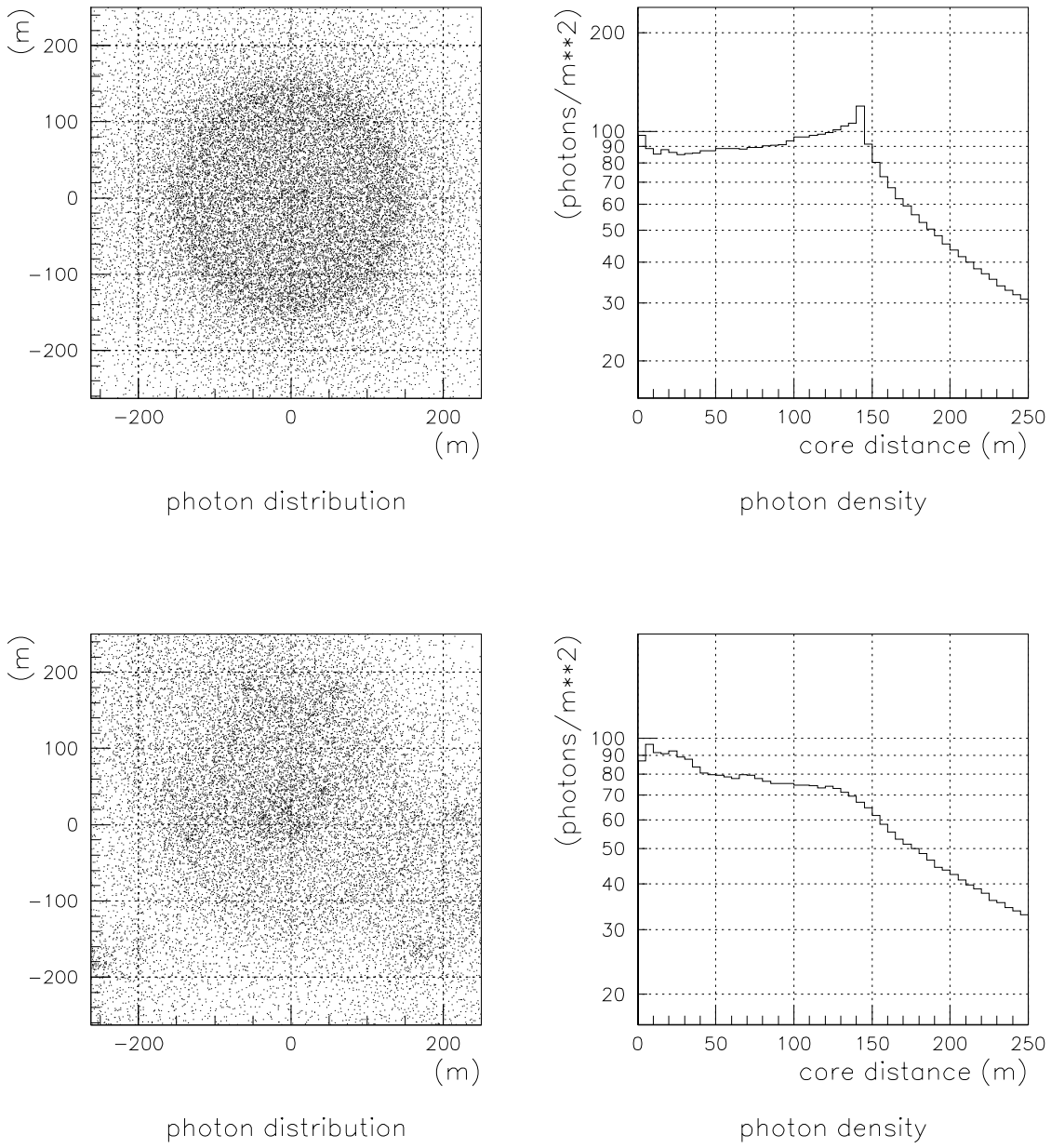

Figure 3.7 Distribution of the Cherenkov light on the ground. **Top:** An EAS by a 1 TeV gamma-ray. Symmetric and uniform density spreads until 150 m radius. **Bottom:** An EAS by a 3 TeV proton. More complicated structure can be seen compared with the top panels.

few degrees $\sim 10^{-3}$ str, a gamma/hadron ratio is estimated to be $\sim 10^{-3}$. Thus, we must reject the background proton effectively. For the background rejection, the method called imaging technique which is established by the Whipple group is widely used. Cherenkov lights from an EAS are collected by a reflector and recorded by a imaging camera at the focal plane as shown in Fig.3.9. The image on the camera tells us how the EAS has developed both in longitudinal and lateral directions. Since the developments of gamma-ray induced EAS and cosmic-ray induced EAS are different as described above, their images on the camera are also different. The simulated shower images of a 1 TeV gamma-ray and 3 TeV proton are shown in Fig.3.10, in which the image of a gamma-ray EAS is more compact and pointing the source direction in the FoV. On the other hand, the image of a cosmic-ray EAS has no information of the direction in the FoV. To select a gamma-ray from a cosmic-ray event, Hillas (1985) approximated the images with an ellipse and parameterized the image shape. These parameters are called "Hillas parameters", and are written in terms of moments of the light intensity distribution. Figure 3.11 represents the Hillas parameters (WIDTH, LENGTH, and DISTANCE) on a shower image. WIDTH and LENGTH are standard deviations of the distribution of the light intensity along the major and minor axes, respectively. DISTANCE is an angular separation between the source position and the center of gravity of the image. Numerical definitions of these parameters are described in App. A. Although there are other parameters used in Hillas (1985), we used only these three parameters in our analysis.

The array of IACTs provides better angular and energy resolutions than those of a single IACT. The array of IACTs receives the Cherenkov lights from an identical EAS simultaneously, which is called a stereoscopic observation. While the single image of the shower cannot determine the arrival direction of the shower, a stereoscopic observation can determine the arrival direction event by event since the multiple images of the single shower from different directions enables us to reconstruct of 3D image of the shower. Intersection point of the image major axes tells the arrival direction event by event as shown in Fig.3.12. At the same time, the intersection points on the ground coordinate represents an impact position of the shower which is defined as the intersection between the ground and an extrapolation of the path of the primary particle as shown in Fig.3.13. A larger distance between the telescopes gives better angular resolution as shown in Fig.3.14. However, the distance is limited by the size of the Cherenkov light pool, and the larger distance makes the detection efficiency smaller. The relationship between the angular resolution and the number of telescope is shown in Fig.3.15. Since the present

IACTs have a large mirror size over 10 m, the Cherenkov light from the cosmic-ray muons are also detected. Cherenkov light from the muon event directly arrive at the telescope as shown in Fig.3.16. It is detected as a ring or an arc image on the camera. Only Cherenkov photons radiated below $2r/\tan\theta_c$ are received by the reflector, where $2r$ is a diameter of the mirror. This means that the maximum height of detectable Cherenkov light is $\sim$1000 m, which is independent of the energy of the muon. Thus, the Cherenkov photons from the muon distribute in 20–30 m circle on the ground. When the distance between telescopes are set to 100 m, the Cherenkov photons from the muon do not hit multiple telescopes simultaneously. Thus, the background-muon event can be rejected in stereoscopic observation from this feature.

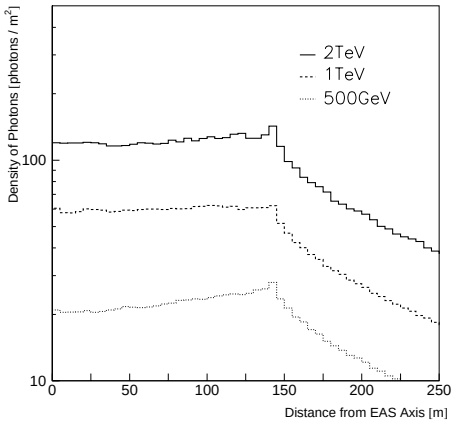

Figure 3.8 Energy dependence of the Cherenkov light density on the ground.

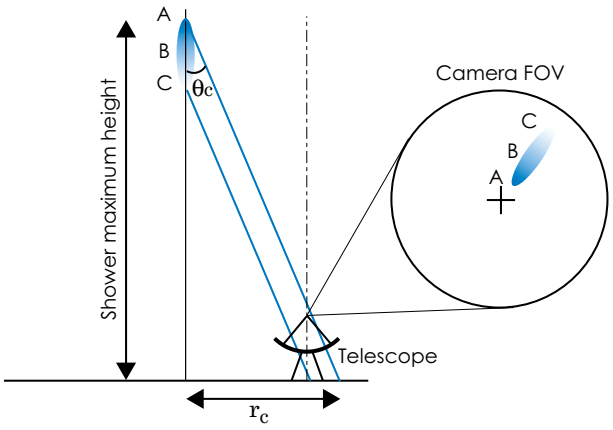

Figure 3.9 A Schematic of geometry of a shower and a Cherenkov telescope.

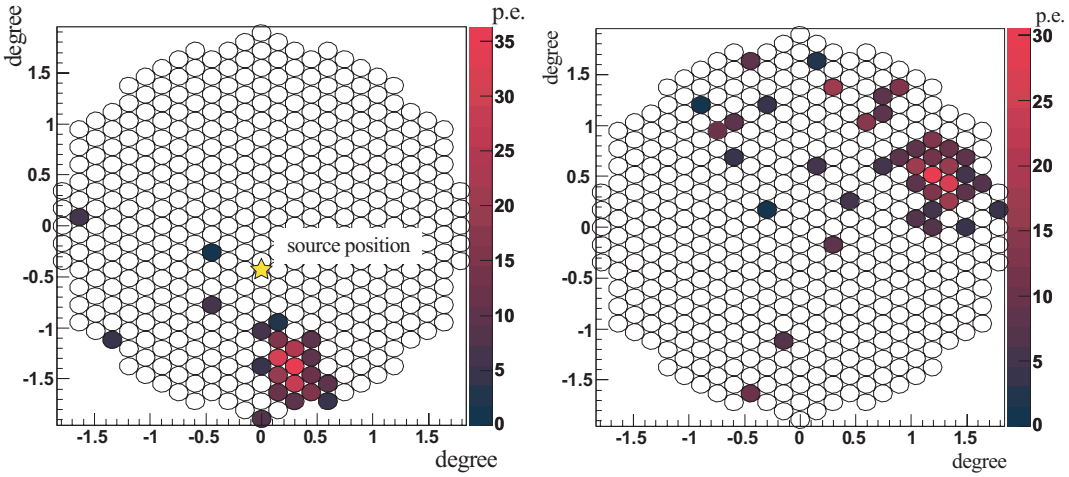

Figure 3.10 Shower images on the camera of CANGAROO-III. **Left:** a shower initiated by 1 TeV gamma-ray, **Right:** by 3 TeV proton. Grey circles indicate pixel of the camera.

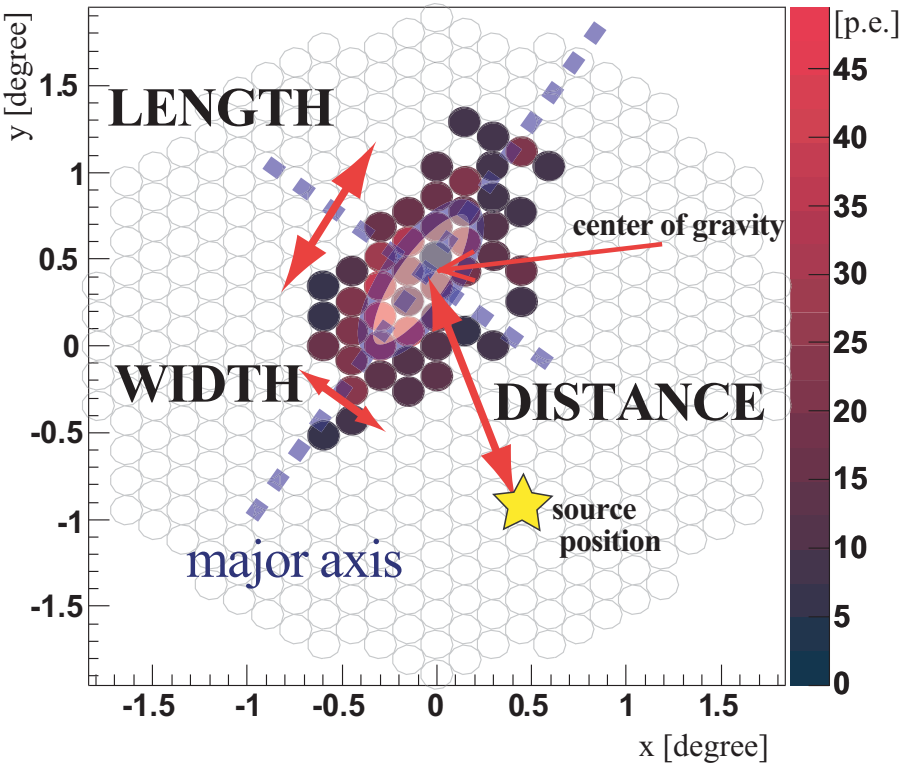

Figure 3.11 Definition of the image parameters. The small circles indicate the PMTs and the color bar represents the value of ADC count in each pixel.

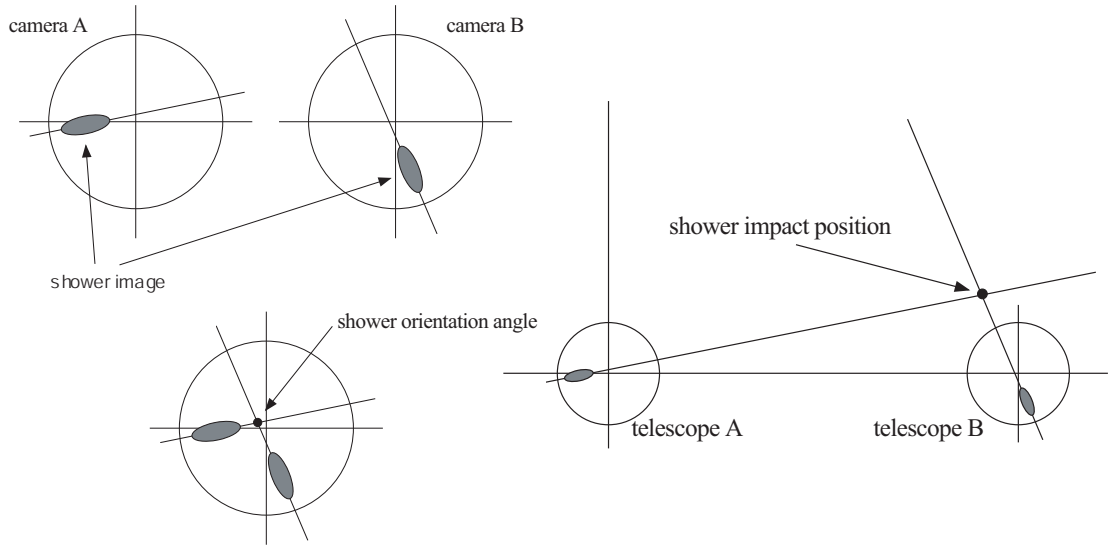

Figure 3.12 Determination of shower orientation angle (left) and impact position on the ground (right) by two telescopes.

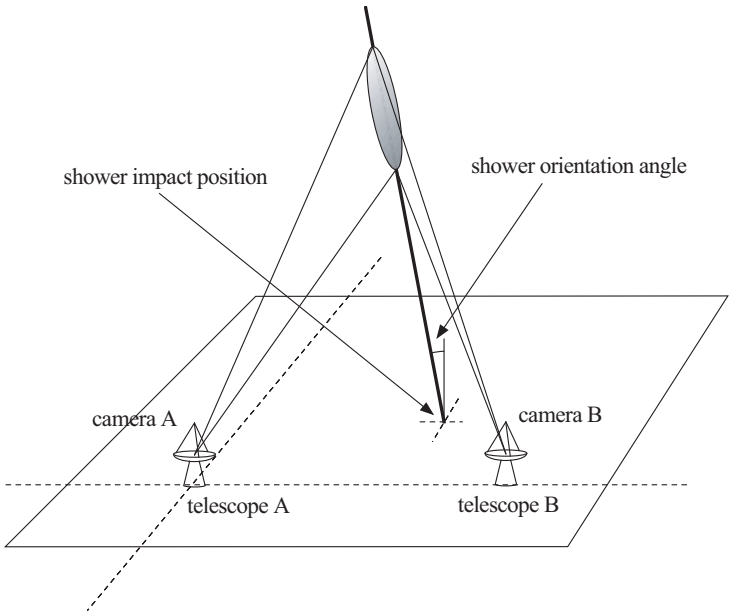

Figure 3.13 Schematic of stereoscopic observation and the three-dimensional reconstruction of a shower.

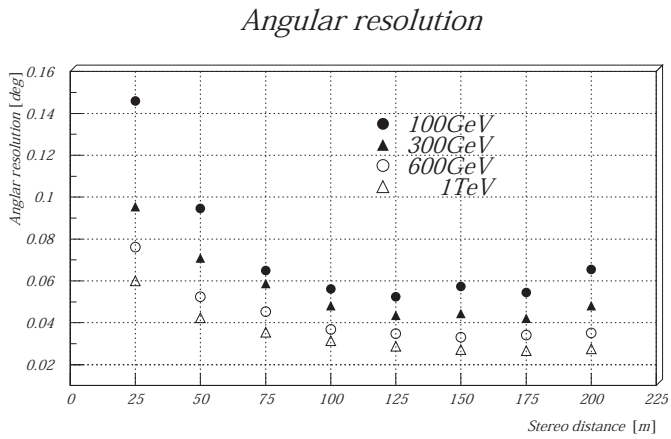

Figure 3.14 Angular resolution and the pitch of telescopes(Hara, 1999).

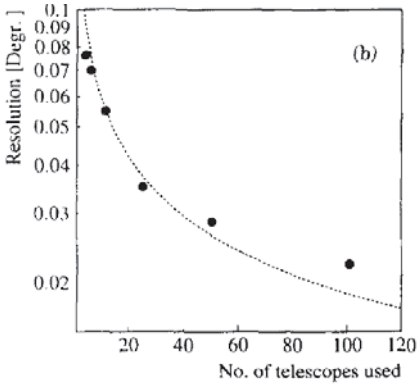

Figure 3.15 Angular resolution and the number of telescopes(Hofmann et al., 1999).

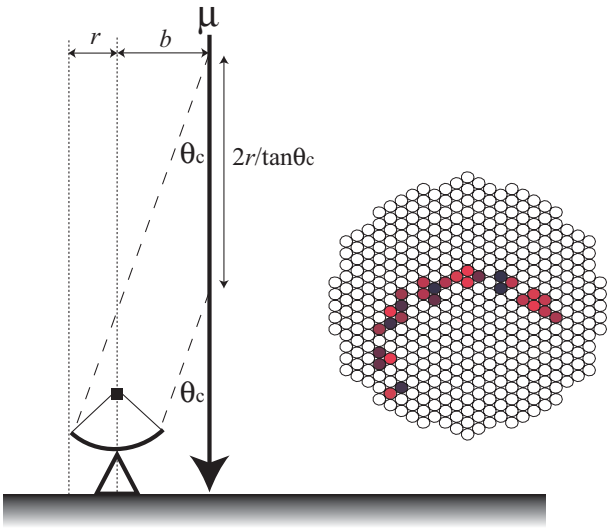

Figure 3.16 Schematic of muon triggered event and observed event by CANGAROO-III(Adachi, 2005).

Chapter 4

CANGAROO-III telescope and Observation

4.1 CANGAROO experiment

CANGAROO is an acronym of Collaboration of Australia and Nippon for a GAmma-Ray Observatory in the Outback. The observation site is located near Woomera, Australia at 136°48′ E, 31°06′S and 160 m above sea level, where Galactic objects can be observed with small zenith angles. From 2002 three ϕ10 m telescopes, CANGAROO-III telescopes, were constructed with several instrumental improvements from previous telescope (CANGAROO-II, T1). The geometrical distribution of the telescope array is shown in Fig.4.2. These three telescopes, hereafter T2, T3, and T4, have an identical hardware configuration. I describe the specifications of T2, T3, and T4 in this section.

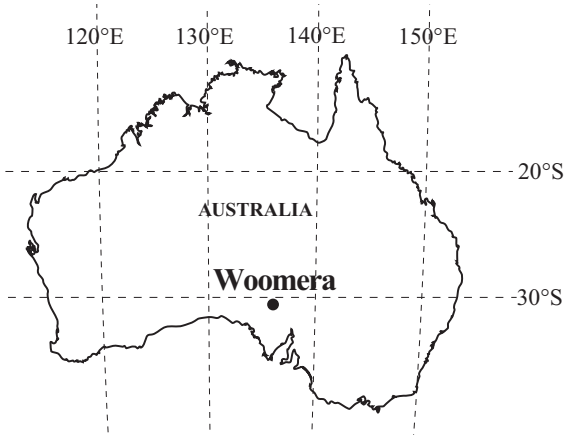

Figure 4.1 Position of the observation site of the CANGAROO-III, Woomera.

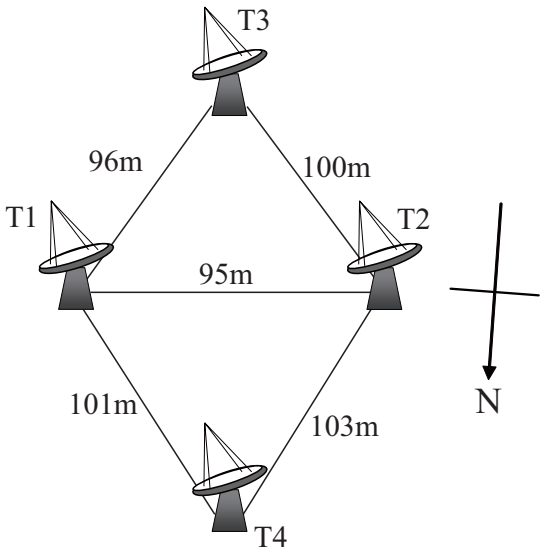

Figure 4.2 Geometrical distribution of CANGAROO-III telescope array.

4.1.1 Reflector

The CANGAROO-III telescope has 114 segmented reflectors with a radius of 39 cm on its parabolic flame. The total reflection area is ~ 57 m^2. The mirror mount and adjustment system are shown in Fig.4.3. The parabolic arrangement has a merit in the conservation of photon arrival timing comparing to Davies-Cotton layout (Davis & Cotton, 1957), The maximum fluctuation in the photon arrival timing from different portions of our paraboloid design with a diameter of 10 m was less than 0.2 nsec (Kawachi et al., 2001) while Davies-Cotton 10 m reflector ($f/0.7$) is 6 nsec (Lewis, 1990).

Each mirror is manufactured as a spherical mirror made of glass fiber reinforced plastic (GFRP). An FRP segment was suitable for our telescope which placed outside in the desert, since an FRP segment was quite light and durable, although had almost the same strength as conventional glass one with 80 % reduced weight. FRP mirrors are formed by molding, pressured in an auto-clave. The cross section and appearance of the mirror are shown in Fig.4.4 and 4.5. Surface of the mirror was coated by aluminized polymer sheet, which has nearly 90 % reflectivity at a wavelength of $\sim$300 nm. The reflectivity was measured immediately after manufactured (Yuasa, 2006). The result of the measurement is shown in Fig.4.6. Curvature radii of produced segments were distributed within 16.6 ± 0.6 m. The mount base of the mirrors on the reflector frame has two degree of freedom, position to be set and a rotation angle. These parameters were

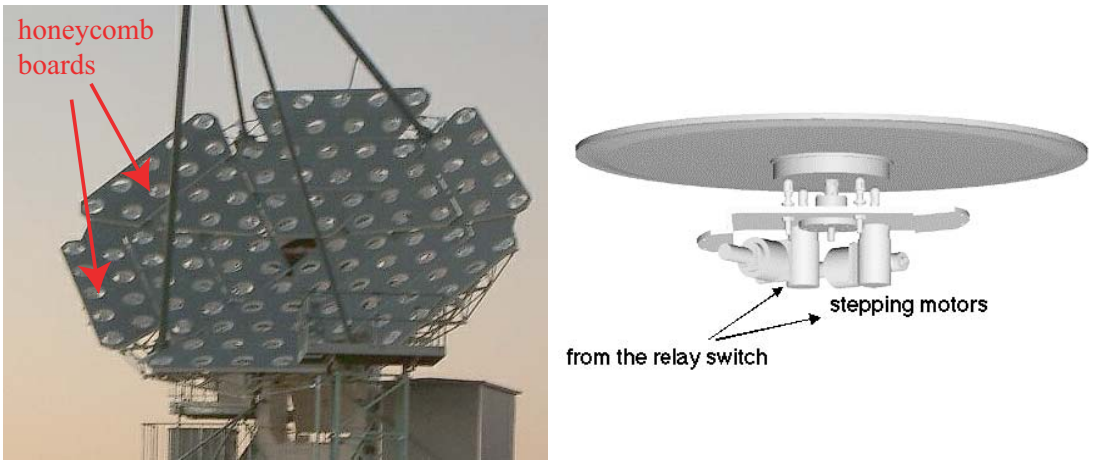

Figure 4.3 **Left:** Honeycomb boards on the reflector frame. **Right:** Schematic of adjustment system.

determined, in order to obtain the best total image quality, using a Genetic Algorithm (GA) based program (Ohishi, 2002, 2005).

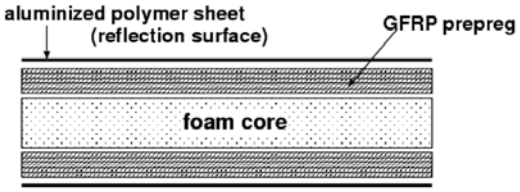

Figure 4.4 A cross section drawing of a FRP segment.

Figure 4.5 GFRP mirror segment with 80 cm diameter and 5 kg weight.

A total spot size of the whole reflector was measured using bright stars. No significant deterioration of the image due to the gravitational deformation was found (Ohishi, 2002; Kawachi et al., 2001). Fig. 4.7 shows an image of a bright star taken by a CCD camera. The spot sizes which are obtained from the fitting of the image by Lorentzian are summarized in Table 4.1. These values are used in Monte-Carlo simulation of the telescopes.

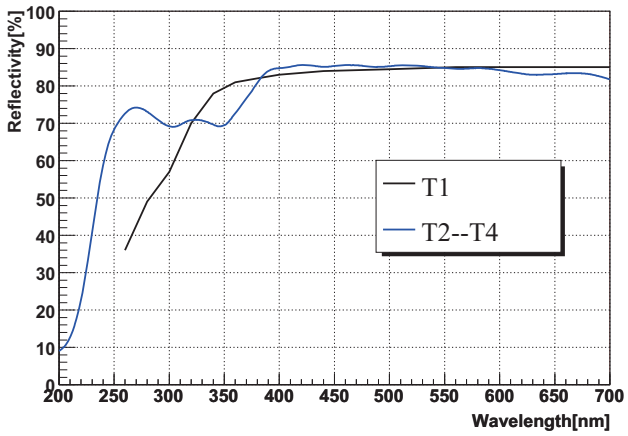

Figure 4.6 Reflectivity of FRP mirrors just after manufactured. Blue line shows that of T2–4 (Yuasa, 2006).

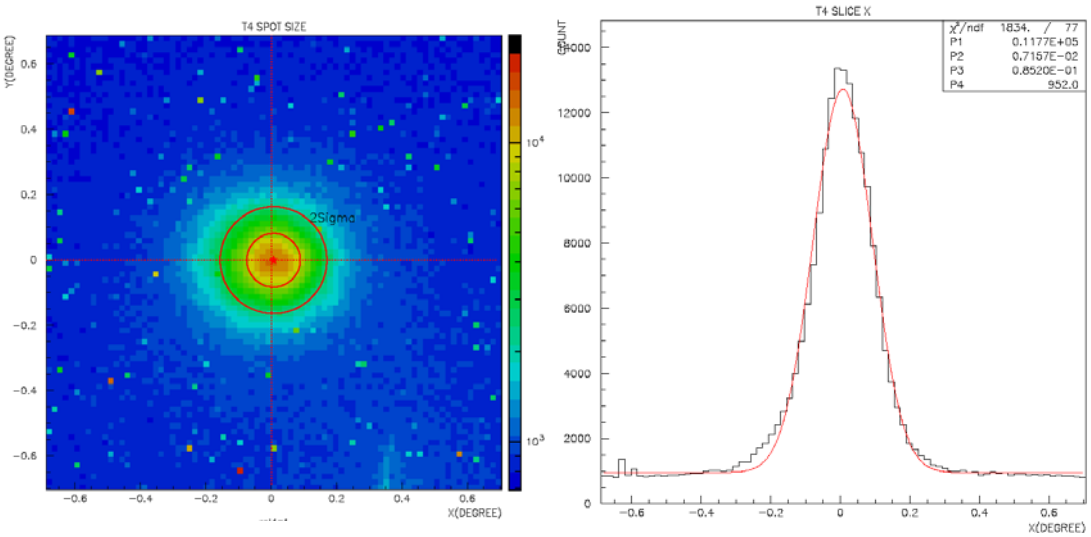

Figure 4.7 A total optical spot-size measurement(Kiuchi, 2004). **Left:** A CCD image of a reflected bright star. **Right:** A projection of the image to X-axis. The solid curve represents a result of a fitting by Lorentzian function. (Taken from Ohishi (2002).)

Table 4.1 Optical spot size of the telescopes used in 2008 observation.

Telescope No.	Optical spot size (FWHM)
T3	0°.10
T4	0°.10

4.1.2 Imaging Camera

Photo-multiplier tubes (PMT) were used to convert the Cherenkov photons which have a very narrow pulse width $\leq$ 10 ns and a spectrum peaked at the short wavelength (blue/UV) to electric signal. The CANGAROO-III camera consists of 427 PMTs with a diameter of 3/4 inch. All the PMTs were arranged in a hexagonal close packing with a light-collecting cone front of the photo cathode as shown in Fig.4.8. The field of view is 4°.0 (full angle), and the pixel size in angle is 0°.168. A camera apparatus, of which weight is $\sim$ 120 kg, is fixed inside the camera-support cylinder, which is attached to a ring at the focal plane supported by four steel stays. The 28 m signal cables from the camera were connected to the electronics hut at each telescope. A 3/4 inch PMT, HAMAMATSU R3479 (Fig.4.8 right), was selected. To enhance the sensitivity of shorter wavelength, UV glass window was adopted. The measured quantum efficiency of R3479 photo cathode is shown in Fig.4.10. The PMT signal is amplified by a high-speed preamplifier (Maxim MAX4107) before the 28 m-long transmission. The gains of all PMTs were calibrated in the laboratory using one-photon signal emitted from a fast blue LED before the installation. The gain fluctuation in whole the camera was less than 1% in the laboratory. A linearity between input and output photoelectrons was maintained up to 200 photoelectrons as shown in right panel of Fig.4.10. Time resolution of the PMT was measured as 0.94 ns (1σ) at 30 photoelectrons (Kabuki et al., 2003). The PMT gain distribution and timing characteristics are measured and corrected by adjusting a high voltage through software in every observation. High voltages (HVs) are supplied on each PMT using a HV supplier module, CAEN SY527 and A392. This module can set a different voltage to the individual PMT. The voltage for each PMT is controlled via a CAENET VME-bus controller, CAEN V288, with a GUI-based software. This software calculates positions of stars in the FoV every second and has an optional function which turns off HVs around bright stars. We used a threshold magnitude of 4.0 mag and radius of 0°.2 FoV turning off HVs.

4.1.3 Electronics and Data Acquisition System

The signals from the camera are fed to the electronics hut in each telescope through twist pair cables of which length is 28 m. The signals are at first fed to DSM (Discriminator Scalar Module) in the electronics hut. DSM can deal 16 channels per board and generates four signal outputs, two analog outputs for ADC and TDC, and two signals for trigger

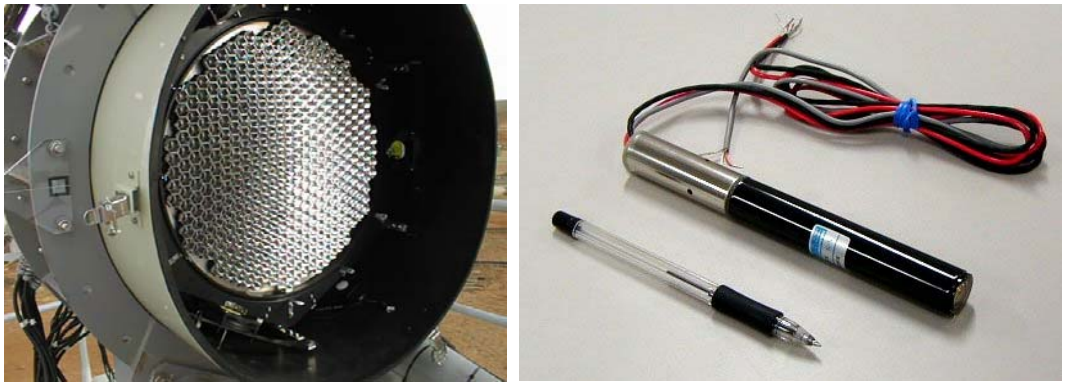

Figure 4.8 **Left:** A front view of the CANGAROO-III camera. **Right:**HAMAMATSU R3479, used as camera pixels of CANGAROO-III.

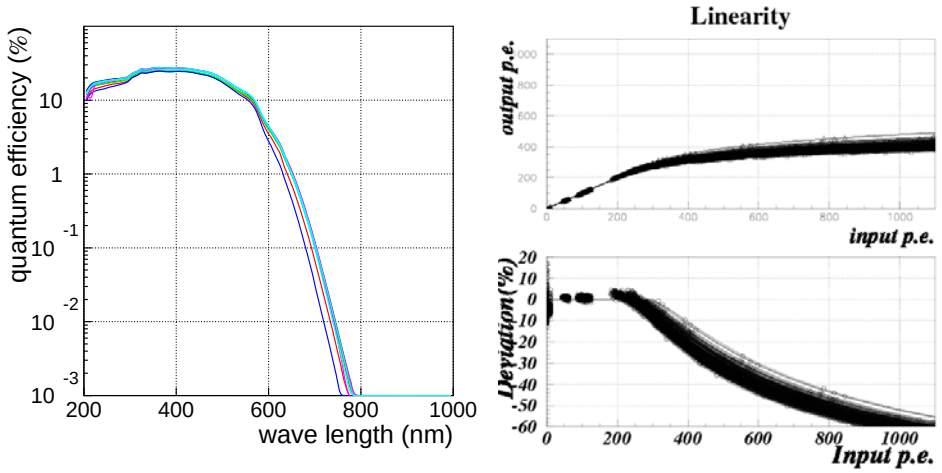

Figure 4.9 **Left:** Measurements of quantum efficiency as a function of wavelength. Results for 10 individual PMTs are overlaid(Kabuki, 2004). **Right:** Linearity of R3479 with the preamplifier(Kabuki, 2004).

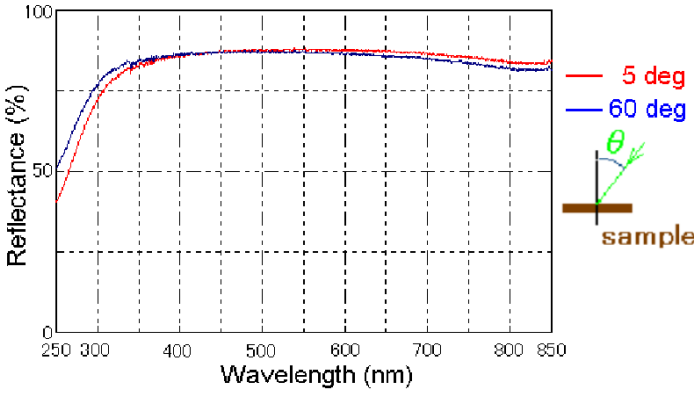

Figure 4.10 Measured reflectance of the light guide(Kabuki, 2004).

decision. The block-diagram and grouping of the DSM are shown in Fig.4.11 and 4.12 The inputted signal is amplified by two-stage ope-amp (CLC400) and splatted to the four signals. First signal is fed to charge integrated ADC. The ADC has 32 signal inputs and the inputted signal are delayed 150 ns by a delay chip on the board. When a trigger signal is inputted, the charge is integrated and recorded. A second signal is summed signal for 16 channel of DSM board. This signal is fed to the trigger decision circuit as ASUM (Analog SUM) signal. Third and fourth signals are fed to updating discriminator and non-updating discriminator, respectively. The threshold level of these discriminators can be changed by remote control through VME. The signal from the updating discriminator is fed to multi-hit TDC. This TDC has 64 channel inputs with the time resolution of 0.78 ns. The TDC records both a leading edge and trailing edge of the signal. The signal from the non-updating discriminator is splatted to two signals. One is fed to 12 bit scaler to record the effect of NSB or star light on PMT. One is summed for 16 channels of DSM board and fed to trigger decision circuit as LSUM (Logic SUM) signal.

I describe the trigger decision here. The Cherenkov light from the EAS hits multiple PMTs of the camera. For a lower energy primary particle, the EAS is smaller and number of hit PMTs is also smaller. From our Monte-Carlo simulations for the CANGAROO-III telescope, about 10 PMTs will be hit for 100 GeV gamma-ray shower and light amount of PMT at the image center are 8-10 photoelectrons/PMT. On the other hand, NSB photons hit PMT at random with a light amount around 5 photoelectrons/PMT, estimated from

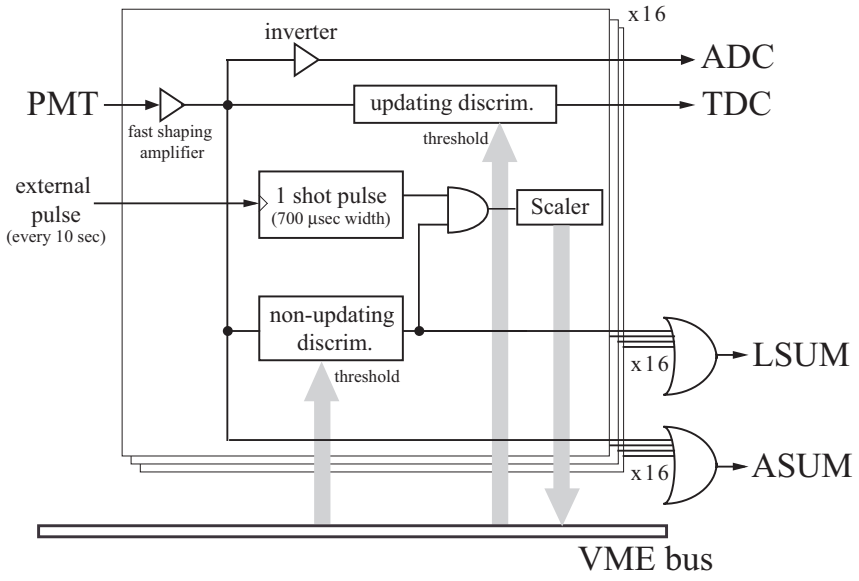

Figure 4.11 A block diagram of the DSM.

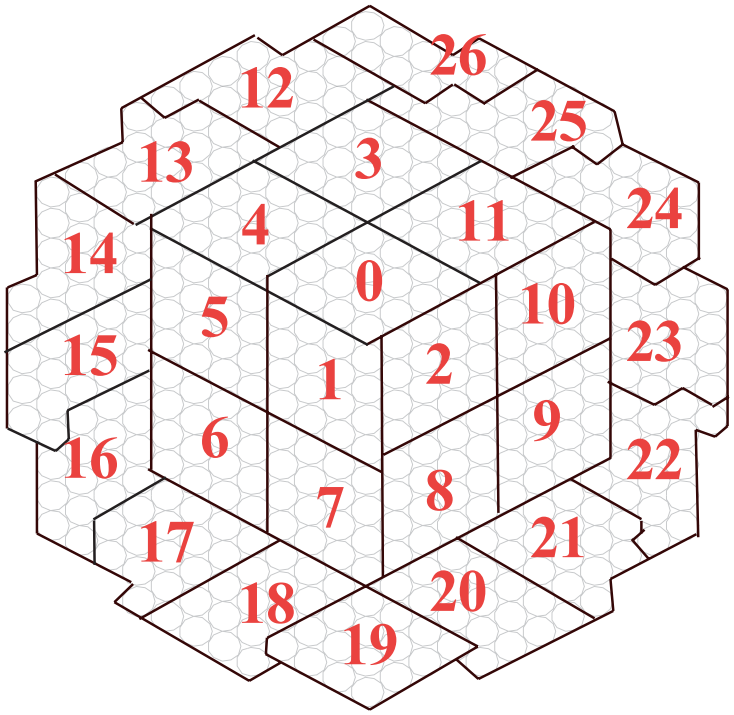

Figure 4.12 A grouping of camera pixels. Numbers represents corresponding IDs of the DSM.

Jelly's equation (Jelly, 1958). By using these differences, we can remove an effect of NSB setting a hardware threshold in the trigger decision. In CANGAROO-III telescope system, we use ASUM and LSUM signals in the trigger decision. Schematics of the trigger decision is shown in Fig.4.13. One telescope has 27 DSM boards. All the LSUM output of the DSM boards are summed and fed to the discriminator (CAEN v895) operated in non-updating mode. One LSUM signal has information of the number of PMTs which exceed the threshold level in one DSM board. Thus, the threshold level of this discriminator corresponds to the number of the PMTs for one telescope. This threshold level is called NHIT. We typically use the threshold to generate LSUM signal as 5-6 photoelectrons and NHIT as 4 hit PMTs. A threshold level for ASUM is set for each DSM unit, of which has information of light amount for each DSM board. We put a threshold level for a sum of all ASUM signals in a telescope which is called NBOX. When a signal is passed all these threshold levels, a gate signal for ADC, a stop signal for TDC, a time recording trigger signal for GPS, and a trigger signal for a stereo trigger system are generated. When the telescope is in "Local trigger mode", the interrupt signal is immediately generated and the recorded information is readout. When the telescope is in "Global trigger mode", the interrupt signal is generated only after a signal from the stereo trigger system is returned.

Here I describe the stereo trigger system. The purpose of the stereo trigger system is lowering the hardware threshold level without increasing the deadtime of DAQ system. As lowering the threshold level, the number of hit PMTs by the NSB or single muon event drastically increases. Then, when using only the local trigger mode, the deadtime will rapidly increases. In the stereo trigger system, we reject these noise events using the difference of the Cherenkov light extent from EAS and muon event. In the stereo trigger system, only when the event trigger signals from several telescopes are coincided, the system returns the event signal to each telescope. Figure 4.14 shows schematic view of the stereo trigger system. When the local trigger condition is fulfilled in each telescope, the signal is fed to the stereo trigger system by the optical cables. The coincidence decision is made within 650 nsec, considering a difference of light path from the EAS to each telescope. When two or three telescopes are coincided, the trigger signals for the interrupt are returned to each telescope with the event number. This number of the telescope in coincidence decision can be changed readily. When the local trigger is generated, the local trigger system is stopped by VETO signal. When the stereo trigger is not generated within 5 μs after the local trigger generation, the DAQ system is cleared without data readout. Figure 4.15 shows the timing chart of the trigger system.

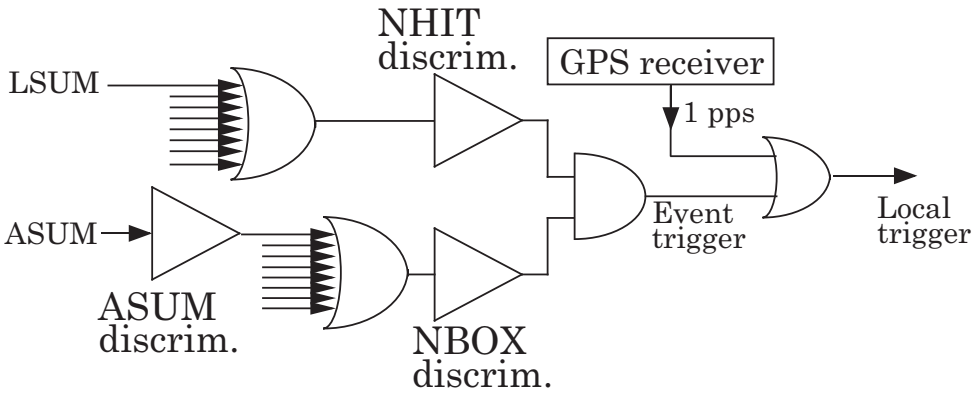

Figure 4.13 Logic of local trigger. Either coincidence of NHIT and NBOX discrimination or GPS pulse generates the local trigger of individual telescopes.

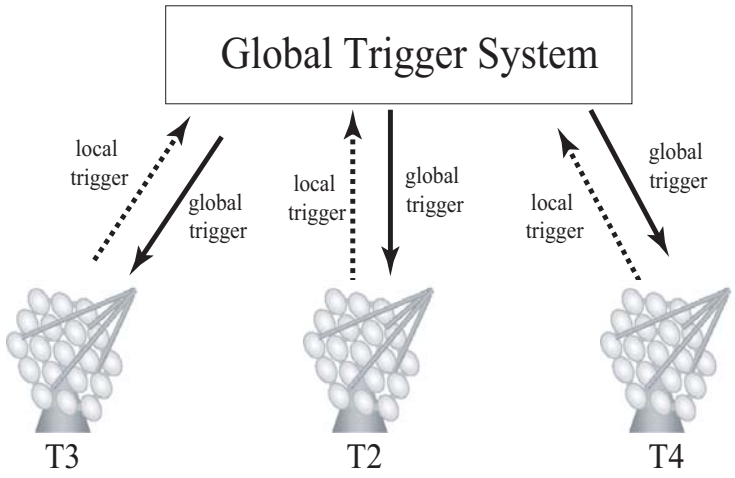

Figure 4.14 Concept of Global Trigger System(GTS).

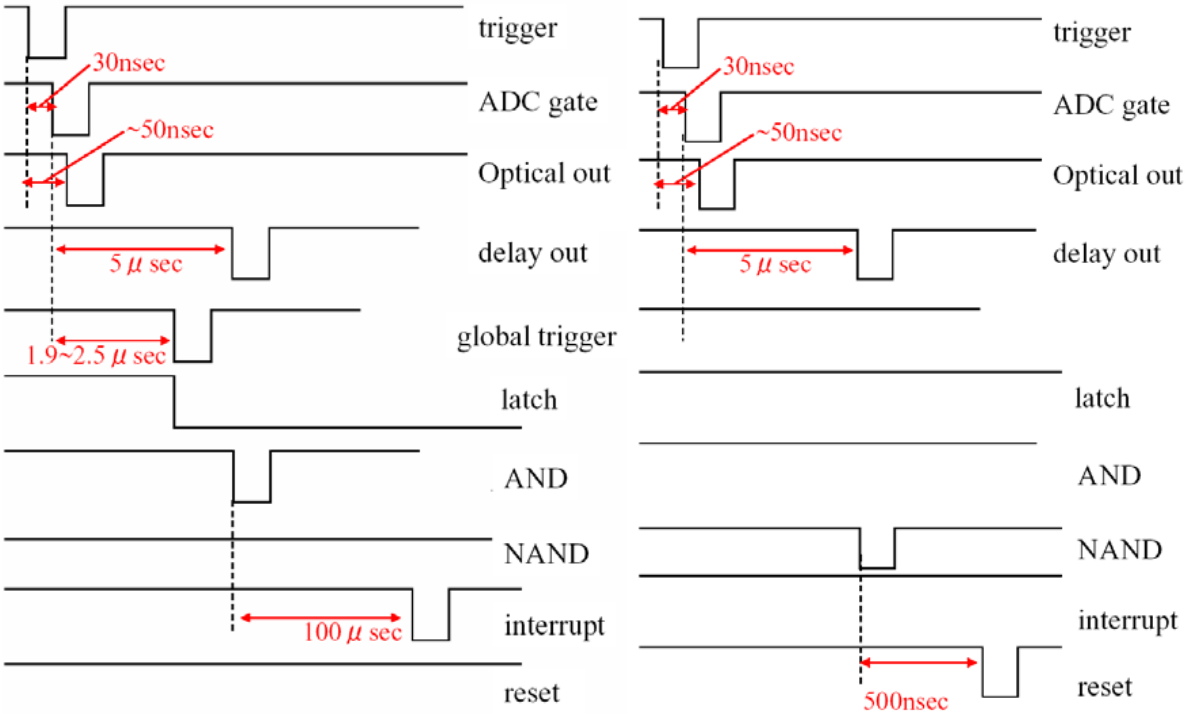

Figure 4.15 Timing chart of the trigger system.**Left:** The stereo coincidence is approved. **Right:** The stereo coincidence is not approved.

4.2 Telescope performance

4.2.1 Muon analysis

Determination of light collecting efficiency for each telescope is very important to simulate the gamma-ray events. The light collecting efficiency is defined as,

(Light collecting efficiency) = (Reflectance of the mirror) × (Reflectance of the light guide) × (Transmittance of the photoelectric surface of PMT).

Since amount of Cherenkov photons from a single muon is almost constant, those muon events are used as a probe of the light collecting efficiency. *Size/Arclength* of the muon ring is a good parameter, where *Size* is the total photoelectrons of the muon event and *Arclength* is the arclength of muon ring in the FoV. We have carried out the muon observation more than 8 hr each month. Since the Cherenkov photons from the muon event are radiated at a height of $\sim$ 200 m, this observation run was able to conduct in even the cloudy night. Because the muon event gives a ring like shape on camera as shown in Fig.3.16, it was selected by its shape. Figure 4.16 shows the time variation of the *Size/Arclength*. The vertical scale is normalized to the initial *Size/Arclength* value to be unity. Because of dusts and deterioration on the mirror, the light collecting efficiency of each telescope has gradually decreased. During 2005, the light collecting efficiency of T2 was hardly determined, since no muon events were remained after the muon selection analysis. Then we carried out mirror cleaning 2005, and then the light collecting efficiency of T2 had been recovered once. However, the efficiency has not been determined again since 2008 summer. Thus, I did not use T2 data for following analysis in this thesis, and only T3 and T4 data were used.

4.3 Observation of HESS J1614-518

4.3.1 Observation Mode

It is important for IACTs to estimate the background events still remained after applying the image cleaning. A conventional method to estimate the hadron events in the final data is ON−OFF subtraction. We have needed a long ON/OFF run for a long time since this experiment started in 1992. In this method, the OFF run was carried out by tracking a same pass in the sky as the ON run in the same night. Thus, OFF run has a same elevation/azimuth distribution as that of the ON run. While this mode sometimes

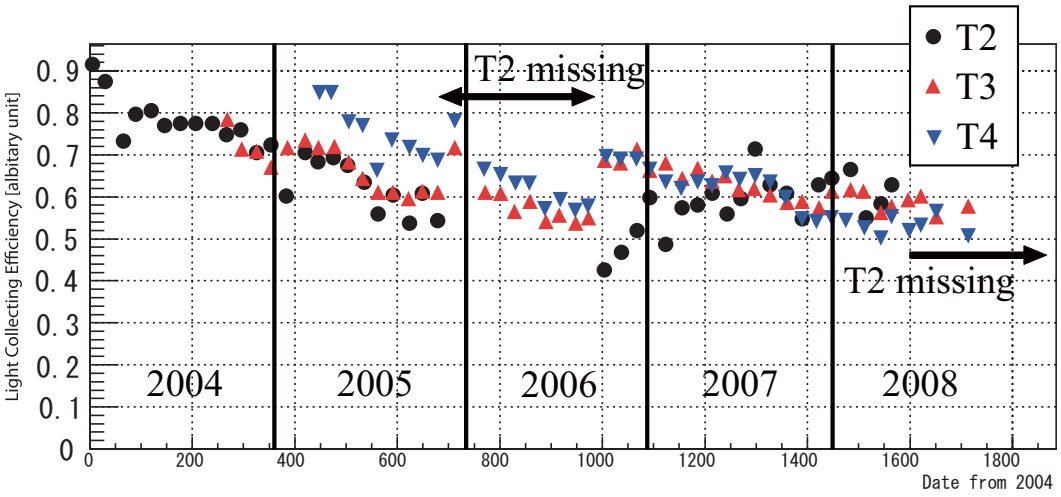

Figure 4.16 Time variation of the light collecting efficiency obtained by the muon observation.

reduces the ON run time to take a OFF run in the same night, a Wobble mode which was developed for the stereo observation by HEGRA group succeeded in taking the OFF data simultaneously during the ON run. In this observation mode, the pointing position of the telescope has an offset of ± 0.5 degree by declination from the target position in order to reduce the effect of inhomogeneous acceptance in the FoV. The offset is switched periodically (20 minutes for CANGAROO-III, 14 min for H.E.S.S., for example), which is the reason of this naming "Wobble". The OFF data are taken from the events which have an intersection point in the OFF region in the FoV. The OFF region are determined as a ring region background and wobble opposite position as shown in Fig.4.17. The ring region has an advantage in statistic of background event due to its large region size, which is now widely used in the IACTs. A wobble opposite position is taken to estimate a systematic error in Chapter 5.

4.3.2 Observation of HESS J1614-518

The observation of HESS J1614-518 were carried out from May to August in 2008 using the Wobble mode. The stereo trigger mode was used as a trigger mode. The pointing position were offset by ± 0.5 degree from the center position of HESS J1614-518 reported by H.E.S.S. group in declination or right ascension, and changed every twenty minutes, in order to suppress position-dependent effects on the camera due to stars. The observation

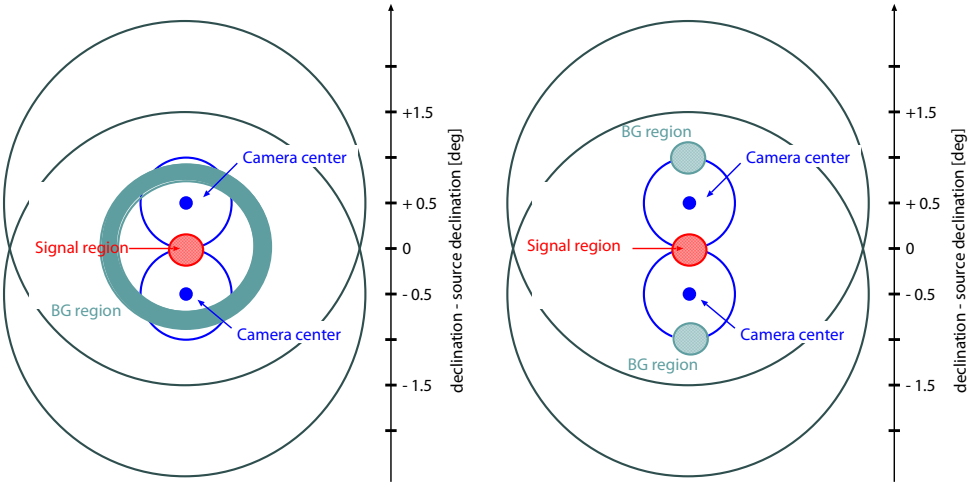

Figure 4.17 Wobble position and BG region. (*Left:*) Ring background. (*Right:*) Opposite background.

Table 4.2 Observation time and Livetime of HESS J1614−514 observations.

	ON run	
Month	Obs. time [min]	Livetime [min]
2008 May	987	862
2008 June	1535	1297
2008 July	1010	868
2008 August	238	189
Total	3770	3217

time and livetime are shown in Table 4.2. The zenith and azimuth distributions are shown in Fig.4.18.

4.4 Monte-Carlo Simulation

For the IACTs, it is difficult to obtain the pure gamma-ray event data, since there is no artificial source providing TeV gamma-rays. In order to calibrate and distinguish the gamma-ray events, we have to know what image a gamma-ray of the specific energy would make on the camera of our telescope. Therefore, I need the detailed study using Monte-Carlo (MC) simulation.

We are developed a simulation of EASs based on GEANT 3.21. GEANT was developed in CERN and provides detector descriptions and simulation for high energy particle

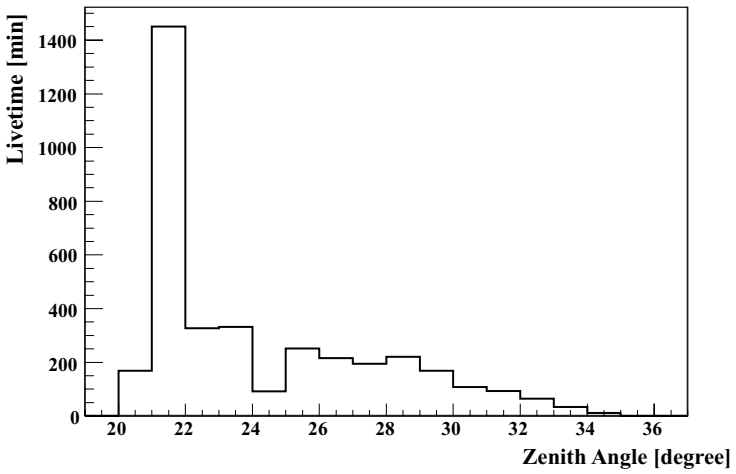

Figure 4.18 Zenith angle distributions of ON run.

interactions. The simulation code mainly consists of four components; the generators of primaries and medium of the atmosphere, the particle interaction description, Cherenkov photon generation, and the telescope response. In the medium description, the atmosphere is divided into 80 layers with an equal thickness of $\sim$12.8 g/cm^2, which is less than a half radiation length. The dependence of the air shower simulation results on the number of these layers was checked by changing the number of layers, and was confirmed to be less than 10 %. In order to evaluate the effect of the number of layers in our simulation, we plotted the mean value of WIDTH distribution by changing the number of layers in Fig.4.19. From this result, the effect of the numbers of layers is almost negligible if we divide the atmosphere into more than 30 layers. The geomagnetic field at the Woomera site was also included; 0.253 G in horizontal and 0.520 G in vertical directions and 6.8 degree from the South.

As for particle tracking in the simulation, the lower energy threshold for a particle transport was set at 20 MeV, which is quite less than the Cherenkov threshold energy of electrons at normal temperature and pressure. In order to save CPU time, only particles whose direction is within a certain degree from the telescope optical axis were selected for tracking to the ground and generate Cherenkov photons. The number of Cherenkov photons generated in the simulation is estimated from the Frank-Tamm formula, and then reduced by multiplying the atmospheric transmittance and PMTs quantum efficiency in advance. Then Cherenkov photons are generated within the calculated Cherenkov angle. As for the atmospheric transmittance, simple Rayleigh-scattering length of 2970 $\times$

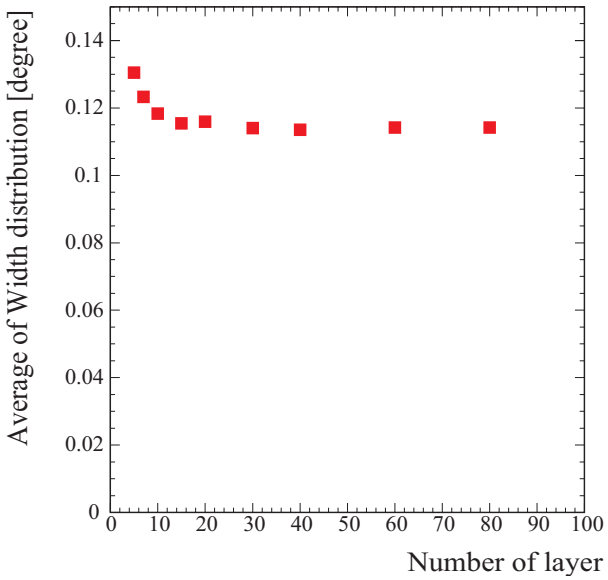

Figure 4.19 Mean value of $WIDTH$ distribution by changing the number of the atmosphere layers in Monte-Carlo code.

$(\lambda/400\ \mathrm{nm})^4$ g cm^{-2} was used in this simulation. As for quantum efficiency, 21 sampling points between 189 nm to 672 nm and for reflectivity 6 sampling points between 200 nm to 800 nm are used to estimate the efficiency. For survived Cherenkov photons, the reflection on the multi-mirror telescopes is calculated assuming perfectly accurate spherical mirror. Photon distribution on the imaging camera is obtained by imposing Gaussian blur with proper width, which is estimated from the muon calibration described below. Every photon is accumulated in finite size PMT pixels.

Night sky background (NSB) photons which were calculated from Jelley's value had also been added to the Cherenkov signals as noises. Nevertheless, since the Jelly's value is just an typical value, I carried out the NSB measurement using 500 MHz flash ADC instead of the charge ADC. Figure 4.20 shows the waveform of the signal from the PMT. The waveform was distorted by the NSB when the camera lid was opened. Figure 4.21 shows the value of NSB on the galactic plane and off the plane. Considering the charge ADC gate width of 100 ns, the NSB value is obtained to be 8 p.e. for on-plane and 4 p.e. for the off-plane. Since the value of on-plain is larger than the Jelly's value of 4 p.e., I used 8 p.e. in the MC simulation for HESS J1614−518 which located on the galactic plane.

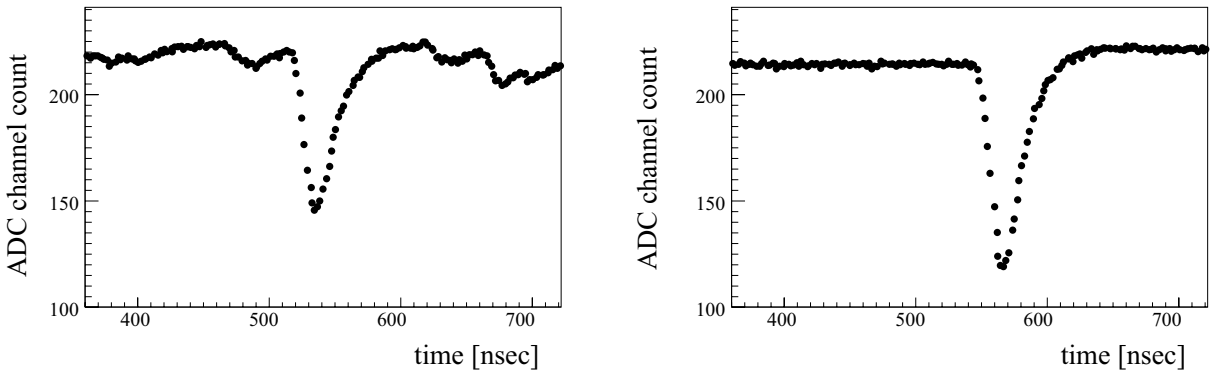

Figure 4.20 Waveform of PMT signal. **Left:** Obtained with the camera lid opened. **Right:** Obtained with the camera lid closed.

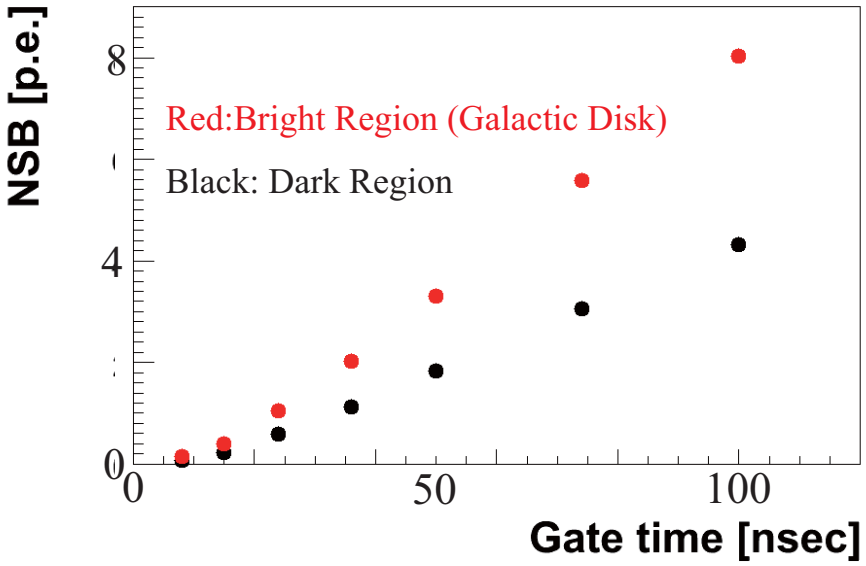

Figure 4.21 Result of the NSB measurement.

Then the response for the Cherenkov photons in each PMT is simulated including electronics modules. The hardware trigger condition is approximately reconstructed in the simulation. Units of outputs of the simulation are perfectly matched to the calibrated real data, and hence both can be analyzed by the same program constructed by the users.

Chapter 5

Analysis

The standard analysis of the CANGAROO-III collaboration (Enomoto et al., 2006a; Kabuki et al., 2007) based on imaging parameters and Fisher discriminant method was applied to the data. Here we describe an outline of the analysis from a raw data to the estimation of the differential flux and morphology.

5.1 Calibration for Cameras and ADCs

The calibrations for the cameras and ADCs were carried out each night using blue-light LEDs. For the calibration data, recorded charges of each pixel in the cameras were converted from ADC channels to the number of photo-electrons. The LEDs were installed in camera shelters. The shelters were completely insulated from external lights by lids. There was a screen on the inner side of the lid, on which particular pattern was printed, to distribute the lights from the LED uniformly on the camera. Lights from the LED are reflected on the screen and uniformly illuminate the PMTs. The LEDs were driven by a pulse generator (AGILENT, 33250A) operated by on-line and flashed with a frequency of 140 Hz and a pulse width of 20 nsec. A synchronized signal from the pulse generator was recorded. After acquiring about 10000 events, the LEDs were turned off and another 10000 events data was recorded as a pedestal data. Using a following relationship,

$$\frac{\sigma_{p.e.}}{\mu_{p.e.}} = \frac{\sigma_{ADC}}{\mu_{ADC} - \mu_{pedestal}}, \tag{5.1}$$

the conversion factor from the ADC channel to the number of photoelectrons was determined, where σ and μ are the standard deviation and mean value, respectively, and the subscripts "p.e.", "ADC", and "*pedestal*" correspond to the distributions obtained at the conversion, the LED run, and the pedestal run, respectively.

5.2 Timewalk corrections

Timewalk corrections for TDC data were carried out from data taken by changing the luminosity of the LEDs. Since photons from the single EAS arrive the cameras within ∼10 nsec, the timing information of each pixel is required to have an accuracy of ∼1 nsec in order to use in analysis. When using a fixed threshold level, timing of the signal usually varies depending on its pulse heights of the input signal. This phenomenon is called "timewalk". The schematic of the timewalk is shown in Fig.5.1. Before the observation, the calibration data for the timewalk corrections was carried out daily. The LED set at the center of the telescope dish was flashed with a random luminosity by the pulse generator, and about 20,000 events data were taken. After the data acquisition, another 10,000 events of pedestal data were taken without the LED flash. From an obtained correlation between the ADC channel and the TDC channel, we correct the timing information. One data set of the obtained correlation was shown in Fig.5.2. Since the integrated charges of ADC have a correlation with the pulse height of the LED, the difference between the arrival time and the absolute time of LED flash, (ΔT), is estimated. Assuming a Gaussian shape for the input pulse waveform, the following equation is obtained as

$$\Delta T^2 = a \log(C - C_0) + b. \tag{5.2}$$

Here C and C_0 are the recorded ADC value for the LED flashing data and pedestal data, respectively. a and b are constants determined from the data. Thus, TDC data are corrected as follow,

$$T' = T - \sqrt{a \log(C - C_0)}. \tag{5.3}$$

Here T' and T are corrected and measured TDC data, respectively. Figure 5.3 shows the distributions of the arrival time of the whole PMTs before and after the correction. The deviation was made to be smaller by the correction.

5.3 Image Cleaning

In IACT, a signal is strongly contaminated by NSB which are observed as a constant pedestal in Fig.5.3. Then, an image cleaning is necessary before calculating "Hillas parameters". In order to reduce the NSB efficiently, cluster cut, ADC cut, and TDC cut were applied to the recorded data.

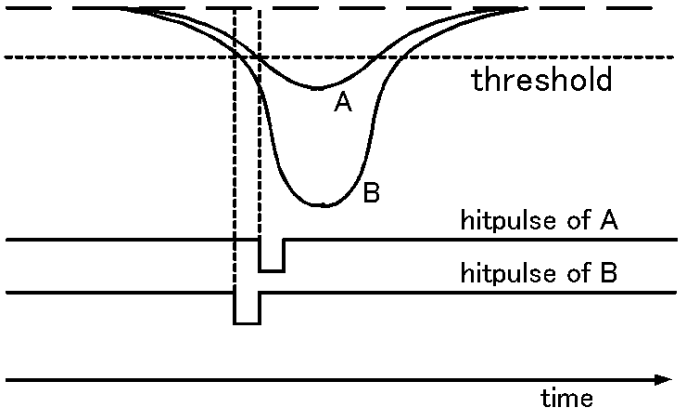

Figure 5.1 The schematic of timewalk (Nakamori, 2008). The timing information varies with the pulse height of input signals, while the actual photon arrival timing is same.

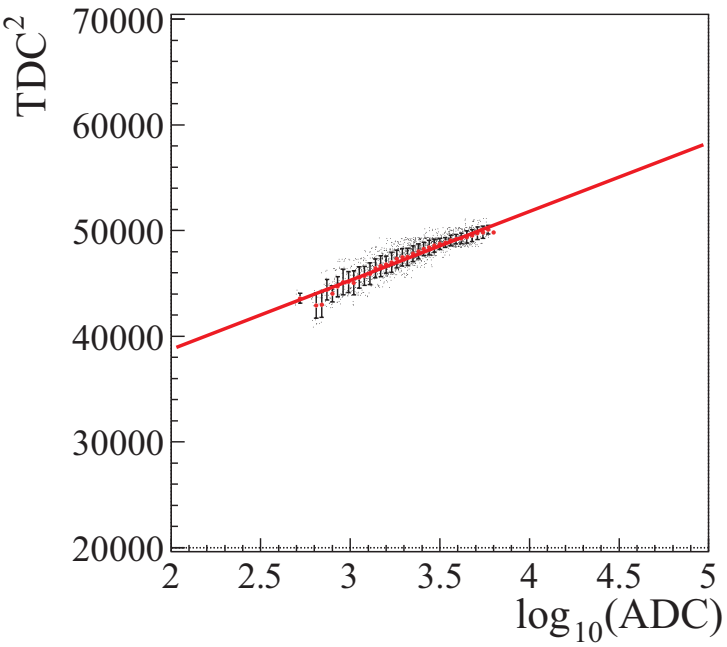

Figure 5.2 An example of the correlation between ADC channels and TDC channels (Nakamori, 2008).

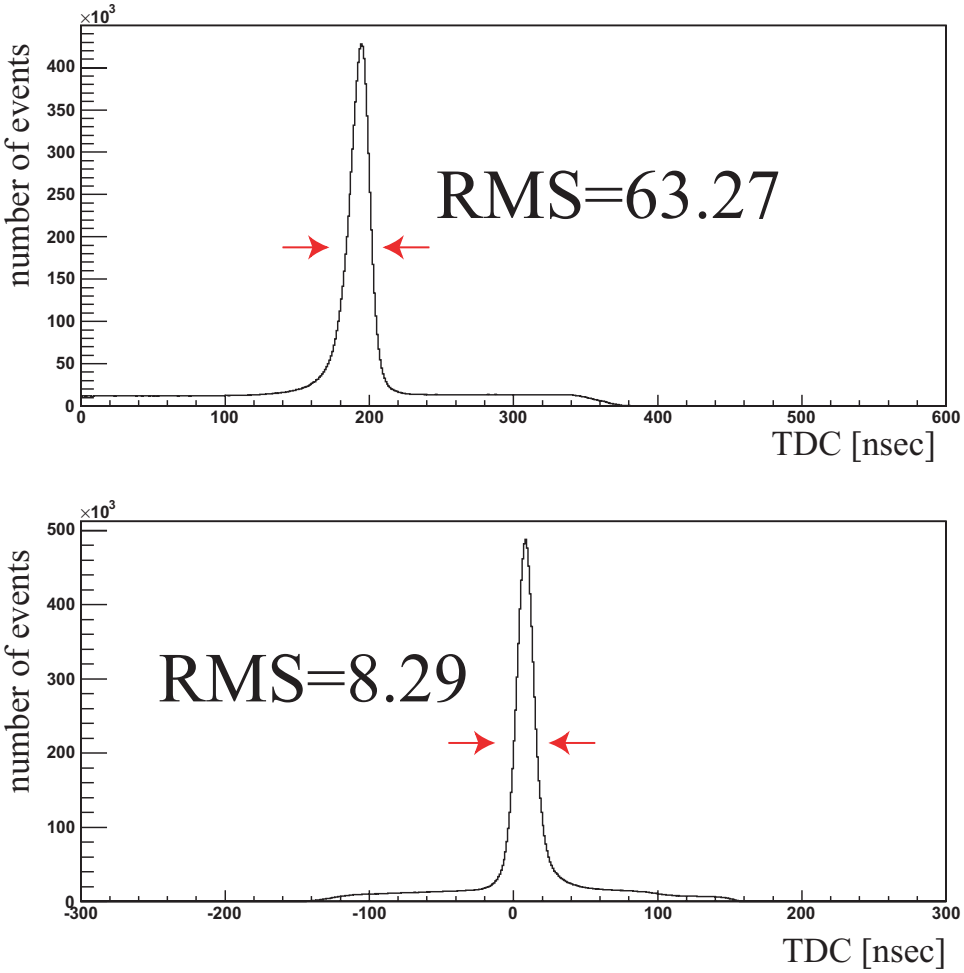

Figure 5.3 Distributions of arrival time of whole PMTs, **top:** before and **bottom:** after the correction (Nakamori, 2008).

Since a shower image is tend to concentrate like a cluster, a separated or isolated hit PMTs are able to regard due to the NSB. Then, we discard these isolated pixels by the cluster cut. A "cluster size" is defined as the number of pixels which constitute the cluster by the shower. We defined this cut as "Tna cut", where n is the number of adjacent pixels required for the cluster. Figure 5.4 shows an example of the cluster cut. In this thesis, I applied T5a cut as the cluster cut.

After the cluster cut, we applied the ADC cut to the data, because the cluster cut cannot remove the NSB hitting the neighboring pixels around the shower cluster. Using the light intensity of the NSB is not as bright as these of showers, we set an light intensity threshold. Figure 5.5 shows the ADC distribution of all channel of T4 and PMTs of which ADC are less than 5 p.e. are discarded.

After the ADC cut, we apply the TDC cut to the data. Since the arrival timing of the NSB signals distribute at random, it can be removed by applying the cuts on the timing distributions. Then, only PMTs with the arrival timing within 30 nsec than mean arrival timing of whole camera were remained. After these cuts, the T5a cluster cut was applied again to the data. Figure 5.6 shows the TDC distributions of T4 before/after those cuts.

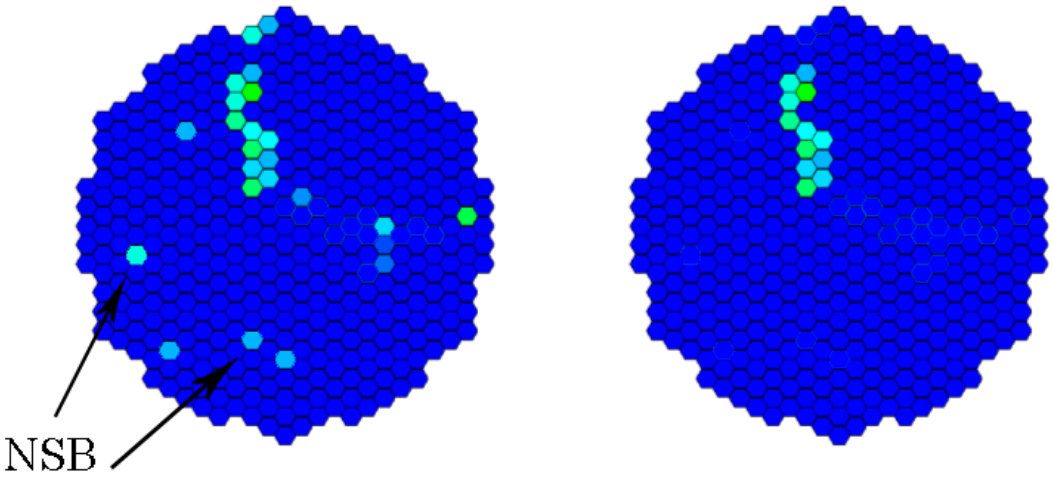

Figure 5.4 An example of the cluster cut (Nakamori, 2008).

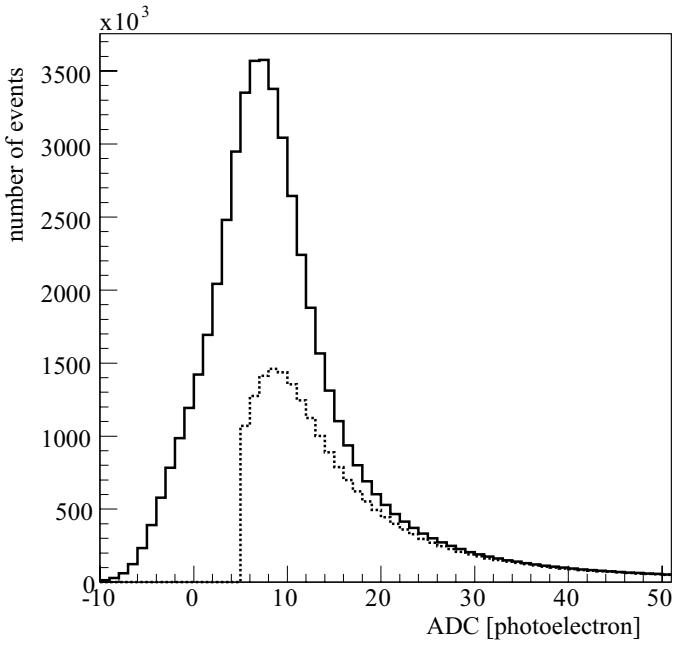

Figure 5.5 ADC distribution of T4 before (solid) and after (dashed) the adc cut (Nakamori, 2008).

5.3.1 Cloud cut

Since there sometimes are clouds in the observed regions of the sky, the shower image on the camera might be distorted by the clouds. Then, I apply the cloud cut. Figure 5.7 shows the trigger rate of T4 in some observation run. Since the trigger rate corresponds to the shower rate, it must be stable and smoothly varied depending on the elevation angle for the clear sky. Thus, we required threshold trigger rate above 5 Hz and abandon the data of period of which a trigger rate is below the threshold.

5.3.2 Edge cut

When energy of the gamma-ray increases, a light amount of an induced shower increases, and a size of the shower image on the camera also increases. Since a chance of the larger image to hit the camera edge increases, an acceptance rapidly drops off for the higher energy gamma-ray. To set a better point in the trade-off relation between the resolutions and the acceptance, we modified the edge treatment.

Figure 5.8 shows examples of the edge treatment of the clusters. In the conventional edge cut, we discarded all events in which outer hit pixels lie on the camera edge. However,

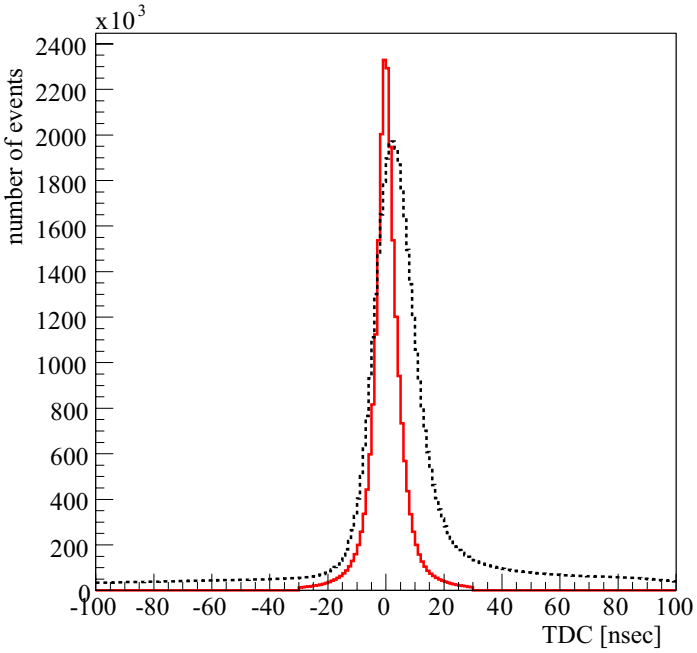

Figure 5.6 TDC distributions of T4 before (black-dotted) and after (red-solid) the image cleaning (Nakamori, 2008).

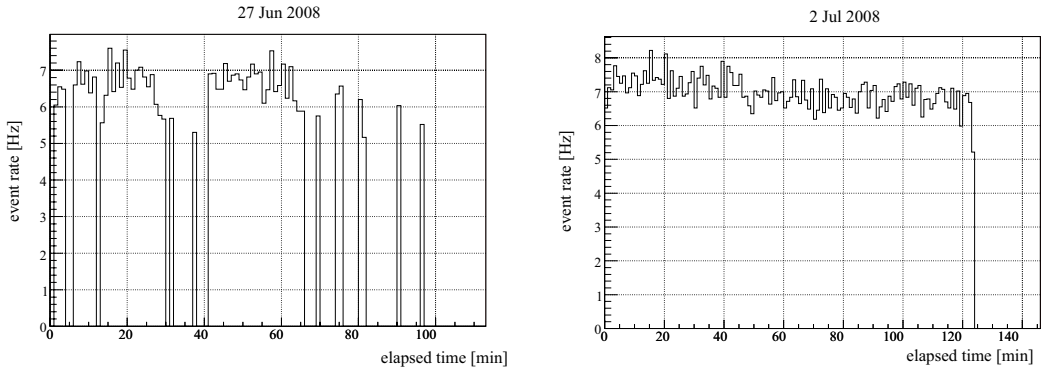

Figure 5.7 Event rates in cloudy (top) and clear (bottom) nights.

for a large image, an image on camera may have an enough information ro reconstruct the direction and the energy, when the most of the hit pixels lies inner the edge. In the modified edge cut, the events of which top 15 hit pixels for the light amount did not hit the camera edge were remained. For this modification, an acceptance for 2 TeV gamma-ray was increased about twice of the conventional edge cut. Figure 5.11 shows the result of applying the modified edge cut to RX J0852.0−4622 (Mizukami, 2007). The modified cut succeeded to obtain a flux of higher energy point.

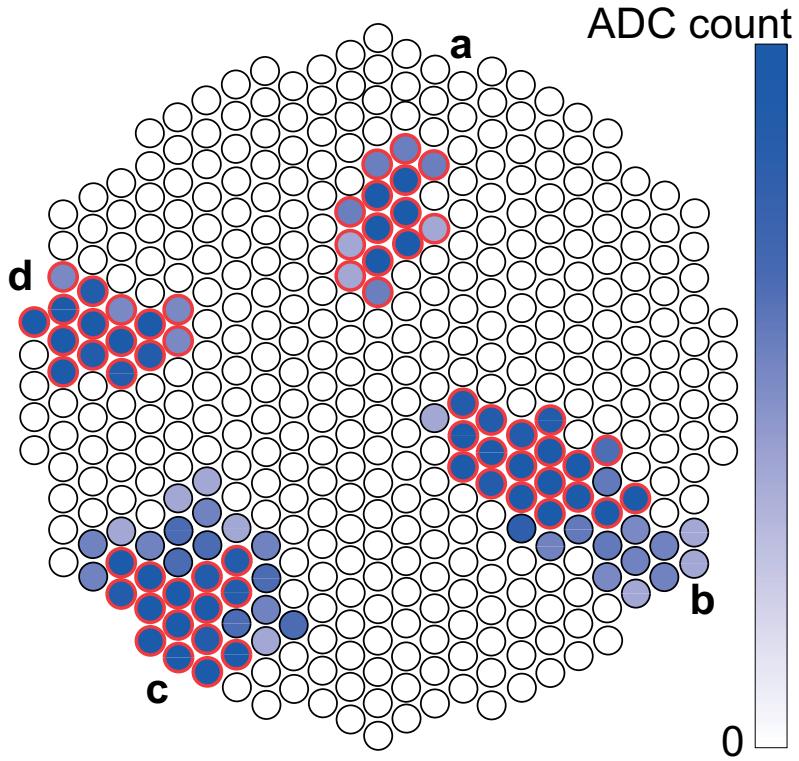

Figure 5.8 Schematic of the edge treatment (Nakamori, 2008). In conventional edge cut, all four images are discarded since they have hit pixels on the camera edge. In core 15 edge cut, image b is not discarded since their top 15 PMTs do not hit the camera edge, while image c and d are discarded.

5.4 Arrival direction determination

For the observation using two telescopes, an arrival direction was determined as an intersection point of the two image axises. However, for the observation using more than

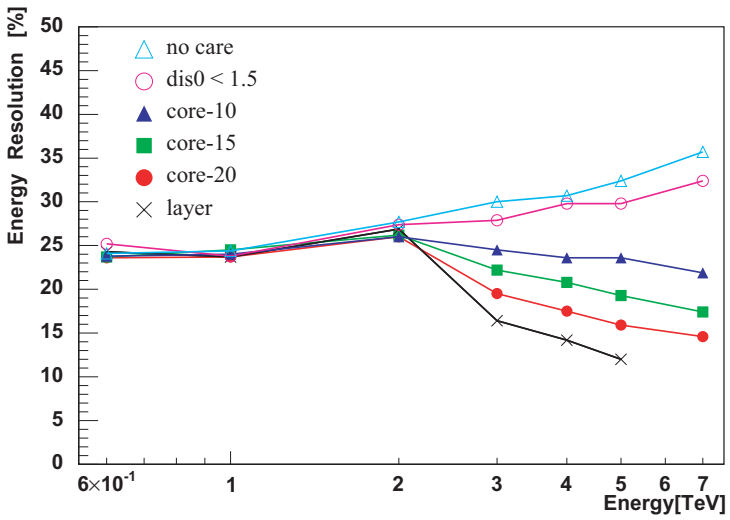

Figure 5.9 Energy resolution for each edge treatment (Mizukami, 2007).

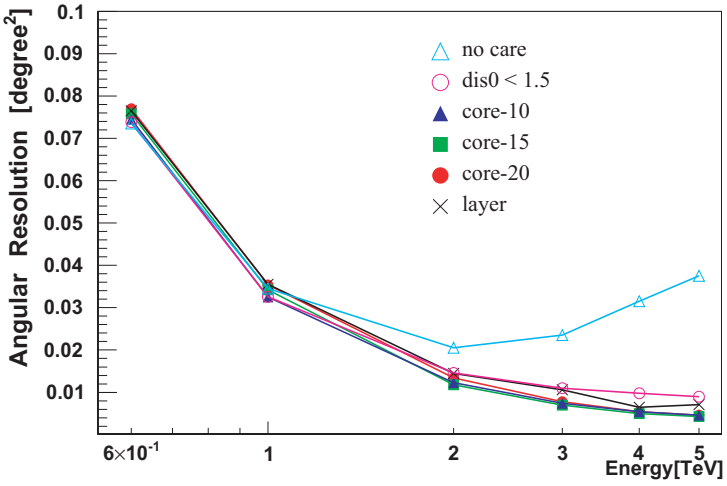

Figure 5.10 Angular resolution for each edge treatment (Mizukami, 2007).

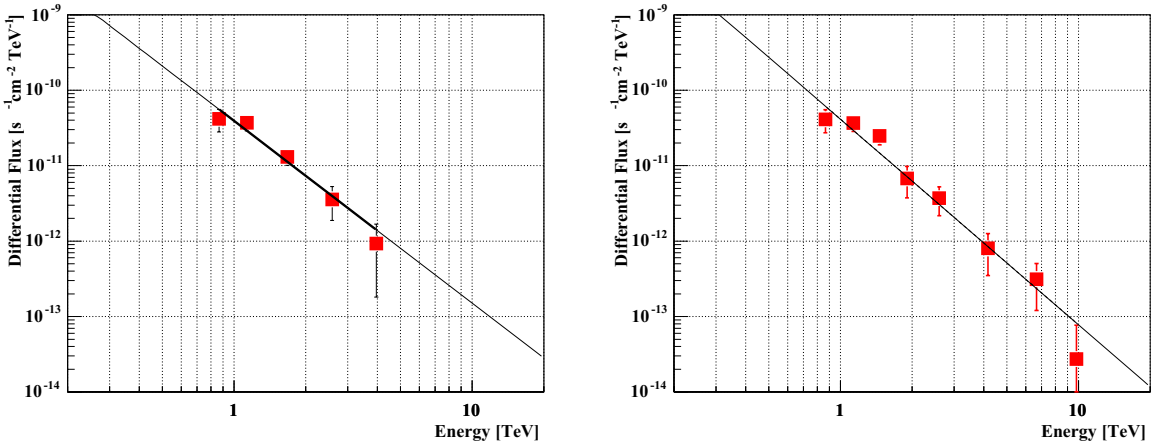

Figure 5.11 Differential flux of RX J0852.0−4622 with the different edge treatment (Mizukami, 2007).**Left:**Conventional edge cut. **Right:**The modified edge cut.

three telescopes, the interaction point cannot be determined uniquely. Hofmann et al. (1999) argued several methods to determine the arrival direction for the multi telescope system. I discuss two methods here. For the method called "Algorithm 1" in Hofmann et al. (1999), Fig.5.12 shows the schematic view of the arrival direction determination. The reconstructed point $(X_{\rm ip}, Y_{\rm ip})$ is described as

$$X_{\rm ip} = \frac{\Sigma x_{mn} \sin\theta_{mn}{}^2}{\Sigma \sin\theta_{mn}{}^2} Y_{\rm ip} = \frac{\Sigma y_{mn} \sin\theta_{mn}{}^2}{\Sigma \sin\theta_{mn}{}^2} \tag{5.4}$$

where (x_{mn}, y_{mn}) and θmn represent the intersection of m-th and n-th telescope and their stereo angle, respectively. This determination method usually provides the more accurate direction when opening angles are closer to 90°.

5.4.1 An determination method for large zenith angle

In the observation at large zenith angle such as the observation of Crab nebula from the CANGAROO site, another determination method is needed since the opening angle becomes quite small. If a reconstructed point is correct, an angular distance between the center of the gravity of the image and the intersection point (here after $D_{\rm ip}$) has to be equal to the Hillas parameter DISTANCE. Then, $D_{\rm ip}$ and DISTANCE are defined as,

$$D_{\rm ip} = \sqrt{(X_{\rm ip} - x_i)^2 + (Y_{\rm ip} - y_i)^2}, \tag{5.5}$$

$$\mathrm{DISTANCE} = \sqrt{(\mathrm{x_0} - \mathrm{x_i})^2 + (\mathrm{y_0} - \mathrm{y_i})^2}. \tag{5.6}$$

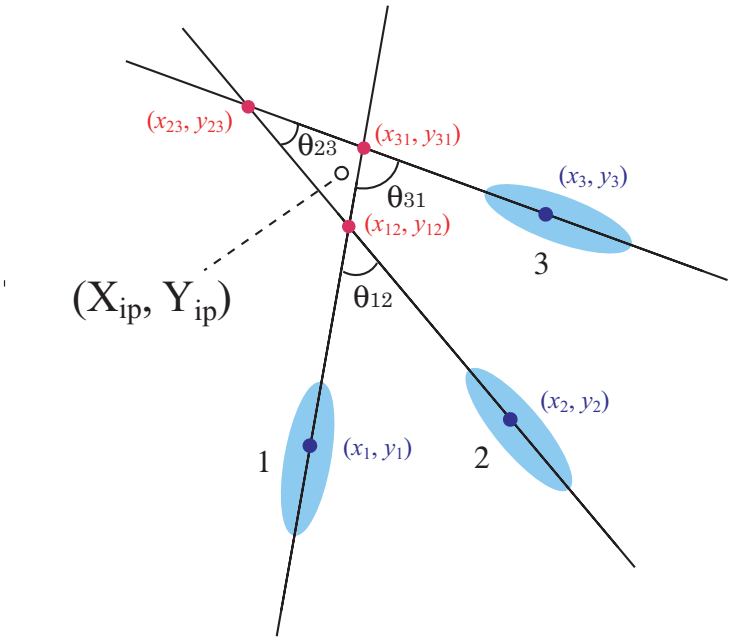

Figure 5.12 Schematics of sine-weighted intersection point determination.

Here, suffix i represents the ID number of the telescopes and (x_0, y_0) represents of the target position. Figure 5.13 shows the correlation between the $D_{\rm ip}$ and DISTANCE of simulated gamma-ray events. You note that the correlation in the large zenith angle is apart from the theoretical line, which indicates that the simple determination method of $(X_{\rm ip}, Y_{\rm ip})$ is inadequate for the large zenith angle. The right figure of Fig.5.13 represents the angular distribution of the reconstructed arrival direction both for small zenith angle and large zenith angle, where the unit of horizontal axis is a squared angular distance between the target position an the reconstructed point. Hereafter we describe this parameter as θ^2, which has been widely used among the TeV gamma-ray experiments.

In order to improve the reconstruction, I have developed a new method called IP-fit. In this method, by using a grid search in the FoV of the camera, I minimize the following χ^2.

$$\chi^2 = \sum_{\rm telescope} (\chi_W^2 + \chi_D^2). \tag{5.7}$$

Here χ_W is the constraint on the WIDTH calculated from the assumed intersection position in the grid search (Fig.5.14). The parameter WIDTH (W) and LENGTH (L) are the standard deviation along with the minor and major axises of the Hillas ellipse,

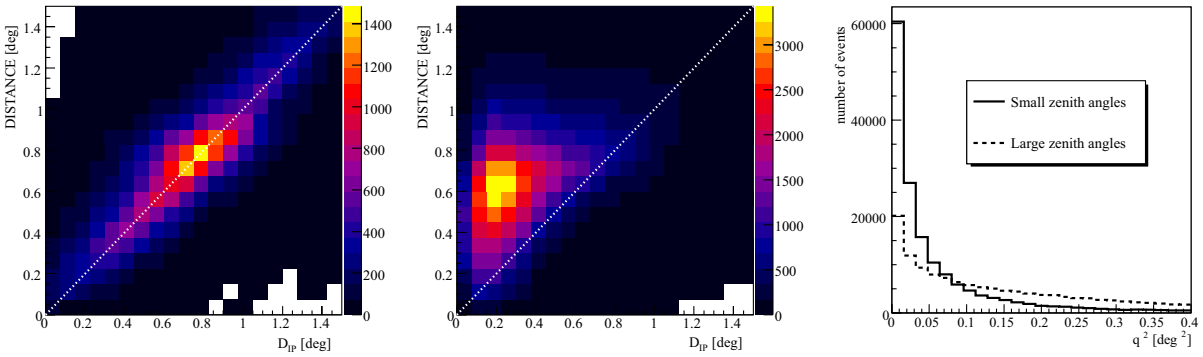

Figure 5.13 Dip and DISTANCE correlations (Nakamori, 2008). **Left:** small zenith angle. **Center:** large zenith angle. **Right:** Simulated $theta^2$ distributions for small (solid line) and large (dashed line) zenith angle.

respectively. Modified WIDTH w' is derived from the error propagation formula,

$$w'^2 = (W\cos\theta)^2 + (L\sin\theta)^2, \tag{5.8}$$

where θ is defined as shown in Fig.5.14. Then we defined χ_W by w' weighted by its SIZE (s_i) as,

$$\chi^2_W = s_i w'^2 = s_i((W\cos\theta)^2 + (L\sin\theta)^2). \tag{5.9}$$

Here SIZE is defined as the sum of photoelectrons for the hit pixels in the cluster. Second constraint is on $D_{\rm ip}$. DISTANCE is predicted by the Monte-Carlo simulation as a function of LENGTH divided by WIDTH, f(W/L). Since DISTANCE= D_{ip}, when the reconstruction point is equal to the source position, the constraint can be written as,

$$\chi^2_d = \left(\frac{D_{ip} - f(\mathrm{L/W})}{\sigma}\right)^2, \tag{5.10}$$

where σ represents a deviation of D_{ip}. Figure 5.15 shows a correlation between DISTANCE and L/W. In our analysis, we use f(W/L) as following form,

$$f(\mathrm{L/W}) = \min(\sqrt{\mathrm{L/W} - 1}, 0.95), \tag{5.11}$$

This function is represented in Fig.5.15 as a solid line. In order to match the dimension of χ^2_d and $\chi^2_{\rm W}$, we multiplied $n\mathrm{W}^2$ to χ^2_d, where n is a constant value corresponding to the number of photoelectrons. Figure 5.16 shows the correlation between n and PSF. I

applied $n = 10$, which gives the best PSF value. Finally I obtain the constraint as,

$$\chi^2 = \sum_{telescope} (s_i w'^2 + 10\mathrm{W}^2\chi_d^2). \tag{5.12}$$

Figures 5.17 and 5.18 show the DISTANCE-D_{ip} correleation and the θ^2 distributions for gamma-ray simulations at zenith angle of the Crab nebula, respectively. By the IP-fit, PSF has been improved from 0.22 deg^2 up to 0.06 deg^2.

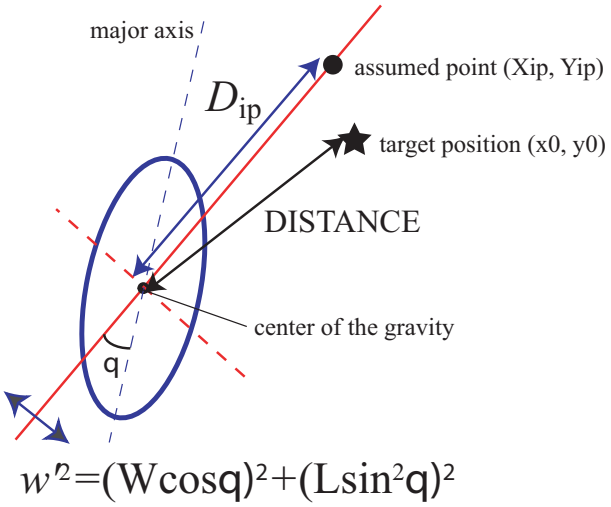

Figure 5.14 Parameters used in IP-fit.

5.5 Gamma/Proton separation –Fisher Discriminant Method–

After the shower image cleaning, we have to select gamma-ray events from enormous proton events. The separation of gamma-rays from proton showers is done using a difference of both Hillas parameters, such as WIDTH and LENGTH. Figure 5.19 shows WIDTH and LENGTH distributions of both gamma-ray simulation and proton observation. In conventional square cuts for imaging parameters, we simply subtract OFF-data from ON-data after applying those square cuts. However, the conventional image cut cannot provide a optimized separation of gamma-ray events and furthermore there always exists some human bias on the determination of the cut parameters. Thus, I adopted a method called Fisher Discriminant method (Fisher , 1936) to the analysis, which is now widely used in high energy physics experiments (Abe et al., 2001).

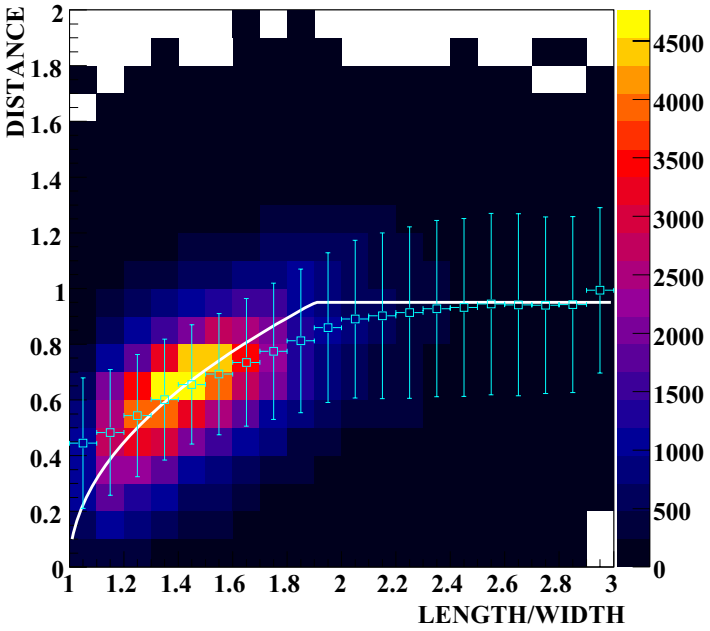

Figure 5.15 Correlation between LENGTH/WIDTH and DISTANCE (Nakamori, 2008). White solid line shows f(W/L).

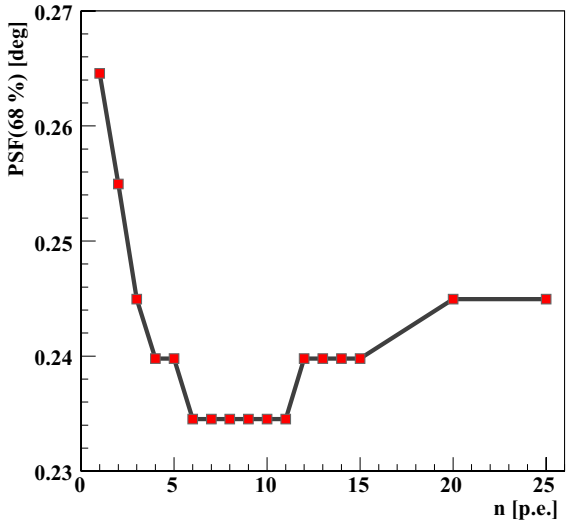

Figure 5.16 n value dependence against PSF (Nakamori, 2008).

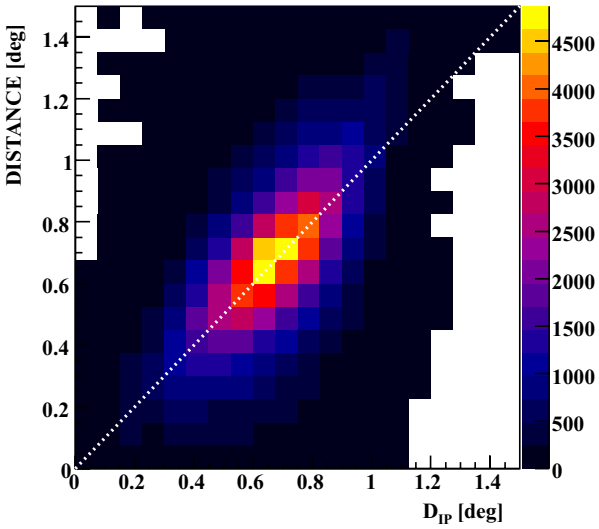

Figure 5.17 Dip and DISTANCE correlation ob tained with IP-fit for gamma-ray simulation of Crab nebula (Nakamori, 2008). Correlation is close to the ideal line (white dashed line).

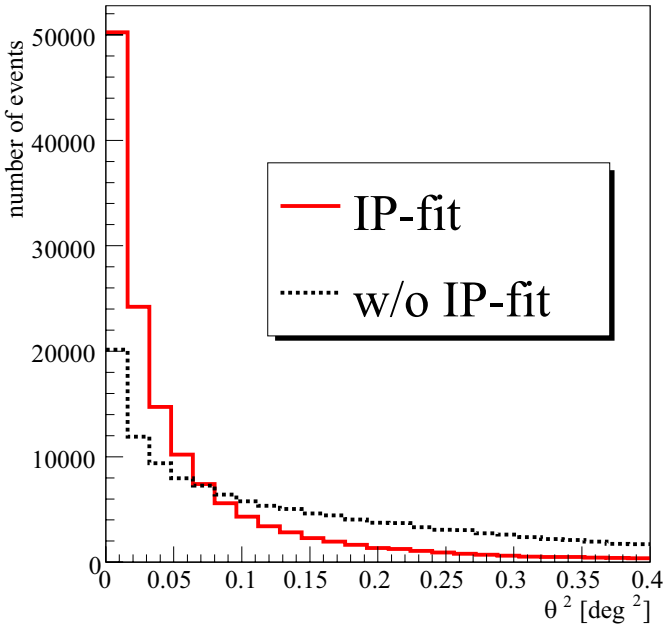

Figure 5.18 θ^2 distributions with IP-fit (red solid line) and without IP-fit (black dotted line) for gamma-ray simulation of Crab nebula (Nakamori, 2008).

For the observation by two telescopes, we use four parameters (W_3, W_4, L_3, L_4), and $\vec{P}$ is defined as,

$$\vec{P} =^t (W_3, W_4, L_3, L_4), \tag{5.13}$$

where a suffix represents an index of telescopes. Fisher Discriminant F is determined by the linear combination of each term,

$$F = \vec{\alpha} \cdot \vec{P}. \tag{5.14}$$

The coefficient $\vec{\alpha}$ is determined as follows. When Fisher discriminants F for gamma-ray simulation (F_γ) and for background (F_b) are derived, separation index D of the two distributions is defined as,

$$D \equiv \frac{(< F_\gamma > - < F_b >)^2}{\sigma_\gamma^2 + \sigma_b^2}, \tag{5.15}$$

where σ is a deviation of the F distribution and the bracket is a mean of the F distribution. Then, α is determined as maximize D, by $\partial D/\partial \vec{\alpha} = 0$,

$$\vec{\alpha} = (\tilde{E}_\gamma + \tilde{E}_b)^{-1}(< \vec{P}_\gamma > - < \vec{P}_b >). \tag{5.16}$$

E is called Error matrix and its elements are described as,

$$E_{ij} =< P_i P_j > - < P_i >< P_j > . \tag{5.17}$$

Then, a following treatment to reduce the number of the parameters is added. For each SIZE bin, I subtract the mean values of WIDTH and LENGTH distribution from these distributions itself. By this treatment, $< F_\gamma >= 0$ is obtained independently of SIZE. Figure 5.20 shows the correlation between WIDTH or LENGTH and $\ln s$. The solid line shows the fitted line by a quadratic function. For each event, P_i' is determined as,

$$P_i' = P_i - (a(\ln s)^2 + b \ln s + c), \tag{5.18}$$

where a, b, and c are determined by the fitting. Then we can determine FD value using $\vec{P}'$. F_γ and F_b are obtained using simulated gamma-ray events and real events located in $0.3 < \theta^2 < 0.5$ deg^2 region. Figure 5.21 shows the obtained F_γ and F_b distributions for HESS J1614−512 analysis.

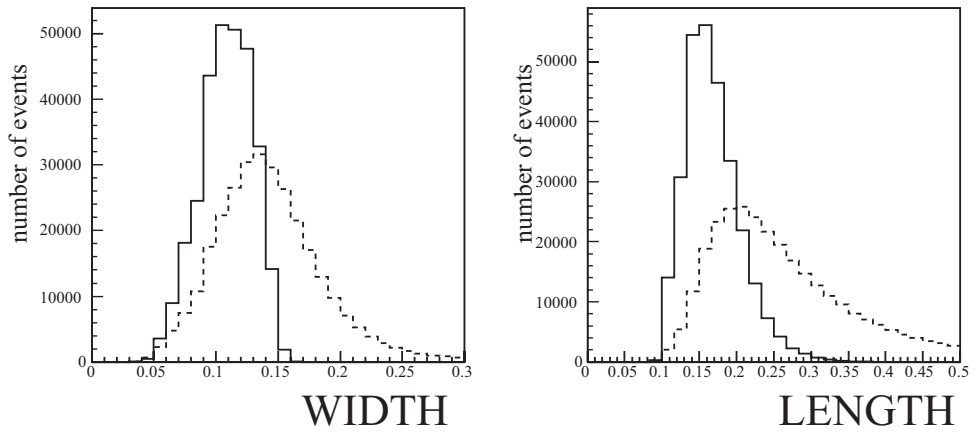

Figure 5.19 The WIDTH and LENGTH distributions of T4 for both background observation for Crab nebula and the gamma-ray simulation (Nakamori, 2008).

5.5.1 Fisher fit

The F distribution obtained by the observations for the gamma-ray source can be assumed to be a superposition of F_γ and F_b as,

$$F = \alpha F_\gamma + (N - \alpha) F_b, \tag{5.19}$$

where N is the number of observed event and α is the number of the gamma-ray events. By fitting the observed F distribution by F_γ and F_b, α is obtained. When the i-th bin value of F_γ and F_b are γ_i and b_i, respectively, the fitting is equivalent to minimize following the χ^2,

$$\chi^2 = \sum_i \left(\frac{n_i - \alpha\gamma_i - (N - \alpha) b_i}{\sqrt{n_i}} \right), \tag{5.20}$$

where n_i is the number of the events in the i-th bin of F distribution. By $d\chi^2/d\alpha = 0$, α is obtained as,

$$\alpha = \frac{\sum_i (b_i - \gamma_i)(1 - N\frac{b_i}{n_i})}{\sum_i \frac{(b_i - \gamma_i)^2}{n_i}}. \tag{5.21}$$

A deviation of α, σ_α, is obtained by the propagation of the error,

$$\sigma_\alpha^2 = \sum_i (\sqrt{n_i})^2 \left(\frac{\partial \alpha}{\partial n_i} \right) \tag{5.22}$$

Figures 5.21 and 5.22 show an obtained fit result in HESS J1614−518. We obtained gamma-ray excess event of 950 ± 107 events in the region of $\theta^2 < 0.2$ deg^2, with significant level of 8.88 σ.

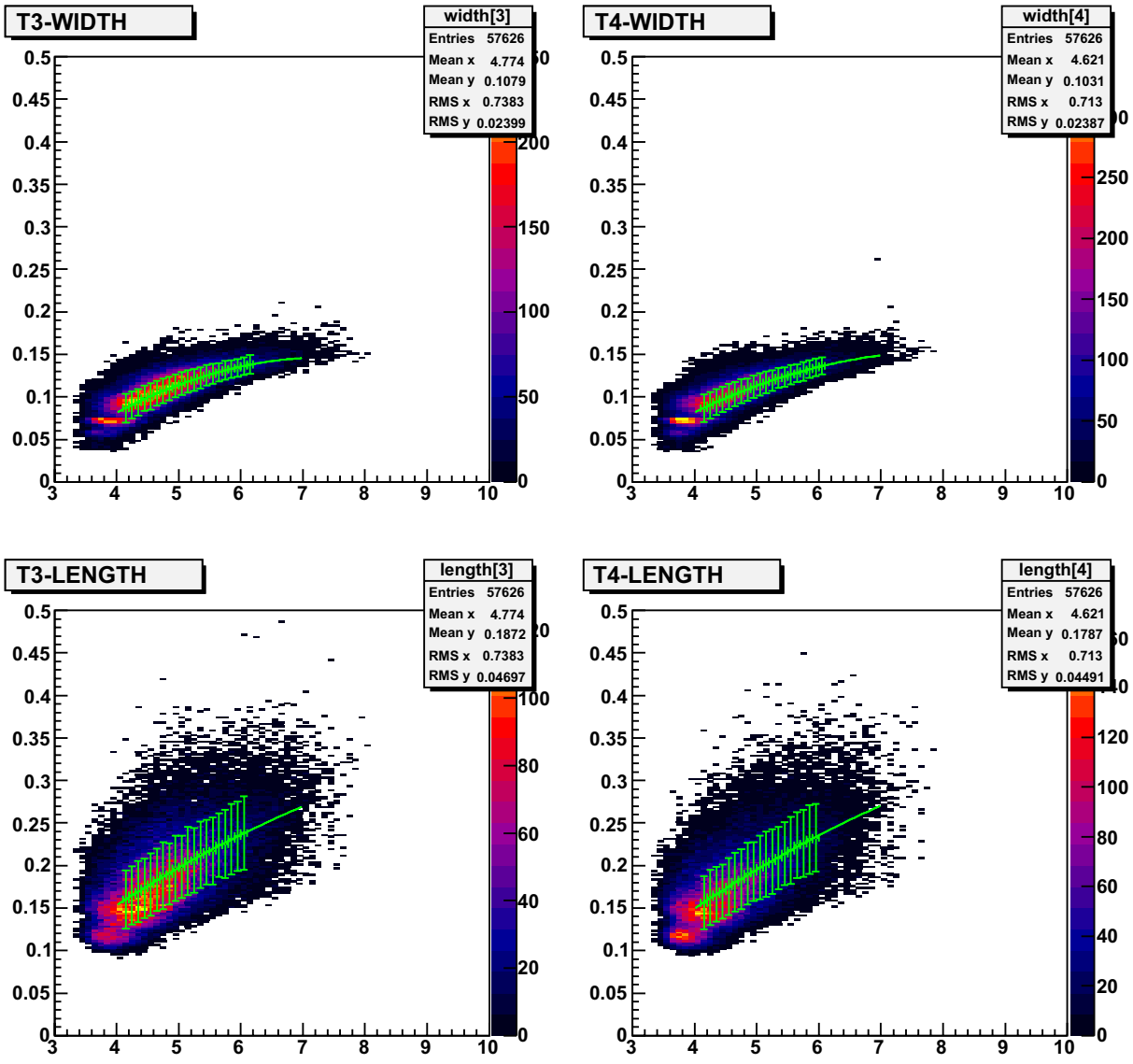

Figure 5.20 Correlation between LENGTH (bottom), WIDTH (top) and ln(SIZE) for T3 (left), and T4 (right).

To investigate the systematic error by the region size, I applied the above analysis with the region size from 0.12 to 0.40 deg^2. The obtained number of events were shown in Fig.5.23. Below the region size of 0.2 deg^2, the excess number reduced due to under estimation of the emission size. Above the size of 0.2 deg^2, the excess number saturated while the error increases. Thus, I used the region size of $\theta^2 < 0.2$ deg^2.

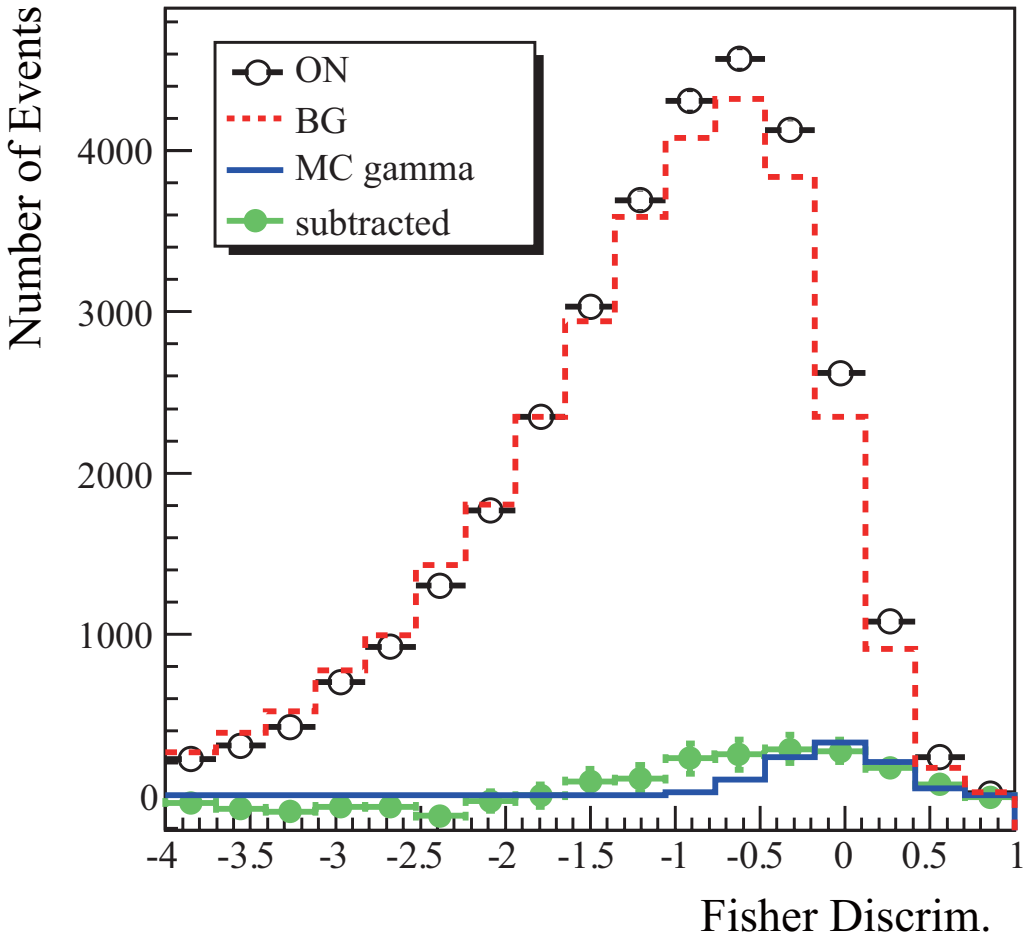

Figure 5.21 Fisher discriminant F distributions. The ON, BG distributions are obtained by the real run with θ^2 region of $\theta^2 < 0.2$ degree^2 and $0.3 < \theta^2 < 0.5$ degree^2, respectively. The MC gamma distribution is calculated by the gamma-ray simulation. The BG and MC gamma distributions are normalized by the Fisher fit. The subtracted distribution is the subtraction of ON and BG distribution

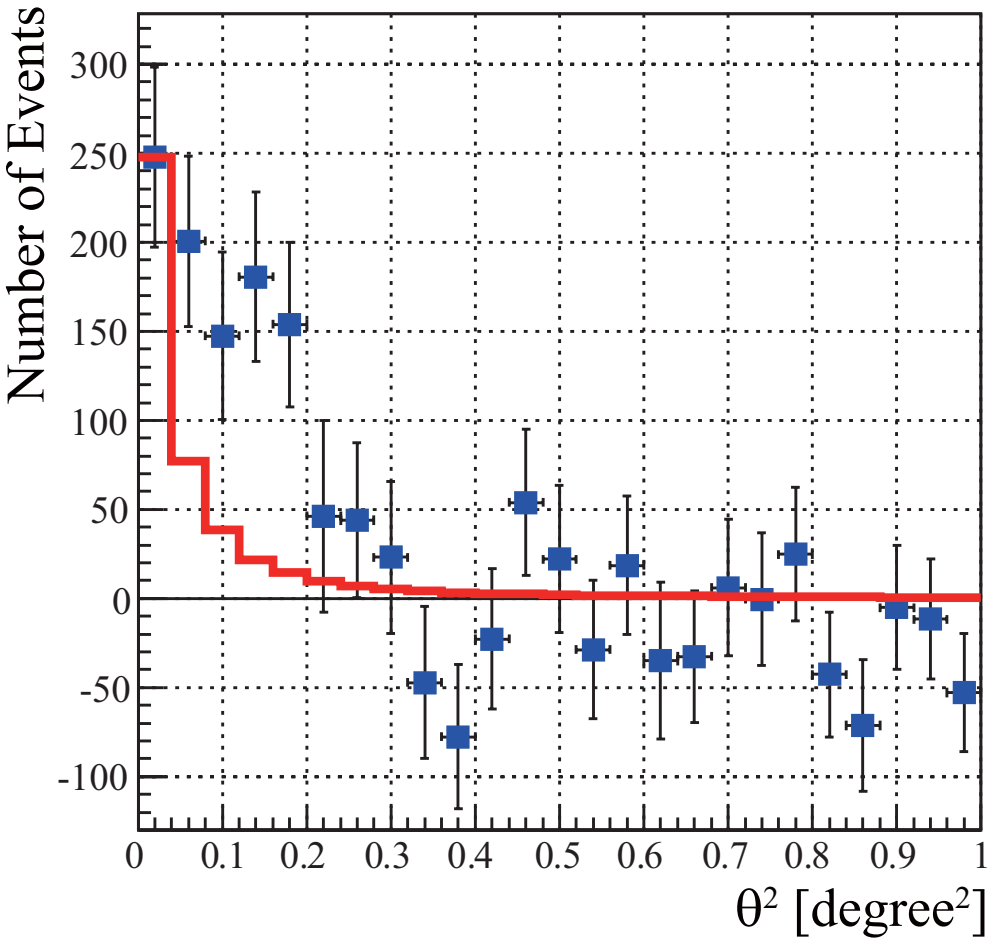

Figure 5.22 The θ^2 plot, where $\theta^2 = 0$ corresponds to the fitted center of gravity of HESS J1614−518 from H.E.S.S. (Aharonian et al., 2006a). The blue data points represents the excess events in each θ^2 bin and the red solid line represents our PSF derived from the Monte-Carlo simulation.

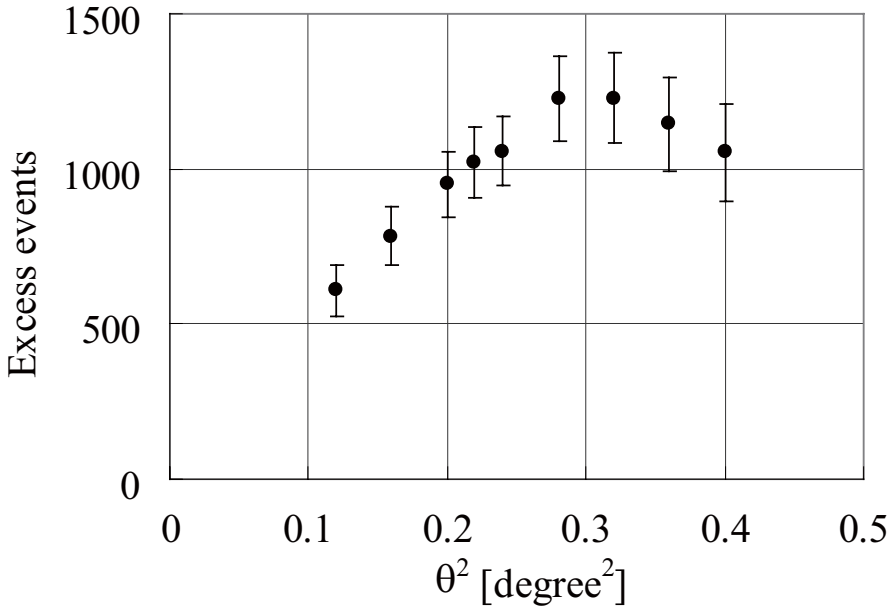

Figure 5.23 The excess event number variations against different excess region taking.

5.6 Differential Flux

In order to calculate a differential flux, we first obtain the number of excess events for each size bin from s_1 to s_2, where s_1 and s_2 are mean size values for the each telescope. Then we calculate a corresponding gamma-ray energy $\bar{E}(s_1, s_2)$ as the mean of the gamma-ray energy distribution of the gamma-ray simulation after the size cut $s_1 < s < s_2$ and effective area $S(s_1, s_2)$. The effective area $S(s_1, s_2)$ is obtained by the product of an acceptance A and the area of gamma-ray injection S_0,

$$S(s_1, s_2) = A(s_1, s_2)S_0 = \frac{n(\bar{E})}{N(\bar{E})}S_0, \tag{5.23}$$

where N and n is generated and detected the number of gamma-rays, respectively. Here $S_0 = \pi r_0^2 \cos z$, $r_0 = 2.5 \times 10^5$ cm and z is a mean zenith angle throughout the observation period. When we describe the excess events for the each size bin as $\alpha(s_1, s_2)$, the number fo gamma-rays per a ground area can be expressed as α/S. Thus, the differential flux dF/dE is obtained as,

$$\frac{dF}{dE}(s_1, s_2) = \frac{\alpha(s_1, s_2)}{St_{obs}}, \tag{5.24}$$

where t_{obs} is the effective observation time. Obtained differential flux is shown in Fig.5.24. The spectrum is consistent with a single power law: $(8.2 \pm 2.2_{\rm stat} \pm 2.5_{sys}) \times 10^{-12} \times (E/1{\rm TeV})^{-\gamma}$ cm^{-2}s^{-1}TeV^{-1} with a photon index γ of $2.4 \pm 0.3_{\rm stat} \pm 0.2_{\rm sys}$. Relevant systematic errors are due to the atmospheric transparency, night-sky background fluctuations, uniformity of camera pixels, and light-collecting efficiencies. In addition, to estimate the systematic error due to the size of the signal integration region, I changed the region from $\theta^2 < 0.14$ deg^2 to 0.40 deg^2, which was included in the systematic error. For the confirmation of the systematic error due to the background region, I took a background region $\theta^2 < 0.2$ deg^2 from the opposite positions of HESS J1614−518 observations in the wobble mode as described in Chapter 4. This analysis provides a differential flux of $(6.4 \pm 2.0_{\rm stat} \pm 2.4_{sys}) \times 10^{-12} \times (E/1{\rm TeV})^{-\gamma}$ cm^{-2}s^{-1}TeV^{-1} with a photon index γ of $2.4 \pm 0.6_{\rm stat} \pm 0.3_{\rm sys}$, which was consistent with that derived with the ring-region background. Obtained flux in the ring background region was consistent with the result of H.E.S.S. as shown in Fig.5.24.

5.7 Morphology

We obtained a gamma-ray sky map by the FD fit method applying to the each grid on the FoV of the camera. The number of excess events were individually estimated in each grid bin of $0.2^\circ \times 0.2^\circ$ square. This bin size is determined by PSF of 0.23 degree. The morphology of gamma-ray-like events, obtained from a Gaussian smoothing with the CANGAROO-III PSF of 0.24 deg, is shown in Fig.5.25. The extent of the VHE gamma-ray emission was estimated by a two-dimensional Gaussian fit on our excess map. The obtained standard deviation was 0.44 ± 0.03 deg which is surely broader than the CANGAROO-III PSF. The centroid position was determined to be (RA., decl. [J2000])= $(243^\circ.634, -51^\circ.950)$. The offset from the best-fit position reported by H.E.S.S. is (ΔR.A., Δdecl.)= $(0^\circ.055 \pm 0^\circ.018, -0^\circ.130 \pm 0^\circ.033)$. The offset is within our PSF. A systematic difference due to the difference in energy thresholds between H.E.S.S. and CANGAROO-III may also contribute to this offset.

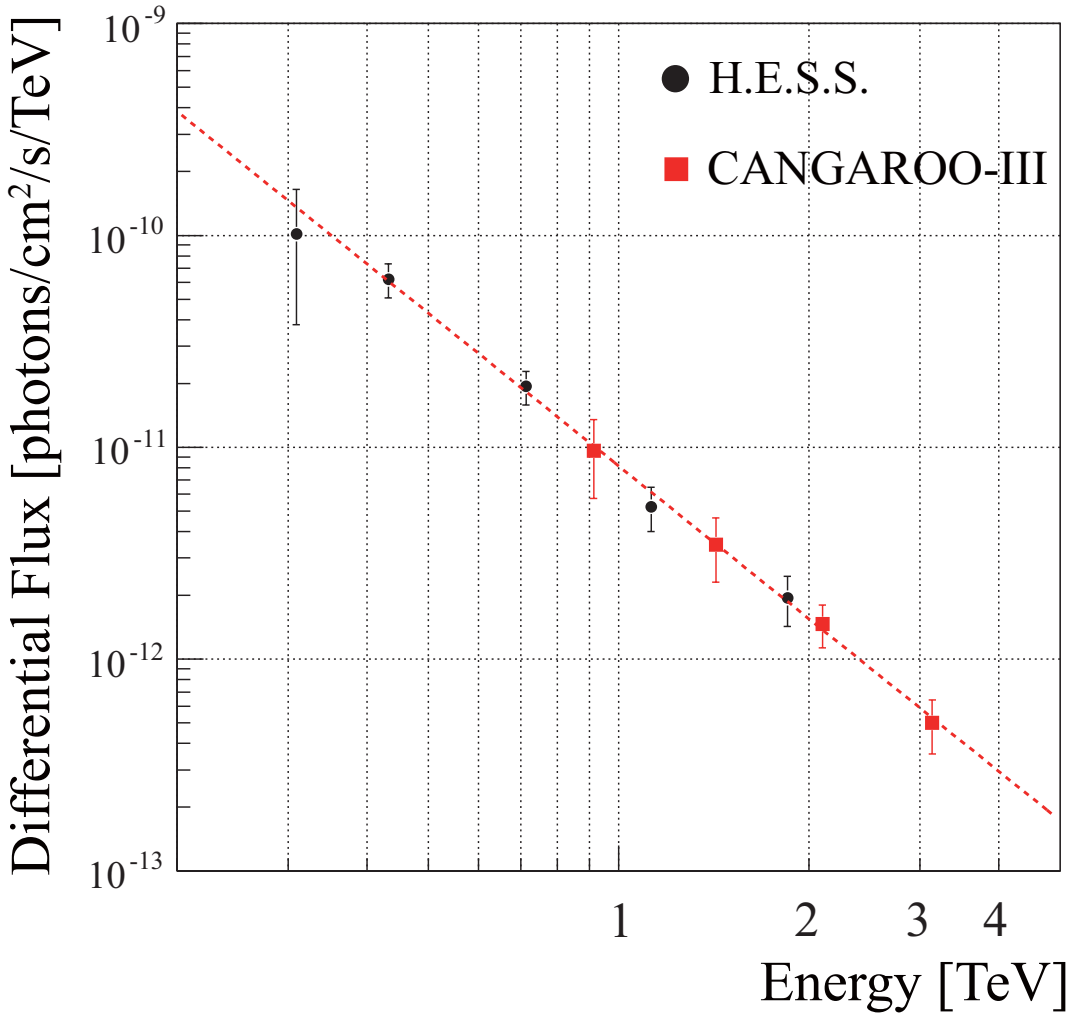

Figure 5.24 Differential flux of HESS J1614−518. Squares and circles show the CANGAROO-III and the H.E.S.S. data points, respectively. The best fit power-law from this work is shown by the dotted line.

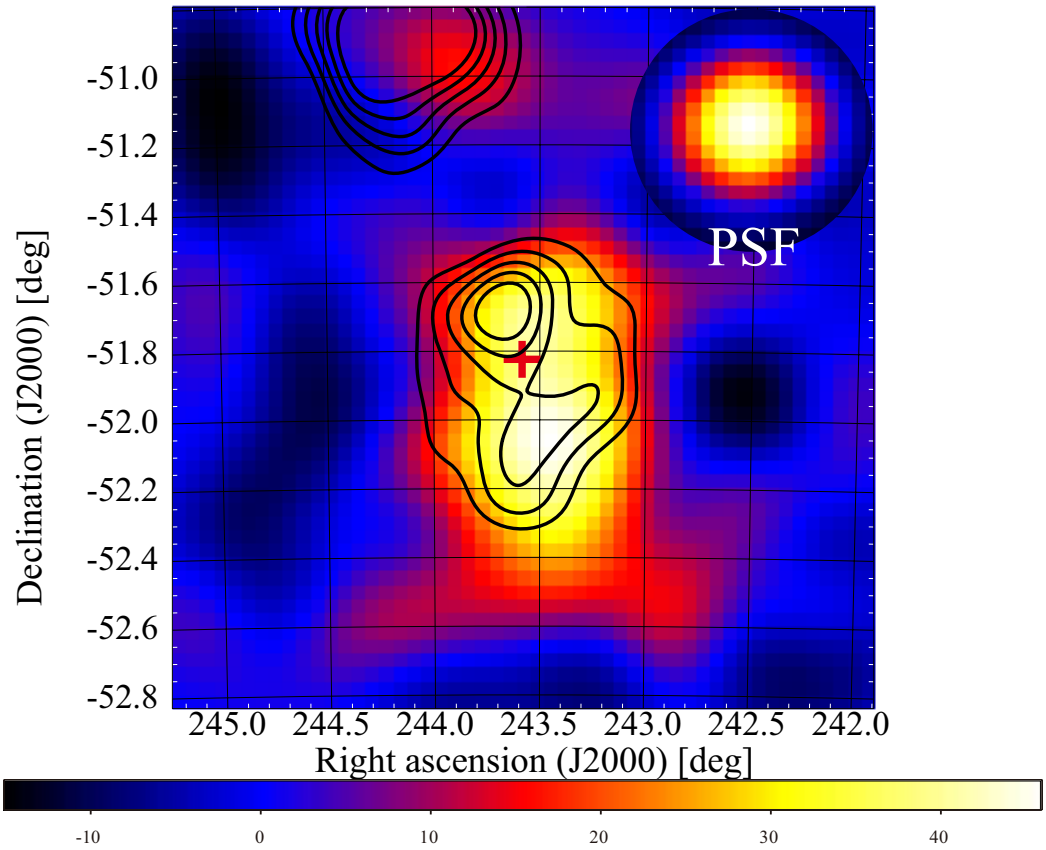

Figure 5.25 Morphology of gamma-ray–like events. The number of excess events per $0°.04 \times 0°.04$ cell is smoothed by a Gaussian with $\sigma = 0.24$ degree, which is the CANGAROO-III PSF, and plotted in equatorial coordinates. The black solid contours show the VHE gamma-ray emission seen by H.E.S.S. Lines correspond to 20, 30, 40, 50, & 60 gamma-ray counts. The red cross shows the H.E.S.S. center of gravity of HESS J1614−518 (Aharonian et al., 2006a).

Chapter 6

Discussion

I now discuss the plausible radiation mechanisms of HESS J1614−518 using the results of CANGAROO-III, H.E.S.S., *Fermi*, and *Suzaku* observations. Since the spectra of *Swift* sources were not available, I did not use the *Swift* data. Figure 6.1 shows the morphological relationship between each observation. The non-thermal X-ray emission from Suzaku source A is positioned very close to the H.E.S.S. gamma-ray peak, the position of the *Fermi* source 1FGL J1614.7-5138c, and within the emission region detected with CANGAROO-III. Thus, this could be the most likely counterpart for HESS J1614−518. I note here that since the FOV of the *Suzaku* observation covered only the part of the TeV gamma-ray emission region, as shown in Fig.6.1, the current observed X-ray flux may only be a fraction of the entire X-ray emission from the entire region of the VHE gamma-ray emission. For further constraints on emission models, I tried to derive the flux at 8 μm at the Suzaku source A position, from the archival data with the Infrared Array Camera (IRAC; Fazio et al. (2004)) onboard the *Spitzer* Space Telescope. However, due to the contamination from a nearby source, I obtained only an upper limit.

Since the observed VHE gamma-ray emission was diffuse and located on the galactic plane, HESS J1614−514 is regarded as a galactic source. Galactic sources were known to be classified into SNRs, PWNe, massive star clusters, giant molecular clouds, or X-ray binaries, We can exclude the possibility that HESS J1614−514 is the binary, since this type of source shows a point-like emission, which is in contrast to the results of CANGAROO-III. The giant molecular scenario is also excluded since Rowell et al. (2008) reported that they found no obvious overlapping molecular clouds across a range of inferred distances up to ∼6 kpc, with the NANTEN ^{12}CO(J=1-0) survey data (Matsunaga et al., 2001). Then, I discussed three scenarios here.

SNR Scenario: Suzaku source B, which may be related to a possible AXP, is positioned roughly in the center of the VHE gamma-ray emission. I thus postulate a scenario in which a supernova explosion occurred at the position of Suzaku source B and the shock of the SNR has now reached the position of Suzaku source A, emitting both the X-ray and gamma-ray emission. In this scenario, I used a distance of 10 kpc which was determined by the absorption feature of *Suzaku* observation.

Another possibility is an association between an SNR and the open cluster, since Pismis 22 is old enough for some massive stars to finish their life as supernovae. In this case, I used a distance of 1 kpc which is the distance to Pismis 22 in discussion.

PWN Scenario: A PWN is also strong candidate of diffuse gamma-ray emission. Five pulsars have been found in this region, PSR J1611−5209, PSR J1612−5136, PSR J1613−5211, PSR J1614−5144, and PSR J1616−5208 (Manchester et al., 2005; ATNF Pulsar Catalogue ver.1.38). As described in Chapter 2, Suzaku source B would be a PWN if associated with a pulsar or AXP. The size of Suzaku source A or source B is smaller than that of the VHE gamma-rays, which feature is also founded in other PWNe because of synchrotron cooling (Chapter 2). I will discuss the PWN scenario and the associated pulsar which could supply enough particles to reproduce both the X-ray emission of Suzaku source A or source B and the VHE gamma-ray emission.

Stellar Wind Scenario: The young open cluster Pismis 22 is located towards the center of HESS J1614−518 and is also a possible counterpart. Its age is $\sim 4.0 \times 10^7$ yr and the distance is 1 ± 0.4 kpc from the Earth. The coincidence between a young open cluster and a VHE gamma-ray source is also found in Westerlund 2 and Cyg OB2 as described in Chapter 2. Stellar winds from massive stars in the cluster could form a shock front, accelerate charged particles, and produce the high energy radiation (Voelk & Forman, 1982; Bednarek, 2007).

6.1 SNR Scenario

In the SNR scenario, I assumed that the X-rays from Suzaku source A and the VHE gamma rays are emitted by charged particles accelerated by the shock in the SNR shell, and Suzaku source B is an associated AXP which is positioned in the center of the SNR shell. Additionally, I will discuss the possible correlation between the SNR and Pismis 22.

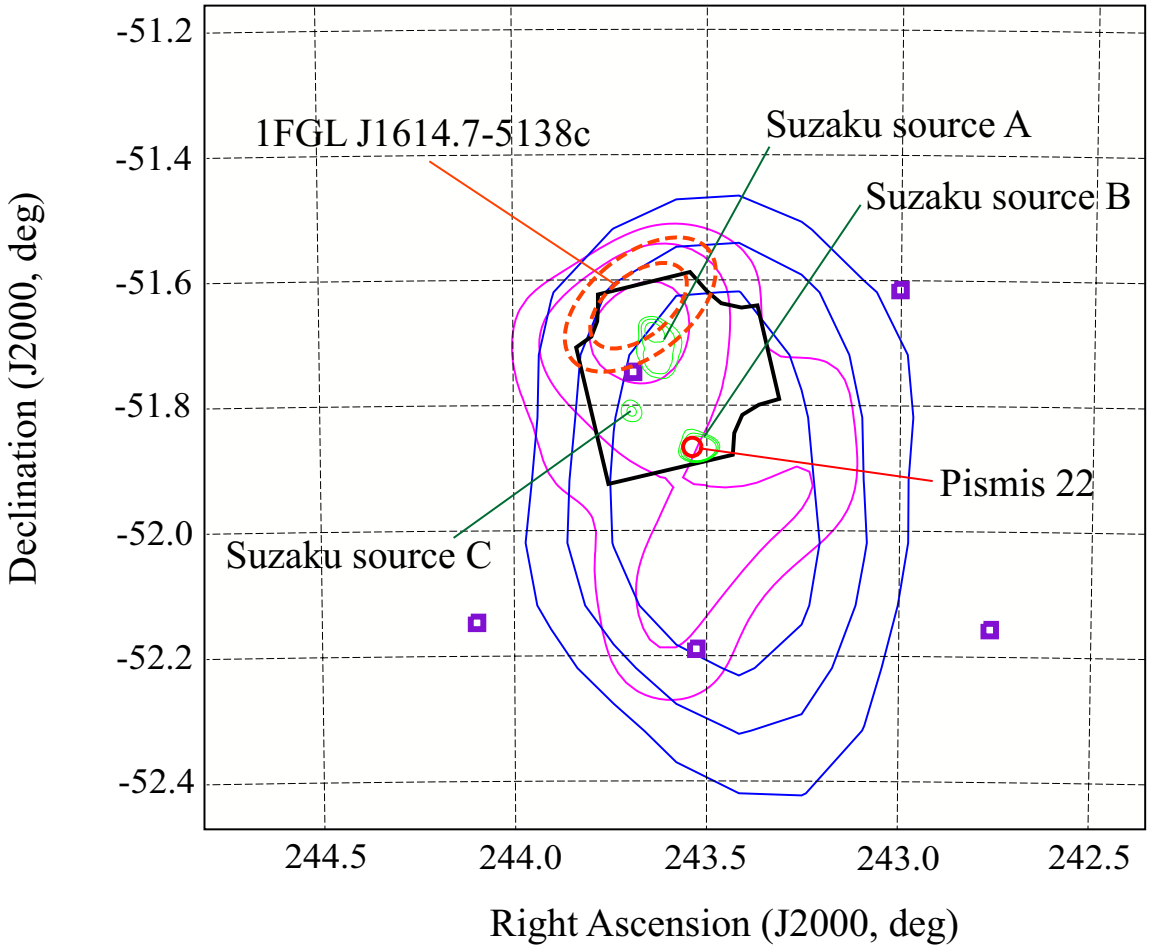

Figure 6.1 Morphological relationship between the X-ray and gamma-ray observations. Blue, magenta, and green contours show the emission regions of CANGAROO-III, H.E.S.S., and *Suzaku*, respectively. Orange dashed circles show the 68% and 90% error ellipses of the position of the *Fermi* source. The red circle shows the Pismis 22 position and purple squares show the positions of nearby pulsars (Manchester et al., 2005; ATNF Pulsar Catalogue ver.1.38). The bold black line shows the observed region by the *Suzaku* XIS in Matsumoto et al. (2008) excluding the calibration source region on the corners.

6.1.1 Leptonic Model

First I examine a leptonic model to explain the observed SED. For the X-ray spectrum, I use the *Suzaku* spectrum of Suzaku source A observed around the VHE gamma-ray peak position, with a statistical error at the 90% confidence level. For the *Fermi* spectrum, I used a 2σ statistical error and systematic errors of 1.8σ in the flux and 1.2σ in the photon index (Abdo et al., 2010a). Here I assumed a single power-law with an exponential cutoff electron spectrum,

$$dN_e/dE_e = K_e E_e^{-\Gamma_e} \exp(-E_e/E_{max\_e}), \tag{6.1}$$

where K_e is the normalization factor, E_e is the electron energy, Γ_e is the spectral index of the electrons, and E_{max_e} is the maximum accelerated electron energy. The single power-law spectrum was derived from the Fermi acceleration mechanism as discussed in Chapter 2. Figure 6.2 shows the model curves for HESS J1614−518. Here I calculated the inverse Compton model curves. To calculate the IC radiation, the amount of the seed photon at the emission region is needed. As a seed photon flux, I used cosmic-ray microwave background and an interstellar radiation field (ISRF) derived from the GALPROP package (v50p) (Porter & Strong, 2005; Strong & Moskalenko, 2006). The estimated photon field is shown in Fig.6.3 for the distance of 10 kpc. Energy densities of 1.4 eV cm^{-3} and 5.5 eV cm^{-3} for IR and optical light were obtained, respectively. In addition, this radiation field changed by less than an order of magnitude when I varied the distance from 1 kpc to 10 kpc, with values in the range from 0.9 to 1.7 eV cm^{-3} and 1.1 to 5.5 eV cm^{-3} for IR and and optical light, respectively. I fixed the power-law index to $\Gamma_e = 2.0$ and fitted the VHE gamma-ray spectrum by the IC emission. By fitting the TeV spectrum, the maximum energy and total energy of the electrons were obtained to be 4.2±1.5 TeV and $1.9 \times 10^{49} \times (d/10\mathrm{kpc})^2$ ergs, respectively. Since the total energy of the accelerated electrons was only ∼1% for a typical supernova explosion kinetic energy of $\sim 10^{51}$ ergs, this scenario was acceptable from the point of energetic aspect. Next, the synchrotron emission from this electron spectrum was calculated. Figure 6.4 shows the synchrotron model curve for different magnetic fields. From Eq.2.53, the ratio of the synchrotron flux to the IC flux is proportional to the energy density of the magnetic field. Thus, from comparison between the synchrotron model and the *Spitzer* upper limit, an upper limit of a magnetic field is determined to be 6 μG.

The harder and fainter spectrum in the X-ray band compared to the VHE gamma-ray spectrum cannot be explained based on the synchrotron and IC emission.

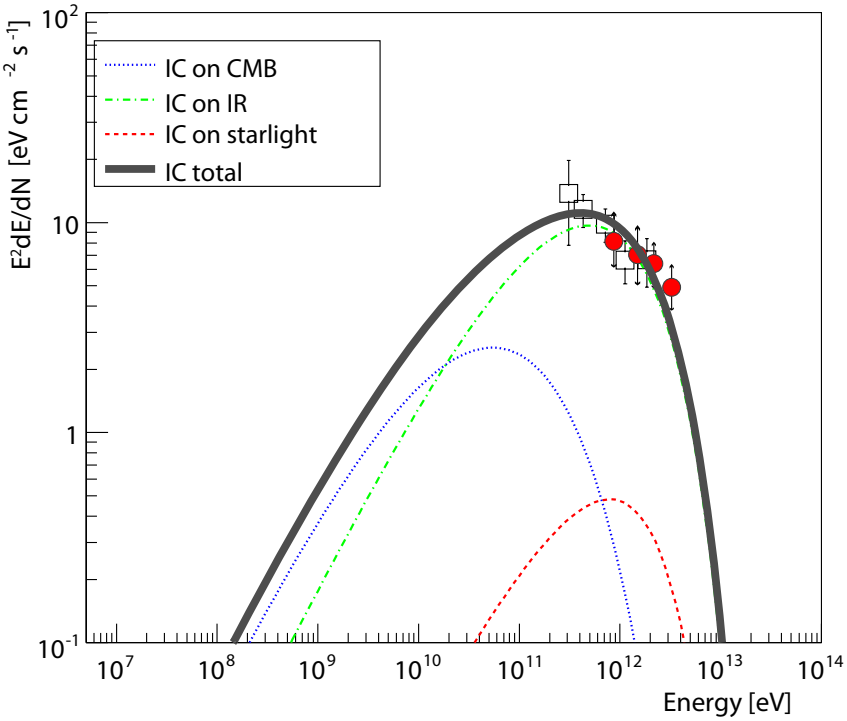

Figure 6.2 The IC emission curves for HESS J1614−518. The electron distribution was determined by fitting the IC emission to TeV spectrum. The IC emissions for different seed photon components were also shown.

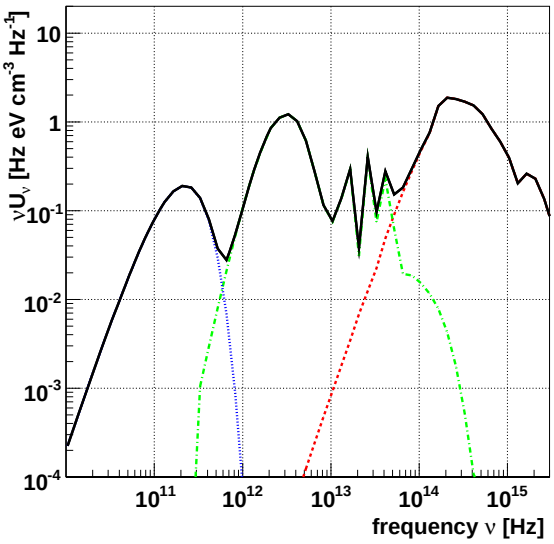

Figure 6.3 Interstellar radiation field from the GALPROP at HESS J1614−514 region with a distance of 10 kpc. CMB (dotted), IR emission from interstellar dust (dot-dashed), and optical photons from stars (dashed) are shown. The bold solid line represents the sum of the three components.

There is also the possibility that Bremsstrahlung produces both the X-ray and VHE gamma-ray emission (Uchiyama et al., 2002), as shown in Fig. 6.5. To assume that the TeV spectrum was originated from only Bremsstrahlung not from IC emission, I used the electron spectrum of 10 % of that obtained by IC fitting. This model gives a good reproduction when an ambient matter density n_p of 600 $p\,\mathrm{cm}^{-3}$ is assumed. I estimated an ambient matter density from the velocity-integrated data of the CO survey (Dame et al., 2001) to be ∼80 or 8 $p\,\mathrm{cm}^{-3}$ for 10 kpc and 1 kpc, respectively. Thus, the Bremsstrahlung model that requires an ambient matter density of 600 $p\,\mathrm{cm}^{-3}$ was rejected. Additionally, there is difficulty in explaining the morphological difference between the X-ray and the VHE gamma-ray emission because it requires an unlike situation in which the relatively high energy (multi-TeV) electrons responsible for the VHE gamma-ray emission has to be extended more widely than the relatively low energy (multi-keV) electrons which are responsible for the X-ray emission.

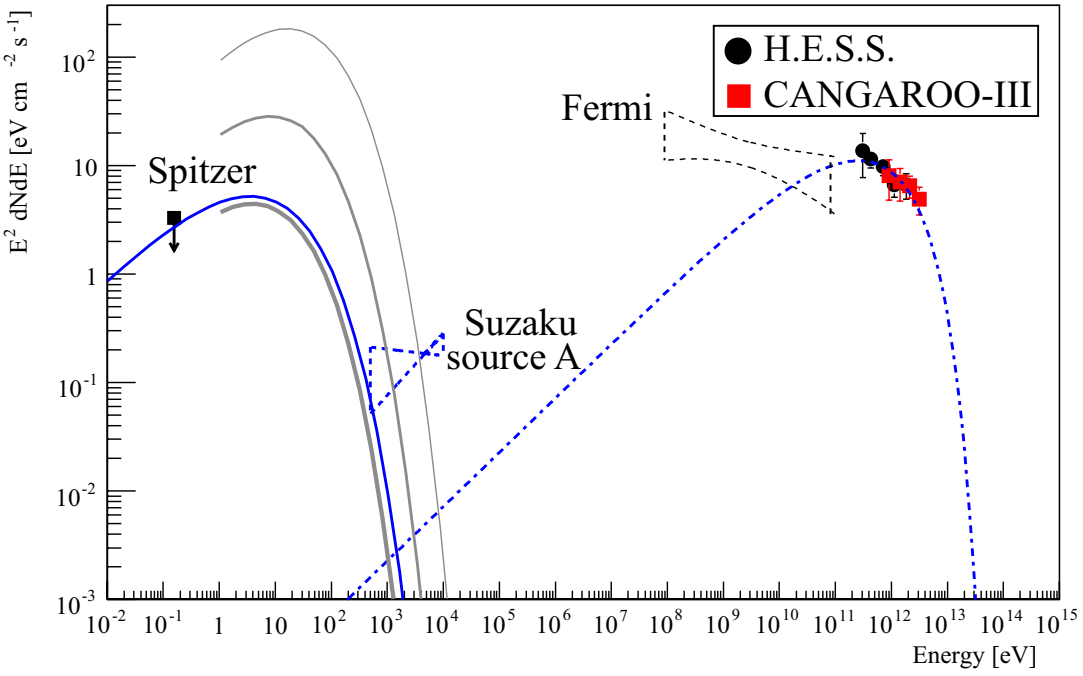

Figure 6.4 SED with leptonic model curves for HESS J1614−518. The dash-dotted and solid blue lines show IC and synchrotron emission derived from the single power-law electron spectrum with an exponential cutoff to fit the VHE emission, respectively. The thick, regular, and thin gray lines show synchrotron emission with different magnetic fields of 5 μG, 10 μG, and 100 μG, respectively.

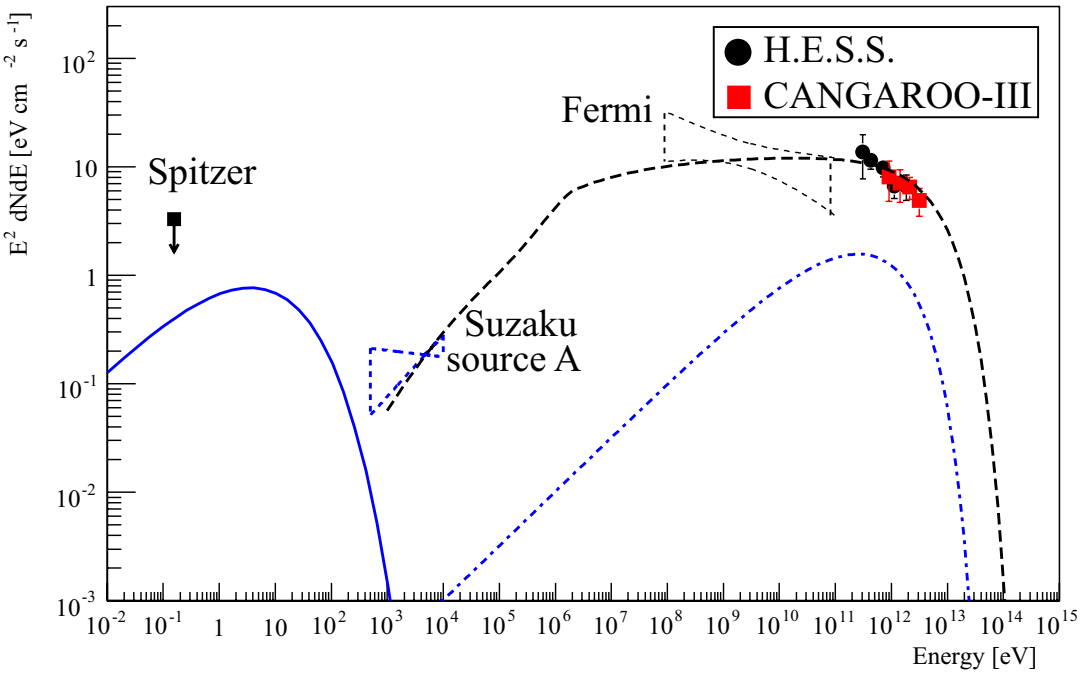

Figure 6.5 The Bremsstrahlung curves for HESS J1614−518. The dashed black line shows a Bremsstrahlung curve for a number density of ambient matter of 600 p cm^{-3}.

6.1.2 Hadronic Model

Second, I examined a neutral-pion decay model. Based on a model proposed by Yamazaki et al. (2006), only nucleonic particles remain in an old SNR with an age of $\sim 10^5$ yr, while primary electrons have already lost most of their energy by the synchrotron cooling. This model naturally explains the difference of the emission size between X-ray and VHE gamma-ray. Figure 6.6 shows the SED with the assumption that the population of accelerated protons can be expressed by a single power-law with an exponential cutoff,

$$dN_p/dE_p = K_p E_p^{-\Gamma_p} \exp(-E_p/E_{max\_p}). \tag{6.2}$$

I set the power-law index to $\Gamma_p = 2.0$. The best-fit cutoff energy was obtained to be $E_{max\_p} = 36 \pm 18$ TeV. The total energy of high energy protons was calculated to be $W_p = 1.2 \times 10^{52} (n_p/1\ p\ \mathrm{cm}^{-3})^{-1} (\mathrm{d}/10\mathrm{kpc})^2$ ergs. By setting $n_p = 100\ p$ cm^{-3}, the efficiency of energy conversion to accelerate protons is 10% for a typical total supernova explosion kinetic energy of $\sim 10^{51}$ ergs. As described above, no obvious molecular cloud was found in the NANTEN ^{12}CO(J=1-0) survey data. In addition, an ambient matter density from the velocity-integrated data of the CO survey (Dame et al., 2000) was estimated to be

$\sim$80 and 8 p cm^{-3} for 10 kpc and 1 kpc, respectively. Thus, an assumption of 100 p cm^{-3} is likely for 10 kpc, but not for 1 kpc. Further observations to determine the ambient matter density are necessary to investigate the validity for such assumed density.

Next, I discuss a ratio between the accelerated protons and primary electrons. Assuming the spectral index, $\Gamma_p = \Gamma_e = 2.0$, the maximum energy of primary electrons is determined so as to be $E_{max\_e} \leq E_{max\_p}$. The turnover energy of synchrotron emission is determined as,

$$E_{turn} = 22 \text{ keV } \times (E_{max\_e}/50 \text{ TeV})^2 \times (B/200\mu\text{G}). \tag{6.3}$$

Then, the hard index of the X-ray spectrum of this source requires $E_{turn} \geq 10$ keV, and a corresponding lower limit for the magnetic field of $B \geq$200 μG was determined from this equation with $Emax\_e = 36$ TeV. The electron spectrum was determined by fitting X-ray emission assuming $E_{max\_e} = 36$ TeV and B =200 μG The model curve for this lower limit condition was shown in Fig.6.6. The number ratio of protons to primary electrons is obtained to be,

$$K_{pe} = K_p/K_e \geq 2.1 \times 10^5 (n_p/1 \ p \text{ cm}^{-3})^{-1}. \tag{6.4}$$

Setting the value of $n_p = 100$ p cm^{-3}, K_{pe} is obtained to be 2.1×10^3. This value is slightly larger than that of the observed average cosmic-rays around the earth of 10^3 at $\sim$1 TeV.

I also calculated the contribution of emissions from secondary electrons from p-p interactions using the same proton spectrum as above and the ambient matter density of $100\,p\,\text{cm}^{-3}$. I followed the calculation in Kelner & Aharonian (2008) to derive the spectrum of the secondary electrons. Assuming a distance of 10 kpc from the Earth, the distance between Suzaku source A and source B was calculated to be 35 pc. Thus, I assumed that the radius of the SNR is 35 pc and roughly estimated the age of the SNR using the equation (2) in Yamazaki et al. (2006) to be 3×10^4 yr, assuming the initial shock velocity of 10^9 cm s^{-1}. Thus, the emissions from the secondary electrons were derived by assuming continuous injection of electrons produced by a constant proton spectrum over 3×10^4 yr with a magnetic field of 200 μG (Atoyan & Aharonian, 1999). The obtained synchrotron curve is shown in Fig.6.6. The obtained inverse Compton and Bremsstrahlung emissions were able to be neglected since the number of electrons is insufficiently small. Since the synchrotron emission from the secondary electrons was not able to explain the X-ray emission, the X-ray emission might originate in the synchrotron emission from the

primary electrons, as shown in Fig.6.6, or other emission mechanisms. Since the synchrotron emission from the secondary electrons dominates below the infrared band, the detection of the emission in the radio to infrared bands could support the hypothesis that the VHE gamma-ray emission is produced by the neutral-pion decay. Because the *Spitzer* upper limit was above the predicted flux of synchrotron emission due to the secondary electrons, more detailed observations with higher sensitivity are needed.

Next, I discussed the possible association between the SNR and Pismis 22. To discuss the association, I estimated the SNR age using the distance to Pismis 22 with the assumption that a supernova explosion occurred at the position of Pismis 22 and the shock front has now reached at the VHE gamma-ray peak position. By using the same equation (2) in Yamazaki et al. (2006), the age was obtained to be 3×10^2 yr for a distance of 1 kpc. Since the lower limit of a magnetic field was obtained to be $B \geq$200 μG as above, the synchrotron cooling time of 100 TeV electrons decreased to 1 yr. For a distance of 1 kpc, the required total energy of protons W_p could be reduced if the number density of ambient matter n_p is the same as for a distance of 10 kpc. If the total energy of protons W_p is fixed to be 10^{50} ergs, the required density of ambient matter is reduced to $n_p = 1\ p\ \mathrm{cm}^{-3}$ for a distance of 1 kpc. This value was comparable with the typical number density in the interstellar field and does not contradict the fact that no obvious molecular cloud was found in the NANTEN ^{12}CO(J=1-0) survey data. The contribution of emissions from secondary electrons was shown in Fig.6.6 as red lines, assuming the injection time of 3×10^2 yr with a magnetic field of 200 μG. The synchrotron emission from the secondary electrons was not able to explain the X-ray spectrum of Suzaku source A. The X-ray emission might originate in the synchrotron emission from the primary electrons, or other emission mechanisms. Since the flux of synchrotron emission from the secondary electrons in the radio to infrared bands was lower than that of the case of a distance of 10 kpc, as shown in Fig.6.6, a determination of the spectrum below the infrared band is a key to reveal the origin of the SNR. Additionally, an observation of thin thermal plasma in the X-ray band by such as the micro-calorimeter onboard Astro-H will provide useful information such as plasma temperature or chemical abundances. For example, the detection of high abundance of α-elements (O, Mg, Si, S, Ca, and Ti) compared to that of iron, which is expected in a massive star explosion (Kobayashi et al., 2006), may support the SNR scenario. In fact, a recent *Suzaku* observation of the open cluster Westerlund 2 detected metal-rich thermal emission, suggesting that the diffuse X-ray and VHE gamma-ray emission may have originated from a hypernova remnant (Fujita et al., 2009).

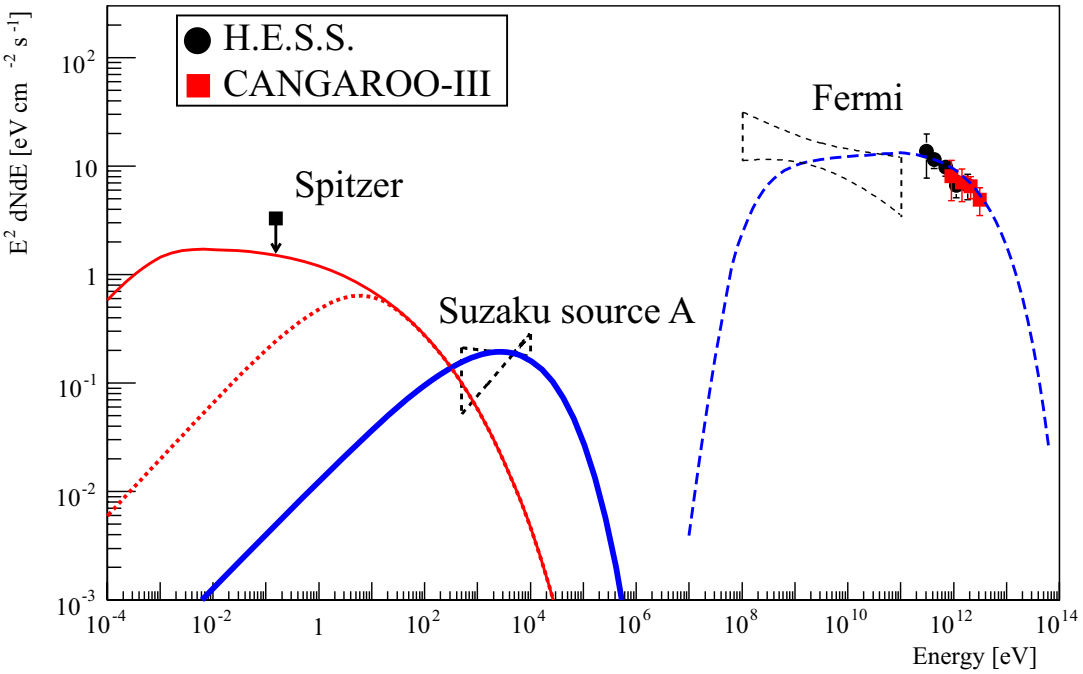

Figure 6.6 SED and the model curve for neutral pion decay (blue dashed line). The blue bold-solid line shows the synchrotron model curve for the primary electrons. The red solid and dotted lines show synchrotron model curves for the secondary electrons for a distance of 10 kpc and 1 kpc, respectively.

6.2 Stellar wind from massive stars scenario

The VHE gamma-ray emission might have been produced by hadrons accelerated in winds from massive stars in Pismis 22 (Voelk & Forman, 1982; Bednarek, 2007). A fraction of the stellar wind energy can be transferred to relativistic particles. Assuming that the shock acceleration generates a single power-law spectrum of primary particles, we can apply the discussion made in the SNR scenario. I discuss the energetics for the hadronic origin here to produce the observed gamma-ray emission. A single O-type star loses mass at a rate of $\dot{M} = 10^{-6} M_{\odot}$ per year with a stellar wind velocity of ~ 1500 km s^{-1} (Castor et al., 1975). The rate of kinetic energy emitted from the single star is 7×10^{35} erg s^{-1}. If I assume an energy conversion efficiency to particle acceleration of 5 %, which is the maximum efficiency adopted for a hadronic model in Bednarek (2007), an ambient matter density of 100 p cm^{-3}, a distance of 1 kpc, and an age of 40 Myr, two O-type stars are required in Pismis 22 to produce the observed VHE gamma-ray spectrum in the hadronic scenario. However, no obvious molecular cloud has been found at this distance in the NANTEN data, as described above. Thus, the scenario of the stellar wind origin is rejected.

6.3 PWN Scenario

PWNe are the largest class of identified Galactic VHE gamma-ray sources. I discuss the possibility of HESS J1614−518 being a PWN in this section.

Generally, a ratio of a TeV gamma-ray flux to a X-ray flux, $F_{\rm TeV}/F_{\rm X}$ is inversely proportional to a squared magnetic field when the high energy electrons emit both TeV gamma-rays and X-rays as described in Chapter 2. To explain the large flux ratio of the TeV gamma-ray flux to the X-ray flux, an extremely low magnetic field lower than the interstellar magnetic field of 1 μG is required, which is not acceptable. Then, I used the time-evolving electron injection model as described in Chapter 2. The population of electrons with an energy of $\sim$1 TeV is sufficiently large to produce the relatively high flux of VHE gamma rays through IC process, since they have been less cooled by the synchrotron radiation and most of them are produced by an early stage of the pulsar life, the young and powerful pulsar. On the other hand, the population of electrons with energy of $\sim$100 TeV which dominantly radiate X-rays is relatively small, since they have been cooled by the synchrotron radiation and only electrons which were recently produced

were able to survive.

I applied this model to HESS J1614−518 as following the calculation in Higashi et al. (2008). All the nearby pulsars are shown in Fig.6.1. First, I applied the model to the nearest pulsar PSR J1614−5144. The distance to the pulsar was measured to be 9.6 kpc which was consistent with the distance to Suzaku source A. The parameters of this pulsar are summarized in Table 6.1. Since the braking index of this pulsar was unknown, I used the value of 2.5 which is the value of Crab pulsar. Even if the measured braking indices of other pulsars falling in the range from 1.4 to 3 (Livingstone et al., 2006) were applied, the following results do not change significantly. I calculated both the synchrotron and IC radiation to reproduce the observed X-ray and VHE gamma-ray fluxes, assuming a single power-law electron spectrum with an exponential cutoff. Figure 6.7 shows the model curves to reproduce the SED with a magnetic field of 8 μG, an initial spin-down timescale $\tau_0 = 3.0 \times 10^4$ yr, and a power-law index of electrons of 2.0. The obtained total energy of electrons was estimated to be $E_{tot} = 3.8 \times 10^{49}$ ergs. However, considering the total spin-down energy of the pulsar over its age, $E_{pulsar} = 3.4 \times 10^{48}$ ergs, this pulsar never supply such a huge energy to the electrons. Thus, PSR J1614−514 is rejected as an associated pulsar. I applied this discussion to the rest of the nearby pulsars. The comparison between calculated E_{tot} and E_{pulsar} are shown in Table 6.1. All the pulsars are not sufficient to produce the observed flux. Thus, none of already known pulsars can be associated with HESS J1614−518.

There is also the possibility that an undiscovered pulsar having an enough spin-down power to explain the observed gamma-ray luminosity might be located in the vicinity of Suzaku source A or source B. I estimated the pulsar age to be 24 kyr and 23 kyr for Suzaku source A and B, respectively, using the correlation between pulsar age and the ratio of gamma-ray flux to X-ray flux (Mattana et al., 2009). Although the time-evolve model can explain the large ratio between the X-ray and TeV gamma-ray fluxes as above discussion, the model showed a very large discrepancy with the sub-GeV flux observed with *Fermi*, the model curve is 30 times larger than the observed flux at 0.1 GeV. Thus, the time-evolving electron injection model with a single power-law electron distribution was rejected. The MeV/GeV component might arise from the different mechanism than the TeV emission.

Although the present sensitivity in the radio band may not be sufficient to detect this unknown pulsar, further observations in the GeV band could detect a radio quiet pulsar like Geminga, which was detected with *CGRO* EGRET (Bertsch et al., 1992), or

Table 6.1. Pulsars near HESS J1614−518.

PSR	d [kpc]	$\dot{E}$[a][ergs s^{-1}]	age[b][yr]	$E_{\rm pulsar}$[c][ergs]	offset[d][arcmin]	E_{tot}[e][ergs]
J1611−5209	3.3	3.4×10^{34}	5.6×10^{5}	7.6×10^{47}	36	7.0×10^{47}
J1612−5136	18.2	1.3×10^{33}	2.0×10^{6}	1.0×10^{47}	24	2.1×10^{50}
J1613−5211	6.1	7.9×10^{33}	3.8×10^{5}	1.2×10^{47}	23	1.5×10^{49}
J1614−5144	9.6	8.1×10^{31}	3.3×10^{6}	1.1×10^{46}	6.4	3.7×10^{49}
J1616−5208	7.4	1.1×10^{33}	5.6×10^{5}	2.5×10^{46}	28	2.2×10^{49}

[a]observed current spin down energy.

[b]obtained from $P/(2\dot{P})$ where P is a period of pulsar and $\dot{P}$ is a time derivative of the period.

[c]derived under the assumption of n =2.5.

[d]from the center position of HESS J1614−518.

[e]total energy of electrons to reproduce the SED.

sixteen previously unknown pulsars which were recently discovered with *Fermi* (Abdo et al., 2009). In addition, future deep X-ray observations could detect pulsed emission from Suzaku source A or source B. Given these detections, emission models for PWNe (e.g., Abdo et al., 2010b; Tanaka & Takahara, 2010; Slane et al., 2010; Bucciantini et al., 2010), using a broken power-law distribution of electrons, might be able to reveal that the VHE gamma-ray emission of this unidentified source originates from a PWN.

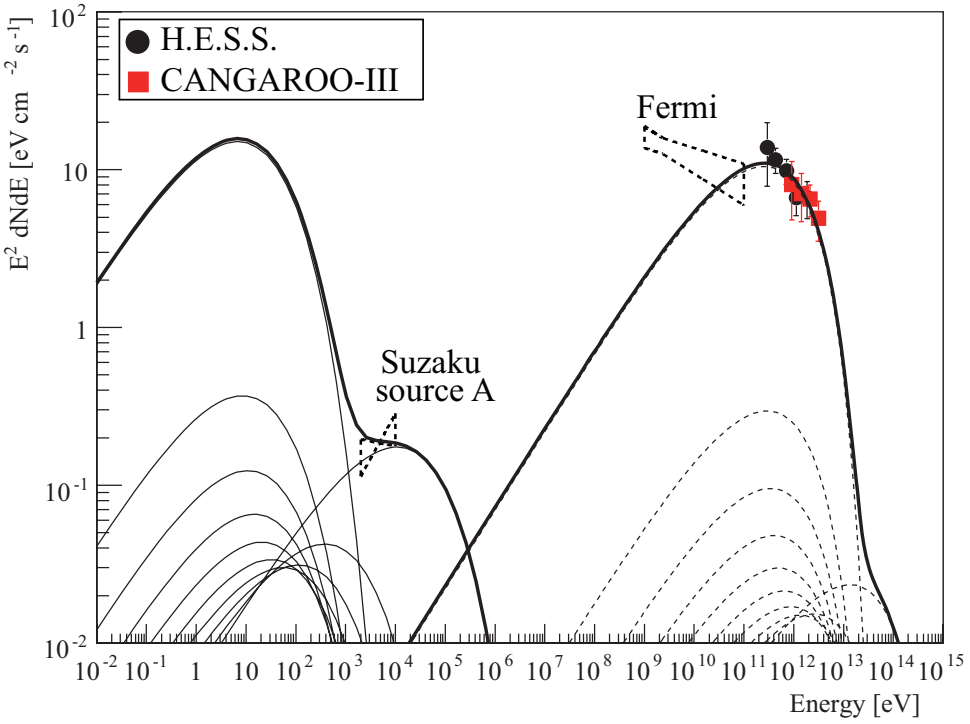

Figure 6.7 SED with a time-evolving leptonic model curves for PSR J1614−5144. The thin solid and dotted lines show the synchrotron and IC component derived from the evolving electron per 3.3×10^5 yr ($0 < t < 3.3 \times 10^6$ yr), respectively. The bold solid lines show their total.

Chapter 7

Conclusion

We observed the VHE gamma-ray unidentified source HESS J1614−518 using CANGAROO-III. The observation was carried out from May to August in 2008, and obtained the data with livetime of 53.6 hr. After the gamma-ray selection using the Fisher discriminant method, we obtained 950 ± 107 gamma-ray events above 760 GeV. The differential energy spectrum was a single power law:$(8.2 \pm 2.2_{stat} \pm 2.5_{sys}) \times 10^{-12} \times (E/1\mathrm{TeV})^{-\gamma}$ $\mathrm{cm}^{-2}\mathrm{s}^{-1}\mathrm{TeV}^{-1}$ with a photon index γ of $2.4 \pm 0.3_{stat} \pm 0.2_{sys}$. The spectrum and size of the emission region were consistent with H.E.S.S. result, and our data reconfirmed the diffuse TeV gamma-ray emission from HESS J1614−518.

I discussed the possible counterparts for this object using the results of observations with *Suzaku* and *Fermi*.

For the SNR scenario, a one-zone leptonic model was not able to account for the observed SED. Hadronic models gave a good reproduction of the SED and the typical SNR explosion energy of $\sim 10^{51}$ ergs is able to supply the total energy of protons. Since the required number densities of the ambient matter were $n_p = 1\ p\ \mathrm{cm}^{-3}$ and $n_p = 100\ p\ \mathrm{cm}^{-3}$ for a distance to the SNR of 1 kpc and 10 kpc, respectively, detailed molecular observations could determine whether the SNR originated from Pismis 22 (d$\sim$1 kpc) or a farther distance around 10 kpc. As there were also differences in the spectrum of the emission from the secondary electrons, a determination of the spectrum below the infrared band would help determine the likelihood of an SNR origin.

For the PWN scenario, the nearby known pulsars are not responsible since the spin-down powers are insufficient to produce the observed TeV gamma-ray luminosity. Further observations to search a pulsar are necessary to investigate the PWN scenario.

For the stellar wind scenario, Pismis 22 was required to contain two O-type stars

through its entire age from energetics considerations. However, the required number density of the ambient matter of $n_p = 100\ p\ \mathrm{cm}^{-3}$ may not be consistent with the results of the NANTEN observations.

To identify HESS J1614−518, more detailed multi-wavelength observations are required. To discuss the stellar wind origin in more detail, a determination of the number of OB stars is necessary. For the SNR scenario, the ultra-high energy resolution in X-ray of the SXS onboard *Astro-H* could detect line emissions with a high abundance of α-elements compared to that of iron, which would indicate that HESS J1614−518 is an SNR. The detection of the synchrotron emission of the secondary electrons by radio to optical band will be a strong evidence of the cosmic-ray acceleration. To show that the Suzaku source B is an AXP, supporting the SNR or PWN scenario, a high time-resolution X-ray observation is needed to detect a pulsed signal from the source. More detailed gamma-ray spectroscopy with *Fermi*, and the Cherenkov Telescope Array (CTA, 2010) could determine the origin of the accelerated particles. For example, the expected sensitivity and angular resolution of CTA are ten and several times better than those of current IACTs, respectively. This high performance will provide such as space distributions of power-law index which help to determine the distributions of accelerated particles, which will lead to the determination of the emission mechanism.

Appendix A

Hillas parameters

Hillas parameters are commonly used image analysis of IACTs. Provided ith hit pixel at (x_i, y_i) contains signal amplitude of s_i, fundamental statistical parameters are definded:

$$\langle x \rangle = \frac{\sum x_i s_i}{\sum s_i}, \quad \langle y \rangle = \frac{\sum y_i s_i}{\sum s_i} \tag{A.1}$$

$$\langle x^2 \rangle = \frac{\sum x_i^2 s_i}{\sum s_i}, \quad \langle y^2 \rangle = \frac{\sum y_i^2 s_i}{\sum s_i}, \quad \langle xy \rangle = \frac{\sum x_i y_i s_i}{\sum s_i} \tag{A.2}$$

$$\sigma_x = \langle x^2 \rangle - \langle x \rangle^2, \quad \sigma_y = \langle y^2 \rangle - \langle y \rangle^2, \quad \sigma_{xy} = \langle xy \rangle - \langle x \rangle \langle y \rangle \tag{A.3}$$

A major axis of a image is defined by minimizing the deviation of the image. Using transformation of

$$\begin{pmatrix} x' \\ y' \end{pmatrix} = \begin{pmatrix} \cos\theta & -\sin\theta \\ \sin\theta & \cos\theta \end{pmatrix} \begin{pmatrix} x \\ y \end{pmatrix}, \tag{A.4}$$

then

$$\sigma_{x'} = \langle x^2 \rangle - \langle x \rangle^2 \tag{A.5}$$

$$= \cos^2\theta \langle x^2 \rangle - 2\cos\theta \sin\theta \langle xy \rangle + \sin^2\theta \langle y^2 \rangle \tag{A.6}$$

$$\sigma_{y'} = \sin^2\theta \langle x^2 \rangle + 2\cos\theta \sin\theta \langle xy \rangle + \cos^2\theta \langle y^2 \rangle \tag{A.7}$$

are calculated. By differenciating these formula, θ is to be obtained:

$$\sin 2\theta (\langle x^2 \rangle - \langle y^2 \rangle) + 2\cos 2\theta \langle xy \rangle = 0 \tag{A.8}$$

$$\theta = \frac{1}{2} \left(\tan^{-1} \frac{\langle xy \rangle}{\langle y^2 \rangle - \langle y \rangle^2} \right). \tag{A.9}$$

Thus

$$\cos 2\theta = \frac{\sigma_y^2 - \sigma_x^2}{\sqrt{(\sigma_y^2 - \sigma_x^2)^2 + 4\sigma_{xy}^2}} = \frac{d}{z} \tag{A.10}$$

$$= \frac{2\sigma_{xy}}{\sqrt{(\sigma_y^2 - \sigma_x^2)^2 + 4\sigma_{xy}^2}} = \frac{2\sigma_{xy}}{z} \tag{A.11}$$

$$\tag{A.12}$$

where $d \equiv \sigma_y^2 - \sigma_x^2$ and $z \equiv \sqrt{d^2 + 4\sigma_{xy}^2}$. Then Hillas parameters are:

$$WIDTH = \sqrt{\frac{\sigma_x + \sigma_y - z}{2}} \tag{A.13}$$

$$LENGTH = \sqrt{\frac{\sigma_x + \sigma_y + z}{2}} \tag{A.14}$$

$$DISTANCE = \sqrt{(\langle x \rangle - x_s)^2 + (\langle y \rangle - y_s)^2} \tag{A.15}$$

where (x_s, y_s) represents posision of the target.

Appendix B

statistical significance

Li & Ma (1983) proposed the statistical methodology for evaluating the reliability of the statistical significance of the gamma-ray signal over the background events, which has been widely accepted in VHE gamma-ray experiments. In general, provided that we pointed the telescopes to the target, for a time of $t_{\rm on}$ and detected $N_{\rm on}$ gamma-ray like events, and that $t_{\rm off}$ and $N_{\rm off}$ for background observation, a parameter α is defined as $\alpha = t_{\rm on}/t_{\rm off}$. Then the number of background events included in $N_{\rm on}$ is estimated as

$$N_{\rm B} = \alpha N_{\rm off}. \tag{B.1}$$

Therefore the number of gamma-ray events, $N_{\rm S}$ is

$$N_{\rm S} = N_{\rm on} - N_{\rm B} = N_{\rm on} - \alpha N_{\rm off} \tag{B.2}$$

Since $N_{\rm on}$ and $N_{\rm off}$ are independent measurements, the variance of $N_{\rm S}$ is calculated as

$$\sigma^2_{N_{\rm S}} = \sigma^2_{N_{\rm on}} + \alpha^2 \sigma^2_{\rm N_{off}}, \tag{B.3}$$

using the error propagation formula. Then the significance S is defined with the standard deviation of $N_{\rm S}$:

$$S = \frac{N_{\rm S}}{\sigma_{N_{\rm S}}} = \frac{N_{\rm on} - \alpha N_{\rm off}}{\sqrt{N_{\rm on} + \alpha^2 N_{\rm off}}}. \tag{B.4}$$

The formula above is simply derived from the Poisson law of $N_{\rm on}$ and $N_{\rm off}$. Li & Ma (1983),however, presented the discrepancies between the distribution of the significances computed by the Monte-Carlo simulation and the expected normal distribution in the case of $\alpha \neq 1$, and then they suggested further improvement of the estimation of the standard deviation of $N_{\rm S}$.

When we estimate the probability that the observed signal was due only to the background, it should be assumed that all the observed signal, not only $N_{\rm on}$ but also $N_{\rm off}$, were derived from the background. Under the assumption, $N_{\rm on}$ would follow the Poisson distribution with expected count of $\langle N_B \rangle$ and $N_{\rm off}$ with $\langle N_B \rangle / \alpha$. Then Eq. B.3 is written as

$$\sigma^2_{N_{\rm S}} = \sigma^2_{N_{\rm on}} + \alpha^2 \sigma_{N_{\rm off}} = (1+\alpha)\langle N_B \rangle. \tag{B.5}$$

Here $\langle N_B \rangle$ is obtained more accurately than Eq. B.1:

$$\langle N_B \rangle = \frac{N_{\rm on} + N_{\rm off}}{t_{\rm on} + t_{\rm off}} t_{\rm on} = \frac{\alpha}{1+\alpha}(N_{\rm on} + N_{\rm off}). \tag{B.6}$$

Then the estimation of the standard deviation of N_S is derived from above two equations as

$$\sigma_{N_{\rm S}} = \sqrt{(1+\alpha)\langle N_B \rangle} = \sqrt{\alpha(N_{\rm on} + N_{\rm off}}, \tag{B.7}$$

which yeilds the significance

$$S = \frac{N_{\rm on} - \alpha N_{\rm off}}{\sqrt{\alpha(N_{\rm on} + N_{\rm off})}}. \tag{B.8}$$

Li & Ma (1983) also showed Eq. B.8 underestimated the significance for $\alpha < 1$ and overestimated for $\alpha > 1$.

They suggested another method of estimating the siginificance by using the method of hypotheses test in mathematical statistics. Here we treat two unknown parameters, the expected number of source photons $\langle N_S \rangle$ and the background $\langle N_B \rangle$, and "null hypothesis" puts $\langle N_S \rangle = 0$. If the null hypothesis is true, the significance is calculated to

$$S = \sqrt{-2 \ln \lambda}, \tag{B.9}$$

where λ is the maximum likelihood ratio:

$$\lambda = \left[\frac{\alpha}{1+\alpha} \left(\frac{N_{\rm on} + N_{\rm off}}{N_{\rm on}} \right) \right]^{N_{\rm on}} \left[\frac{1}{1+\alpha} \left(\frac{N_{\rm on} + N_{\rm off}}{N_{\rm off}} \right) \right]^{N_{\rm off}}. \tag{B.10}$$

Fig. B.1 shows the comparison of the probability derived from Eq. B.4, Eq. B.8, Eq. B.9 and the standard normal distribution for $\alpha < 1$ and $\alpha > 1$(Li & Ma, 1983). Eq. B.9 gave the most consistent result with the Gaussian, which we adopted in this thesis.

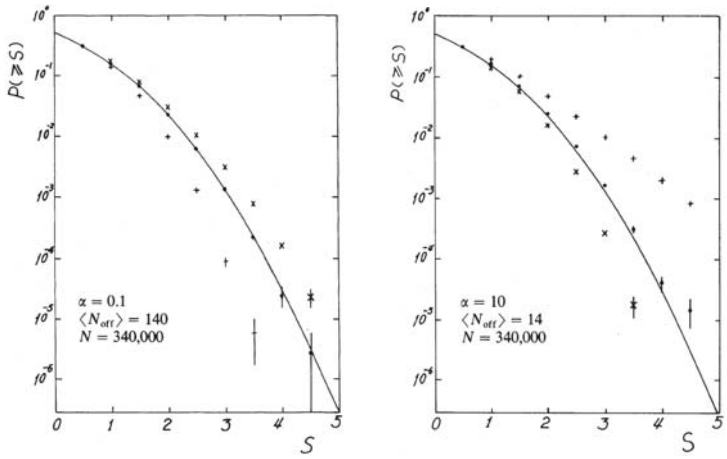

Figure B.1 Integral frequency distributions of the significance of the Monte-Carlo samples(Li & Ma, 1983). Solid line represents the Gaussian distribution. Eq. B.4, Eq. B.8 and Eq. B.9 are represented by pulses, crosses and filled circles, respectively.

Appendix C

Spindown luminosity and magnetic field of pulsar

A pulsar is generally approximated as a magnetic dipole. Since the magnetic dipole is inclined from the rotation axis, the magnetic dipole moment shows a periodic variation at a large distance. Therefore the electromagnetic radiation is observed, and the pulsar loose its energy through the radiation.

The energy loss of magnetic dipole radiation is

$$-\frac{dE_{\rm rad}}{dt} = \frac{B^2 R^6 \Omega^4 \sin^2\alpha}{6c^3}, \tag{C.1}$$

where B and R are a radius and a surface magnetic field of the pulsar, respectively, α is an angle between the rotation and magnetic axis. On the other hand, we can estimate the energy loss in the rotational energy E_{rot} as follows,

$$E_{\rm rot} = \frac{1}{2} I \Omega^2 \tag{C.2}$$

yields

$$-\frac{dE_{\rm rot}}{dt} = -I\Omega\dot{\Omega}, \tag{C.3}$$

which is called the spindown luminosity. From Eqs.C.1 and C.3, we can derive the surface magnetic field by assuming $dE_{\rm rad}/dt = dE_{\rm rot}/dt$,

$$B = 3.1 \times 10^{19} \sqrt{P\dot{P}}\ \ {\rm G}, \tag{C.4}$$

with $R = 10$ km, $I = 10^{45}$ g cm^2 and $\alpha = 30^\circ$, typically 10^{12} G ($P \sim 1$ sec and $\dot{P} \sim 10^{-15}$).

Appendix D

Braking index and characteristic age of pulsar

It is generally believed the "spindown law" of the time evolution of its angular velocity:

$$\dot{\Omega} = -k\Omega^n, \tag{D.1}$$

where k and n are constants and the latter is called a braking index. By integrating Eq. D.1, we can calculate the age of the pulsar τ as,

$$\tau = -\frac{P}{(n-1)\dot{P}}\left(1 - \left(\frac{P_0}{P}\right)^{n-1}\right), \tag{D.2}$$

in which P_0 represents the (unknown) initial period of the pulsar. Assuming $n \neq 1$ and $P \ll P_0$, the approximation yields the characteristic age τ_c as

$$\tau_c = -\frac{1}{n-1}\frac{P}{\dot{P}}. \tag{D.3}$$

For the magnetic dipole braking, the braking index turns to be -3. Differentiation of Eq. D.1 shows the braking index is directly derived from the measurement if the second differential of the period is provided:

$$n = \frac{\Omega\ddot{\Omega}}{\dot{\Omega}^2} = 2 - \frac{P\ddot{P}}{\dot{P}^2}, \tag{D.4}$$

even though the measured braking indices are mostly lager than -3.

Bibliography

AGIS 2010, http://www.agis-observatory.org/

Abdo, A. A., et al. 2007, ApJl, 664, L91

Abdo, A. A., et al. 2010a, ApJs, 188, 405

Abdo, A. A., et al. 2010b, ApJ, 714, 927

Abdo, A. A., et al. 2009, arXiv:0910.1608

Abe, K., Abe, K., Adachi, I., et al. 2001, Physical Review Letters, 87, 101801

Acero, F., et al. 2010, A&A, 516, A62

Adachi, Y., 2005, Master thesis, Tokyo university

Aharonian, F., et al. 2002, AAP, 393, L37

Aharonian, F., & Bogovaloc, S. V., 2003, New Astronomy, 8, 85

Aharonian, F., et al. 2004, ApJ, 614, 897

Aharonian, F., et al. 2005a, AAP, 435, L17

Aharonian, F., et al. 2005b, Science, 307, 1938

Aharonian, F., et al. 2005c, A&A, 437, L7

Aharonian, F., et al. 2005d, AAP, 431, 197

Aharonian, F., et al. 2005e, AAP, 442, 1

Aharonian, F., et al. 2006a, ApJ, 636, 777

Aharonian, F., et al. 2006b, AAP, 448, L43

Aharonian, F., et al. 2006c, A&A, 449, 223

Aharonian, F., et al. 2006d, A&A, 460, 365

Aharonian, F., et al. 2007, AAP, 467, 1075

Aharonian, F., et al. 2008, AAP, 477, 353

Aharonian, F., et al. 2009, ApJ, 692, 1500

Albert, J., et al. 2006, Science, 312, 1771

ATNF Pulsar Catalogue, http://www.atnf.csiro.au/research/pulsar/psrcat/

Atoyan, A. M., & Aharonian, F. A. 1999, MNRAS, 302, 253

Backer, D. D. & Hellings, R. W. 1986, ARA& A, 24, 537

Bednarek, W. 2007, MNRAS, 382, 367

Bell, A. R., 1978, MNRAS, 182, 147

Bertsch, D. L., et al. 1992, NAT, 357, 306

Blandford, R. D., Ostriker, J. P., 1978, ApJ, 221, L29

Bock, D. C.-J., Large, M. I., & Sadler, E. M. 1999, AJ, 117, 1578

Bucciantini, N., Arons, J., & Amato, E. 2010, MNRAS, 1423

Casares. J., Ribo, M., Ribas, I., et al. 2005, MNRAS, 364, 899

Castor, J. I., David, C., & Klein, R. I. 1975, ApJ, 195, 157

Chatterjee, S., et al. 2005, ApJl, 630, L61

Coppi, P. S., & Aharonian, F. A. 1997, ApJL, 487, L9

CTA 2010, http://www.cta-observatory.org/

Dame, T. M., Hartmann, D., and Thaddeus, P., 2001, ApJ, 547, 792

Davis, J. & Cotton, E. 1957, *Jornal of Soloar Energy Sci. and Eng.*

Dickey, J. M., & Lockman, F. J. 1990, ARA&A, 28, 215

Dodson, R., Legge, D., Reynolds, J. E., & McCulloch, P. M. 2003, ApJ, 596, 1137

de Jager, O. C., et al. 2009, arXiv:0906.2644

Ellison, D. C., Baring, M. G., & Jones, F. C., 1995, ApJ, 453, 873

Enomoto, R., et al. 2002a, Nature, 416, 823

Enomoto, R., et al. 2002b, Astroparticle Physics, 16, 235

Enomoto, R., et al. 2006a, ApJ, 638, 397

Enomoto, R., et al. 2006b, ApJ, 652, 1268

Enomoto, R., et al. 2009, ApJ, 703, 1725

Fahlman, G. G., & Gregory, P. C. 1981, Nature, 293, 202

Fazio, G. G. et al. 2004, ApJs, 154, 10

Fermi, E., 1949, Phys.Rev., 75, 1169

Fisher, R. A. 1936, Annals of Eugenics, 7, 179

Fujita, Y., Hayashida, K., Takahashi, H., & Takahara, F. 2009, PASJ, 61, 1229

Funk, S., et al. 2007, ApJ, 662, 517 2007

Gaensler, B. M., Brazier, K. T. S., Manchester, R. N., Johnston, S., & Green, A. J. 1999, MNRAS, 305, 724

Gaensler, B. M., Arons, J., Kaspi, V. M., Pivovaroff, M. J., Kawai, N., & Tamura, K. 2002, ApJ, 569, 878

Gaisser,t.k., et al., Cambridge University Press, (1990)

Garcia-Munoz, M., et al., 1997, ApJ, 217, 859

Hara, S., 1999, Master thesis, Tokyo Institute of Technology

Hewish, A., Bell, S. J., Pilkington, J. D., Scott, P. F., and Collins, R. A. 1968, Nature, 217, pp.709

Higashi, Y., et al. 2008, ApJ, 683, 957

Hillas, A. M. 1985, Proc. 19th ICRC (La Jolla), 3, 445

Hinton, J. 2007, Proc. 30th ICRC, 1335

Hinton, J. A., & Aharonian, F. A. 2007, ApJ, 657, 302

Hofmann, W., Jung, I., Konopelko, A., Krawczynski, H., Lampeitl, H., and Phuhlhofer, G., 1999, Atropart Phys, 12, 135

Jelly, J. V. 1958, Cherenkov, radiation and its application, Pergamon Press

Kabuki, S., et al. 2003, Nucl. Inst. Meth., A500, 318

Kabuki, S. 2004, Ph.D. thesis (Tokyo U)

Kabuki, S., et al. 2007, ApJ, 668, 968

Katagiri, H., et al. 2005, ApJ, 619, L163

Kawachi, A., et al. 2001, Astropart. Phys., 14, 261

Kelner, S. R., & Aharonian, F. A. 2008, PRD, 78, 034013

Kiuchi, R., 2004, Master thesis, Tokyo university

Klepac, E. G., Ptuskin, V. S., & Zirakashvili, V. N., 2000, Atroparticle Physics, 13, 161

Kobayashi, C., Umeda, H., Nomoto, K., Tominaga, N., & Ohkubo, T. 2006, ApJ, 653, 1145

Kubo, H., et al. 2001, Proc. 27th ICRC (Hamburg), 2900

Kubo, H., et al. 2003, Proc. 28th ICRC (Tsukuba), 2863

Kuiper, L., Hermsen, W., den Hartog, P. R., and Collmar, W. 2006, ApJ, 645, 556

Lande, J., Ackermann, M., Allafort, A., et al. 2012, ApJ, 756, 5

Landi, R., et al. 2006, ApJ, 651, 190

Landi, R., et al. 2007, ATel, 1047

Lewis, D. A. 1990, *Exp. Astron.*, 1, 213

Li, T. P., & Ma, Y. Q., 1983, ApJ, 272, 317

Livingstone, M. A., Kaspi, V. M., Gotthelf, E. V., & Kuiper, L. 2006, ApJ, 647, 1286

ongair, M. S., 1992, High energy astrophysics, Second edition, Cambridge university press, Volume 1

Malkov, M. A., Diamond, P. H., & Sagdeev, R. Z. 2005, ApJl, 624, L37

Manchester, R. N., Hobbs, G. B., Teoh, A., & Hobbs, M. 2005, AJ, 129, 1993

Manzali, A., De Luca, A., & Caraveo, P. A. 2007, ApJ, 669, 570

Markwardt, C. B., & Ogelman, H. 1995, NAT, 375, 40

Matsumoto, H., et al. 2008, PASJ, 60, 123

Matsunaga, K., Mizuno, N., Moriguchi, Y., Onishi, T., Mizuno, A., & Fukui, Y. 2001, PASJ, 53, 1003

Mattana, F., et al. 2009, ApJ, 694, 12

Mizukami, T., 2007, Master thesis, the University of Kyoto

Montmerle, T. 1979, ApJ, 231, 95

Muno, M. P., Law, C., Clark, J. S., Dougherty, S. M., de Grijs, R., Portegies Zwart, S., & Yusef-Zadeh, F. 2006, ApJ, 650, 203

Muraishi, H., et al. 2000, AAP, 354, L57

Murphy, T., Mauch, T., Green, A., Hunstead, R. W., Piestrzynska, B., Kels, A. P., & Sztajer, P. 2007, VizieR Online Data Catalog, 8082, 0

Naito, T., & Takahara, F., 1994, J.Phys. G, 20, 477

Nakamori, T., 2008, Ph.D. thesis, University of Kyoto

Nakamori, T., et al. 2008, ApJ, 677, 297

Ohishi, M.(2002), Master thesis(Tokyo U)

Ohishi, M.(2005), Doctor thesis(Tokyo U)

Ohm, S., et al. 2009, arXiv:0906.2637

Ohm, S., et al. 2010, Astronomical Society of the Pacific Conference Series, 422, 265

Piatti, A. E., Claria, J. J., and Bica, E. 2000, A&A, 360, 529

Porter, T. A., & Strong, A. W. 2005, Proc. 29th ICRC (Pune), 4, 77

Rowell, G., Horns, D., Fukui, Y., & Moriguchi, Y. 2008, AIP Conf. Series, 1085, 241

Rybicki, G. B., Lightman, A. P., 1979, Radiative processes in astrophysics, A Wiley Interscience publication

Seo, E. S., & Ptuskin, V. S., 1994, ApJ, 431, 703

Slane, P., Castro, D., Funk, S., Uchiyama, Y., Lemiere, A., Gelfand, J. D., & Lemoine-Goumard, M. 2010, ApJ, 720, 266

Strong, W.S., & Moskalenko, I.V., 2006, GALPROP project, http://galprop.stanford.edu/web_galprop/galprop_home.html

Sturner, S. J., Skibo, J. G., Dermer, C. D., & Mattox, J. R. 1997, ApJ, 490, 619

Swordy, A., 2001, Space Sci. Rev., 99, 85

Tanaka, T., et al. 2008, ApJ, 685, 988

Tanaka, S. J., & Takahara, F. 2010, ApJ, 715, 1248

TeVCAT, http://tevcat.uchicago.edu/

Uchiyama, Y., Takahashi, T., Aharonian, F. A., & Mattox, J. R. 2002, ApJ, 571, 866

Uchiyama, H., Matsumoto, H., Tsuru, T. G., Koyama, K., & Bamba, A. 2009, PASJ, 61, 189

Uchiyama, Y., Aharonian, F. A., Tanaka, T., Takahashi, T., & Maeda, Y. 2007, NAT, 449, 576

Vasisht G. & Gotthelf E.V. 1997, ApJ, 486, L129

Voelk, H. J., & Forman, M. 1982, ApJ, 253, 188

Yamazaki, R., et al. 2006, MNRAS, 371, 1975

Yamazaki, R., Kohri, K., & Katagiri, H. 2009, A&A, 495, 9

Yuasa, M. 2006, Master thesis(Tokyo U)

Watanabe, S., et al. 2003, Proc. 28th ICRC (Tsukuba), 4, 2397

Weekes, T. C., et al. 1989, ApJ, 342, 379

Willingale, R., Aschenbach, B., Griffiths, R. G., Sembay, S., Warwick, R. S., Becker, W., Abbey, A. F., & Bonnet-Bidaud, J.-M. 2001, AAP, 365, L212

Acknowledgement / 謝辞

京都大学宇宙線研究室の谷森達氏には本論文の作成を始めとして、大学院での研究を一貫してご指導いただき大変感謝しています。また同研究室の窪秀利氏には研究の具体的な進め方、論文の執筆まで詳細にご指導いただきました。有難うございました。茨城大学の吉田龍生氏には放射機構モデルについてご指導いただきました。大変感謝しています。全ての CANGAROO メンバーに観測・解析・論文の作成にあたり、多くのご指導・ご助言をいただきました。大変感謝しております。

京大宇宙線研究室の CAGAROO メンバーの西田大輔氏、身内至緒氏、中森健之氏、東悠介氏、中野晋太郎氏には、DAQ・解析ソフトを協力して構築・メンテナンスできたことを大変感謝しております。宇宙線研究室の X 線・ガンマ線メンバーの皆様には研究を進める上で大変刺激を与えていただきました。特に上野一樹氏、内山秀樹氏、小澤碧氏には研究を進めるうえでいろいろなことを共有でき、楽しく研究を進めることができました。ありがとうございます。

ルネサスエレクトロニクスの石坂勝男氏には博士論文執筆について理解いただき大変感謝しております。また新井大輔氏には論文執筆を進めるように常に励ましていただきました。ありがとうございました。

最後に大学院博士課程まで進むことに理解を示しサポートしていただいた両親と、社会人になってからの論文の執筆という私のわがままに協力してくれた妻と娘に感謝します。